Quantitative Phase Imaging of Biological Samples using Optical Coherence Tomography

A Thesis Submitted in Fulfillment of the Requirement for the Award of the Degree of

DOCTOR OF PHILOSOPHY

in Engineering

Submitted By

NEERU SINGLA

(Reg. No. 901504006)

Under Supervision of

Dr. Vishal Srivastava
Associate Professor,
Department of Electrical & Instrumentation Engineering,

Department of Electrical and Instrumentation Engineering

THAPAR INSTITUTE OF ENGINEERING &
TECHNOLOGY PATIALA, PUNJAB

August, 2019

Dedicated

To

My Parents

Shri Taraki Lal & Smt. Kamlesh Rani

CERTIFICATE

This is to certify that the thesis entitled **"Quantitative Phase Imaging of Biological Samples using Optical Coherence Tomography"** being submitted by **Neeru Singla** to the Department of Electrical & Instrumentation Engineering, Thapar Institute of Engineering & Technology (Deemed to be University), Patiala for the award of the degree of **Doctor of Philosophy**, is a record of bonafide research work carried out by her under my guidance and supervision and has fulfilled the requirements for the submission of this thesis, which to my knowledge has reached the requisite standard.

The results embodied in the thesis have not been submitted in part or full to any other University or Institute for the award of any degree or diploma.

Srivastava

Dr. Vishal Srivastava

Associate Professor,

Department of Electrical & Instrumentation
Engineering,

Thapar Institute of Engineering &
Technology (Deemed to be University),
Patiala

ACKNOWLEDGEMENTS

This study was a challenging one and it would have been unachievable without the help and encouragement of many people. I honestly feel short of words for acknowledging the people who helped me directly and indirectly to complete this whole journey.

With due regards and great delight, I convey my heartful gratitude and indebtedness to my supervisor **Dr. Vishal Srivastava**, Associate Professor, Department of Electrical & Instrumentation Engineering, Thapar Institute of Engineering & Technology, Patiala for his skilful guidance, proficient evaluation, persistent encouragement, and conscientious supervision throughout this academic endeavour. His hard-working nature and methodical suggestions were a constant source of encouragement to me. It is owing to their able guidance, expertise, inquisitive attitude, and tireless efforts that I find my vision even more broadened. I earnestly thank him from the core of my heart for being a consistent source of inspiration right through the beginning till the end.

I am very thankful to **Dr. Soumendu Jana**, Associate Professor, School of Physics & Material Science, **Dr. Deepti Mittal**, Associate Professor, Department of Electrical & Instrumentation Engineering and **Dr. Saurabh Bhardwaj**, Associate Professor, Department of Electrical & Instrumentation Engineering, for being the members of Doctoral Committee and spending their valuable time in reviewing and critically examining the work.

I am also thankful to present Chairman of the Doctoral Committee **Dr. R.S. Kaler**, Senior Professor & Head, Department of Electrical and Instrumentation Engineering for the much-needed support throughout the work.

My heartfelt gratitude is due to **Dr. Rafat Siddique**, Senior Professor & Dean, Research and Sponsored Projects and Honourable Director **Dr. Prakash Gopalan** for the encouragement, support and providing the necessary facilities to carry out and complete this work on steady course.

I also wish to express my deep sense of gratitude to **Prof. Dalip Singh Mehta**, Department of Physics, IIT Delhi for providing me facility to do experimental work in his lab and all the persons of the lab for helping me in the experiments.

I would also thankful to **Dr. Prashant Singh Rana**, Assistant Professor, Department of Computer Engineering to guide me in machine learning concepts.

I would like to thank **Kriti, Gurleen, Arunpreet, Arshdeep, Parveen** and **Manjit**. I am very fortunate to have wonderful and caring friends to support me.

I would like to express my loving gratitude for my family, who are the most precious people in my life and without whose efforts I would have not achieved this whole journey.

Last but not least, I bow in reverence to **ALMIGHTY GOD** who has always showered blessings on me at each and every step to complete this thesis.

Neeru Singla

Neeru Singla

ABSTRACT

Advancement in the diagnostic techniques is required for early detection of the disease which will avoid the many risks to patients. This thesis research work describes a novel imaging technique for quantitative phase imaging of the biological samples. We developed a full-field optical spatial coherence microscopy (FF-OSCM) system based on monochromatic laser. The system is characterized in terms of axial resolution, lateral resolution, phase sensitivity and phase stability. The developed system exploits the property of spatial coherence and its performance is comparable to the conventional optical coherence microscopy based on temporal coherence. The system is used for the quantification of different stages of malaria infected red blood cells (RBCs) through a fully-automated computer-aided system. The system further modified to study the different stages, especially early and late trophozoite of malaria with limited labelled data size using the customized convolutional neural networks (CNNs). The results were also compared with commonly known CNNs and shows that our automated system has a comparable performance with less computational time.

We also develop an automated algorithms for the classifications of the human burnt skin injuries *in vivo*, and margin assessment of the breast cancer tissues using optical coherence tomography (OCT) images. Our proposed automated procedure entails building a machine learning based classifier by extracting quantitative features of normal and burn tissue images recorded by OCT and obtained good sensitivity and specificity. Our results show the capability of a computer-aided technique for accurately and automatically identifying burn tissue resection margins during surgical treatment. Furthermore, the study was performed in the classification of the human breast cancer tissues using OCT images. We developed an automated algorithm based on a pretrained CNN (Inception-v3) architects with reverse active learning for the classification of healthy and malignancy breast tissue. The network output is also correlated with the corresponding histology image. Our results lay the foundation for the future that the proposed method can be used to perform automatic intraoperative identification of breast cancer margins in real-time and to guide core needle biopsies.

In the last part of this thesis, phase shifting interferometry (PSI) based FF-OCT system was employed *exvivo* for the study of breast cancer tissue and stored RBCs. The

experimental system is based on Mirau interferometer illuminated by tungsten halogen lamp. It produces high resolution *enface* images, therefore it doesn’t need a point-by-point scanning as in the case of conventional OCT system. Textural features were extracted from the phase images for the quantification of breast cancer tissue and stored RBCs.

TABLE OF CONTENTS

LIST OF FIGURES

LIST OF TABLES

LIST OF ACRONYMS

ATP	Adenosine triphosphate
ACT	Auto-Correlation term
AUC	Area Under the curve
ANN	Artificial Neural Networks
AdaGrad	Adaptive Gradient Algorithm
AvNNet	Average Neural Network
BD	Balanced Detector
BS	Beam Splitter
BN	Batch Normalization
CAD	Computer Aided Diagnosis
CCT	Cross-Correlation Term
CNN	Convolutional Neural Networks
CCD	Charge Coupled Device
Coll	Collimator
Cir	Circulator
DIC	Differential Interference Contrast
DHM	Digital Holographic Microscopy
DPM	Differential Phase Microscopy
DL	Deep Learning
DBN	Deep belief networks
DNN	Deep Neural Networks
EDTA	Ethylene diamine tetra-acetic acid
ELM	Extreme Learning Machine
FoV	Field of View
FP	False Positive
FN	False Negative
FC	Fiber Coupler
FF-OSCM	Full Field- Optical Spatial Coherence Microscopy
FPM	Fourier Phase Microscopy
FD-OCT	Fourier Domain Optical Coherence Tomography
GLCM	Gray-Level Co-Occurrence Matrix
GPU	Graphical Processing Unit
HMC	Hoffmann modulation contrast
HPM	Hilbert Phase Microscopy
LED	Light Emitting Diode
LSC	Longitudinal Spatial Coherence
MEMS	Micro Electro Mechanical System
MMFB	Multi-Mode Fiber Bundle
MO	Microscopic Objective
MCC	Mathew Correlation Coefficient
NA	Numerical Aperture
NDF	Neutral Density Filter
OAI	Off-Axis Interferometry
OCM	Optical Coherence Microscopy
OCT	Optical Coherence Tomography
PC	Phase Contrast

PSI	Phase Shifting Interferometry
PZT	Piezoelectric Transducer
PCA	Principle Component Analysis
QPI	Quantitative Phase Imaging
RBC	Red Blood Cell
RM	Reference Mirror
RI	Refractive Index
ROI	Region of Interest
RF	Random Forest
ReLu	Rectified Linear Unit
ROC	Receiver Operating Characteristics
RRF	Randomized Random Forest
SD	Standard Deviation
SLD	Super Luminescent Diode
SF	Spatial Filter
SNR	Signal to Noise Ratio
SLIM	Spatial Light Interference Microscopy
SCM	Spatial Coherence Microscope
SVM	Support Vector Machine
SS-OCT	Swept Source OCT
SD-OCT	Spectral Domain OCT
SGD	Stochastic Gradient Descent
TP	True Positive
TN	True Negative
TL	Transfer Learning
TD-OCT	Time-Domain OCT
TPM	Tomographic Phase Microscopy
USAF	United States Air Force
VCSEL	Vertical Cavity Surface Emitting Laser
WHO	World Health Organization
WL-DHM	White light diffraction phase microscopy
2-D	Two Dimensional
3-D	Three Dimensional

CHAPTER 1

INTRODUCTION

1.1 BACKGROUND

Optical microscopy is one of the standard tool for non-destructive testing of biological and industrial objects [1]. For the visualization of internal microstructure mainly in biomedical applications a high spatial resolution optical microscope with contrast agent is required [2]–[4]. In optical microscopy, contrast may be either exogenous (extrinsic) or endogenous (intrinsic). The well-known modality utilizing exogenous contrast to provide targeted morphological information is fluorescence microscopy, in which a specimen is labelled with a fluorescent molecule [5], [6]. Although, fluorescence microscopy is continuously applied across a broad range of studies, as there are number of applications in biology for which methods employing endogenous contrast are required. This is because label-free methods are not subject to photo-bleaching or photo-toxicity and therefore permit the observation of living cells in their natural environment over indefinite time periods with nearly or no sample preparation is required [7]. The main challenge associated with endogenous contrast is that cells should be transparent phase objects and produce very little contrast under normal illumination conditions. This problem has been solved optically using methods such as phase contrast (PC) [8], differential interference contrast (DIC) [9], confocal microscopic imaging, digital holographic microscopic imaging and Hoffmann modulation contrast (HMC) microscopy [10]. But all above mentioned techniques suffers some limitations either depth of penetration or with poor spatial and axial resolution. Abbe gave an idea for the phase imaging, produced by interference pattern between the scattered and the unscattered light beams, used in the above methods [8]. This information acknowledged by Zernike to develop phase contrast microscopy [11]. Phase contrast microscopy has a potential to improve the contrast of an image by putting a quarter-wavelength delay between the reference beam and the sample beam. Phase contrast has encouraged many biological imaging studies and received Zernike in 1953 Nobel Prize in Physics [8]. While widely adopted by microscopists world-wide for label-free imaging, phase contrast images can only provide qualitative information. Nowadays, it has become clear that the quantitatively measuring the properties of cellular activities with high resolution, in three dimensions, across a wide range of spatial and temporal scales, and in a minimally invasive manner are required [12]–[14]. Multi-scale facilities are important, since the developing cellular behaviour is the outcome of taking whole information from inter-cellular interactions, intra-cellular molecular reactions and myriad environmental stimuli. The output response to these factors also has different implications at a wide range of scales. The observations of the changes at the cellular level in the growth rate, morphology, in the cell cycle, or motility or in various inter-cellular processes. Further, changes may be taken at the level of the cellular culture or population in the overall proliferation rate, spatial architecture, etc. However, to understand the behaviour of the cellular studies, there is a requirement of those measuring techniques which can enumerate all the parameters simultaneously, across the relevant spatial and temporal scales. All the above-mentioned methods are very useful but all suffers from one important drawback, that measured intensity has nonlinear, and thus non-invertible, relationship with the phase of the specimen. The field of quantitative phase imaging (QPI) was born out of attempts to quantitate the contrast generating mechanism in phase contrast microscopy. Without this information, extracting morphologically relevant parameters like size, refractive index (RI) and dry mass density, etc. are not much effective. With the help of QPI, we can extract the phase variations and RI of the specimen. Figure 1.1 illustrates the information which is typically available from QPI experiments [15].

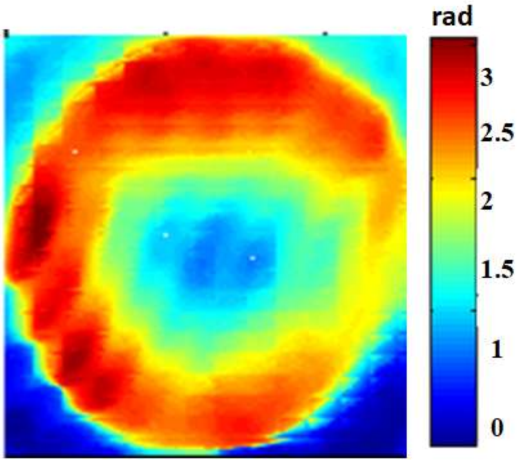

Figure 1.1 Representation of QPI data

1.2 QUANTITATIVE PHASE IMAGING

QPI provides much more rigorous analysis of the image as compare to the intensity image obtained by conventional microscopic technique. The phase map contains various information, such as cell thickness and RI which allow quantization of cellular morphology under experimental conditions [16], [17]. Nowadays, QPI play an important role in the biological studies [18], [19]. For example, QPI has recently measured cell cycle-dependent growth patterns by exploiting the fact that phase images are proportional to morphological changes like dry mass density, RI etc. [20] and brought insight to the age-old question of how single cells regulate their growth. QPI has also enabled the monitoring of cytoskeletal/organelle interactions on short time-scales due to its ability to image cytoskeletal structures in parallel [21], whereas, fluorescence microscopy requires multiple fluorescent labels to get the same image information. Likely, QPI has been used to quantify intracellular mass transport [22], monitor the effects of Adenosine triphosphate (ATP) on red blood cell (RBC) and membrane dynamics [23]. In addition to biology, QPI is making waves in the realm of clinical diagnostics [12], [24], [25], where it has recently manifested itself as a powerful tool for low-cost, high throughput, and high-sensitivity RBC screening [26]. Another developing area for QPI is cancer diagnosis, where it has been used to differentiate cancerous cells in isolation [27], identify tissue self-affinity as a potential biomarker for precancer [28], detect calcium oxalate as a breast cancer screening tool, and correlate cancerous regions in prostate biopsies with high variance in the phase image [29].

Recently, various QPI methods have been developed to obtain the quantitative images of different biological objects such as optical coherence microscopy (OCM) [3], [30], [31], tomographic phase microscopy (TPM) [32], phase-shifting interferometry (PSI) [33], Fourier phase microscopy (FPM) [18], digital holographic microscopy (DHM) [16], diffraction phase microscopy (DPM) [34], spectroscopic diffraction phase microscopy [35] and Hilbert phase microscopy (HPM) [36]. All these methods are very much successful and each technique has its own advantages and disadvantages. QPI interferometry technique is the high-resolution quick imaging and simultaneous production of interference between the sample and reference objects.

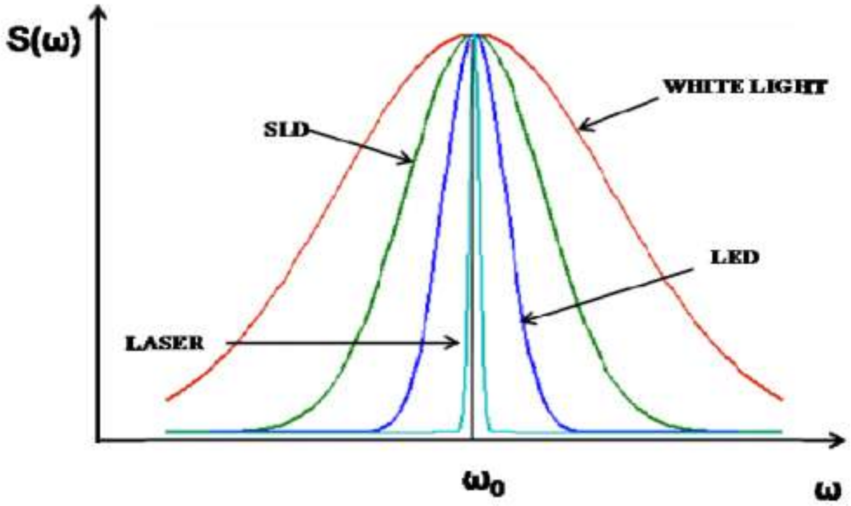

Figure 1.2 Optical spectrum profiles of various light sources vary with the bandwidth variation.

To optimize the image quality, the choice of light source is very critical. It is desirable to use broad band light source whose coherence length is very small to achieve better axial resolution [37]. Therefore, the unwanted fringes due to multiple reflections from the different surfaces can be avoided and accurate slice selection in the sample is possible. A qualitative comparison between the optical spectrum of a broadband source and that of a laser is shown in figure 1.2 [38]. The spectrum of super luminescent diode (SLD) is not always broader than light emitting diodes (LED), such as in the case of white LED. But as compare to single color LED the SLD spectrum is relatively broader bandwidth.

1.3 QUANTITATIVE PHASE IMAGING METHODS

QPI methods image the optical path length of a phase object integrated along the optical or z-axis. In the literature, there are numerous ways to do this [9]. QPI can be broadly classified into two categories: PSI and slightly off-axis interferometry (OAI). To understand the comparison between the QPI methods, we theoretically explain the spatial frequency domains of the methods in figure 1.3, slightly off-axis and PSI interferometry [39], [40].

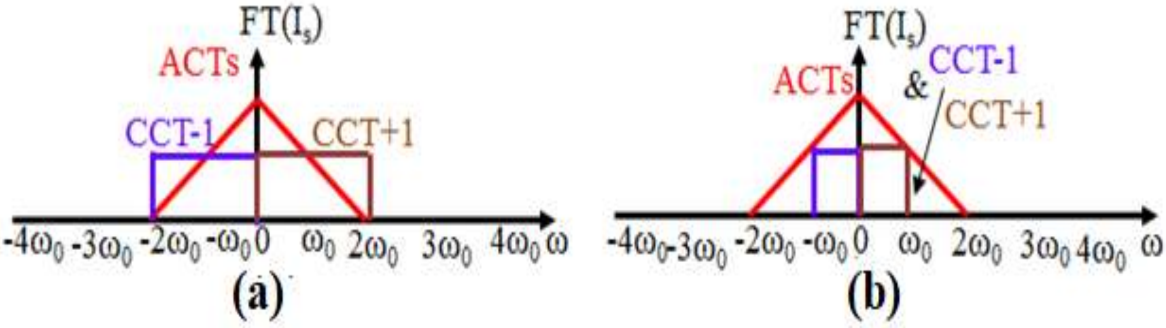

Figure 1.3 Graphically differentiate the spatial frequency spectrum of (a) Slightly OAI, and (b) PSI; CCT (Cross Correlation Term), ACT (Auto Correlation Term).

In both cases the two auto-correlation terms (ACTs), situated around the origin of the spatial spectrum, this consists of the reference arm and sample arm. Since the reference arm is taken to be a constant axis over the camera illumination area, the total width of the ACTs for an interferometric image is only determined by the width of the sample arm ACT given by four times the highest spatial frequency ω_0 of the object recorded by the camera. In comparison, the width of each cross-correlation term (CCT) is only $2\omega_0$.

In slightly-OAI as seen in figure 1.3(a), the CCTs should not be overlapped, but the overlapping of the ACTs with each CCT's is acceptable. Therefore, the highest spatial frequency needed per exposure is only $2\omega_0$. However, in the case of phase shifting interferometry as shown in figure 1.3(b), all ACTs and CCTs are centered at the origin. Therefore, the required highest spatial frequency per exposure is only ω_0. So, therefore, in this case, four or five interferogram patterns (depending on the technique chosen) should be attained to completely remove the both ACTs and one of the CCTs.

1.3.1 Phase-Shifting Interferometry

In PSI, a coherent laser beam is incident on an imaging system/interferometer. The beam is split into sample and reference arms, which are then recombined collinearly at the image plane [41]. By modulating the phase of the reference arm, the resulting interferograms are also modulated where the bias of each pixel is determined by the phase of the sample. Conventionally, four interferograms are measured as the reference phase is modulated in equal increments around the unit circle such that the phase image is easily obtained using trigonometric relationships [14]. A block diagram representation is given in figure 1.4 which includes spatial filter (SF), beam splitter (BS), objective lens (OBJ) and CCD [42].

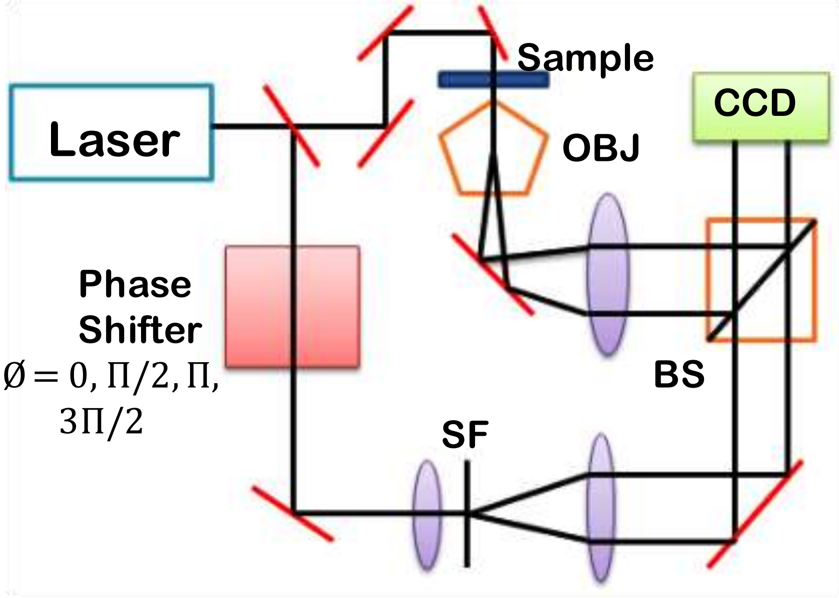

Figure 1.4 Schematic representation of PSI.

Because the interfering beams are collinear, PSI preserves the spatial resolution inherent in the sample arm's imaging optics, which may be diffraction-limited [9]. Phase sensitivity is determined by the Signal to Noise Ratio (SNR) which is easily maximized by controlling the relative powers of each beam. Furthermore, the method is computationally simple and requires no assumptions about the scattering properties of the sample. Disadvantages in PSI stem from the fact that multiple interferograms are required per phase image thereby limiting acquisition speed. Also, phase and speckle noise tend to reduce temporal and spatial phase stability in systems utilizing non-common-path geometries and monochromatic light. In the recent years, researchers have mitigated some of these issues by sacrificing alignment tolerance for speed [43] and adapting PSI to common-path geometries [44] and white light illumination [34].

1.3.2 Slightly Off-Axis Interferometry

To extract the phase information of the dynamic biological samples, since it requires only single interferogram slightly off-axis interferometry performs better as compared to PSI interferometry. Slightly-OAI is similar to PSI, except that spatial, rather than temporal, modulation is used in which the reference beam propagates at a known off-axis angle. The resulting interferograms are spatially modulated with a periodicity determined by this angle. The transmission function of the sample can be reconstructed in many ways; for example Fourier domain demodulation [4] or Hilbert transform methods [45] may be used. A block diagram representation is given in figure 1.5.

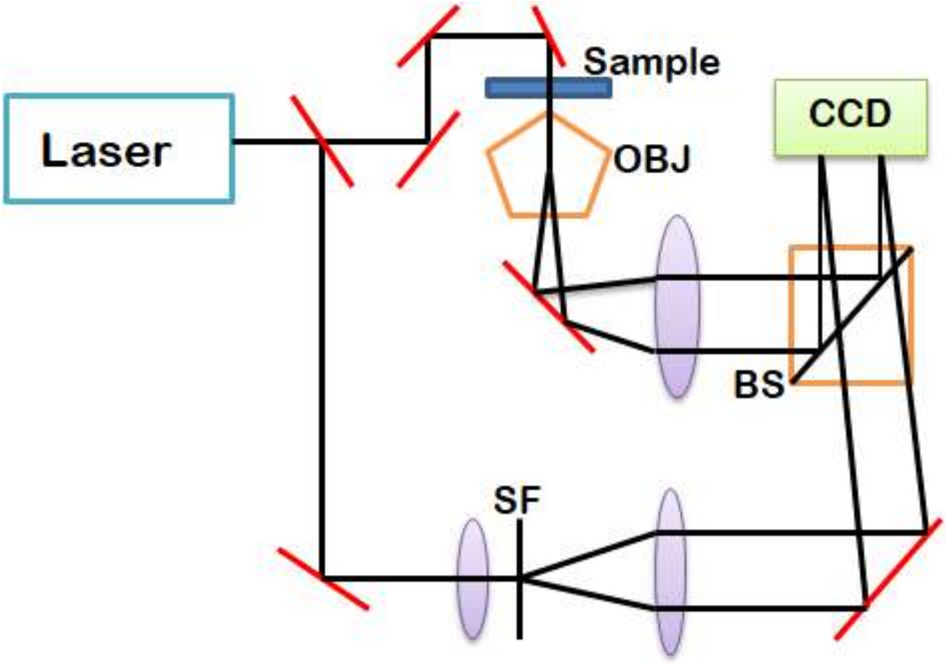

Figure 1.5 Schematic representation of slightly- OAI.

Because phase recovery is based on a single interferogram, temporal resolution is maximized and only limited by camera readout speed. Like PSI, slightly-OAI benefits from controllable fringe visibility and doesn’t require scattering assumptions. Unlike PSI, however, spatial resolution in slightly-OAI is often limited by the off-axis angle and not the imaging optics. Slightly-OAI also suffers from reduced sensitivity associated with phase and speckle noise and reconstruction methods are often complicated by the need to unravel a highly wrapped phase function in the presence of noise [46]. As with PSI, slightly-OAI researchers have increased phase stability by adopting common-path geometries [47] and using white light [34].

1.3.3 Quantitative Phase Imaging Method Comparison

The overall characteristics of selected QPI methods reported in the literature are summarized in Table 1.1. The configurations cited in Table 1.1 are not exhaustive and are meant to be representative of progress within each category.

Table 1.1 Characteristic summaries for representative QPI methods

QPI Method	**Published Configuration**	**Single-shot**	**High resolution**	**Sensitivity**	**Common Path**	**Broadband Light source**	**No object Scattering Assumptions**	**Computa -tionally simple**
PSI	PS-DHM [16]	✗	✓	✓	✗	✗	✓	✓
	FPM [18]	✗	✓	✓	✓	✗	✓	✓
	SLIM [48]	✗	✓	✓	✓	✓	✓	✓
Slightly OAI	Slightly-OA-DHM [47]	✓	✗	✓	✗	✗	✓	✗
	DPM [49]	✓	✗	✓	✓	✗	✓	✗
	wDPM [34]	✓	✗	✓	✓	✓	✓	✗

where, **✓’s** indicates presence of a desired attributes, **✗’s** indicates absence of a desired attributes.

The table compares QPI methods using the following metrics: single-shot (enables high acquisition speed), high spatial resolution, sensitive (high SNR), common-path (eliminates phase noise), broadband light source (reduces speckle noise), no object scattering assumptions (strongly scattering 2D phase objects with sharp edges can be imaged without artifacts), and computationally simple (enables real-time processing). From the above table it's sufficient to motivate the present research work that we have to develop a single-shot, high resolution, common-path broadband slightly off-axis quantitative phase microscope system to achieve higher stability and fast acquisition for biological applications.

1.4 OPTICAL COHERENCE TOMOGRAPHY

Optical coherence tomography (OCT) is a non-invasive medical imaging technique which is being reliable for high resolution (micrometer-scale) tomographic imaging of biological applications as well as it measures the amplitude of the backscattered light by the sample being imaged [50], [51]. OCT was initially given by Huang et.al [1] in time-domain mode of operation. The OCT can be envisioned as an optical analogy to ultrasound imaging where the technique visualizes echoes from discrepancies in a sample. In OCT, light is being used as a source for the detection of optical echoes rather than sound. OCT has many advantages like low temporal coherence property of light source for high sensitivity and high resolution optical sectioning [1], [52], [53]. Light reflected or backscattered from the object propagates with different delay times, from the different layers of the object [50]. By translating the reference mirror one can obtain a longitudinal profile of reflectivity versus depth. OCT measures the eco-time delay of back scattered or back reflected light from different layers of the object to determine the dimension of object. The key parameters in OCT systems are sensitivity, resolution and acquisition speed. Axial resolution depends upon bandwidth of the light source whereas lateral resolution depends upon the numerical aperture (NA) of the imaging optics [52].

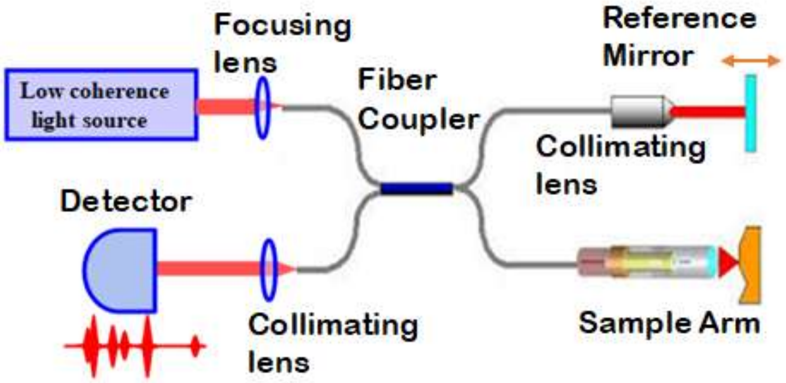

Figure 1.6 (a) Schematic diagram of optical coherence tomography.

The schematic diagram of a traditional OCT system is illustrated in the figure 1.6 (a). A fiber-coupler based Michelson interferometer is illuminated by a broad band or low coherence light source. Light is directed to 2 × 2 fiber coupler and it is supposed to be equal power is dispersed on both sample and reference arms, however, there are so many OCT systems which take the advantage of unbalance power splitting and have been described both experimentally and theoretically [54]. The output light at the reference fiber is incident on the reference mirror while the light at the output of the sample arm is incident onto the sample.

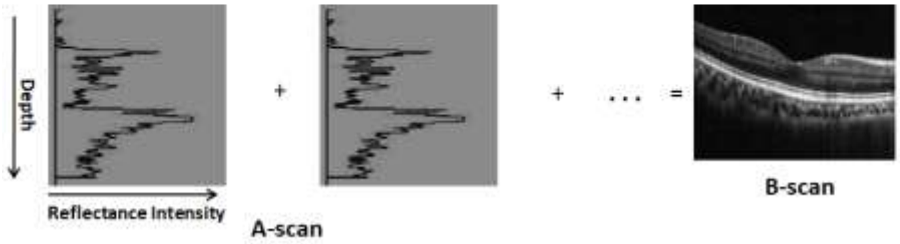

Figure 1.6 (b) A-scan and B-scan OCT images.

Light reflected or backscattered from the object propagates with different delay times, from the different layers of the object [19], [50] and the combined light is made to interfere on the surface of a photo-receiver or detector. By translating the reference mirror one can obtain a longitudinal profile of reflectivity versus depth, i.e. A-scan as shown in figure 1.6(b). On the basis of the point by point scanning mechanism the focused beam position into the sample, multiple A-scans are obtained and interfaced in the desktop into a 2D cross-sectional image of the sample in the region of the focal spot, defined as B-scan shown in figure 1.6(b) [1].

1.4.1 Theoretical Aspects of Extraction of Signal using OCT

From the figure 1.7, if a wavelength-independent bifurcation ratio for the beam splitter is taken, then the electric fields for low coherent light source reflected into sample and reference beams of the interferometer can be expressed as [38]:

$$E_S = E_R = b(k)e^{-j(\omega t - kz)} \tag{1.1}$$

where, E_R is the electric field at the reference beam,

E_S is the electric field at the sample beam,

$b(k)$ is the electric field amplitude spectrum,

k is the wave-number,

and z is the distance from the different layers of the sample.

Therefore, the attenuated electric field of the reference beam is as follows:

$$E_R = r_R b(k)e^{-j(\omega t - 2kz_R)} \tag{1.2}$$

where, r_R is the reference beam.

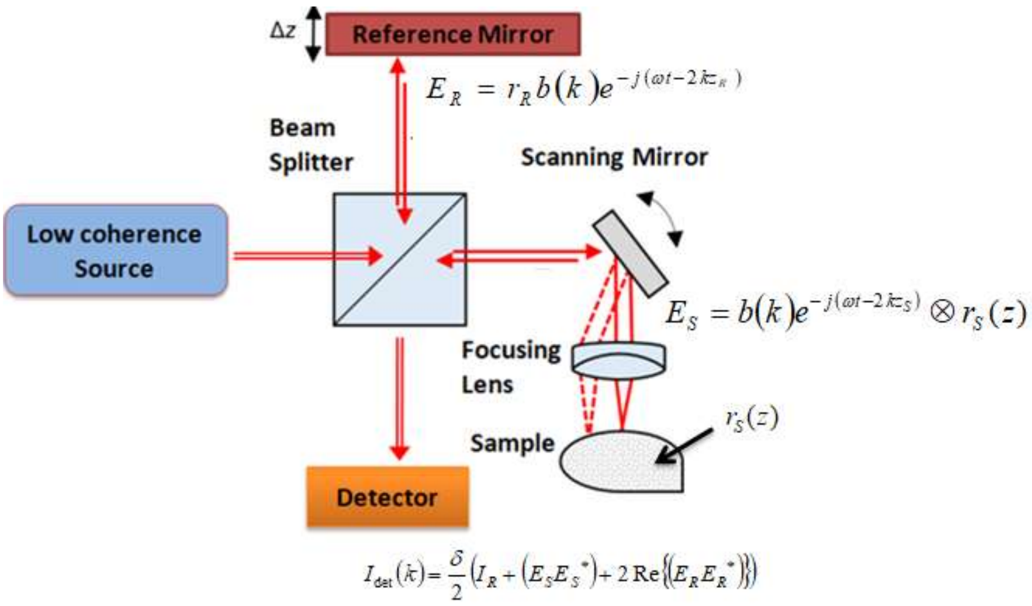

Figure 1.7 Schematic diagram of conventional OCT

The light incident on any given specimen will undergo back reflected from the multiple layers due to the presence of scattering particles and refractive index variations within the specimen. The back reflected photons reoccurring from the sample beam can be expressed by:

$$E_S = b(k) e^{-j(\omega t - 2kz_S)} \otimes r_S(z) \tag{1.3}$$

where, $r_S(z)$ is the depth-dependent amplitude reflectivity function of any given specimen.

Therefore, the sample and reference beams are recombined at the beam splitter and are given as,

$$E_{\det} = \frac{1}{\sqrt{2}}\left(E_S + E_R\right) \tag{1.4}$$

The incident light in terms of electric field is converted to photo current with the help of optical detectors, which are based on square law intensity detection devices. So, the originated photo current is directly related to the product of the average time of the incident electric field and its complex conjugate which is as follows:

$$I_{\det}(k) = \frac{\delta}{2}\left(E_S + E_R\right)\left(E_S^* + E_R^*\right) = \frac{\delta}{2}\left(I_R + \left(E_S E_S^*\right) + 2\,\mathrm{Re}\left\{\left(E_R E_R^*\right)\right\}\right) \tag{1.5}$$

where, δ is the detector responsivity in Ampere/Watt. The right-hand side of the first two term of the equation correspond to the DC component of the current and interference generated within the given specimen. The final term of the equation 1.5 represents the interference pattern generated between the reference and sample beams which further utilized to compute the structural information or axial depth profile in OCT. When the signal was simplified, the AC component of the photocurrent can be expressed as:

$$I_{ac}(k, \Delta z) = \delta B(k)\sqrt{R_R}R_S(\Delta z)\cos[2k\Delta z] \tag{1.6}$$

In order to obtain the axial structural profile information, the depth-dependent reflectivity function $R_S(\Delta z)$ of any desired specimen is extracted using various OCT signal processing techniques. In a point by point scanning system, the light propagates from the interferometer and is directly send to a detector is illustrate in figure 1.7. After taking the resampling and subtraction of the DC background, the axial depth profile of the structural information is produced by performing the inverse Fourier transform process. Different types of OCT are used to study the biological and industrial objects non-invasively [55]–[58].

1.4.2 Categories of Optical Coherence Tomography

OCT can be broadly divided into two main categories: time domain OCT (TD-OCT) and Fourier or frequency domain OCT (FD-OCT). In TD-OCT, the autocorrelation gives information about source spectral distribution. In contrast, in FD-OCT, the autocorrelation is calculated by the Fourier transform of the power spectral signal that is measured directly.

1.4.3 Time-Domain Optical Coherence Tomography (TD-OCT)

In time-domain OCT, the wavenumber - dependent photo detector current is recorded with the help of a single or multiple detectors where the reference beam is used to match the optical path length from the different depth reflections within the sample [52], [59]. To acquire the depth profile in TD-OCT reference mirror is moved in axial direction or in the direction of wave propagation to map out the sample reflectivity as a function of axial depth. Figure 1.8 shows the schematic diagram of TD-OCT system based on Michelson interferometer. The system uses a broad band light source. The light coming out from the source has been divided into two parts with the help of 2x2 fiber, one part is going towards the reference mirror and other part towards sample arm. The light reflected from the sample and the light reflected from the reference arm again recombines at fiber coupler. When the path difference between the reference arm and object arm is within the coherence length of light source interference occurs and recorded by the detector. Due to mechanical movement of the reference mirror to obtain the sample depth profile it gives rise to motion artifacts and limited repeatability [52].

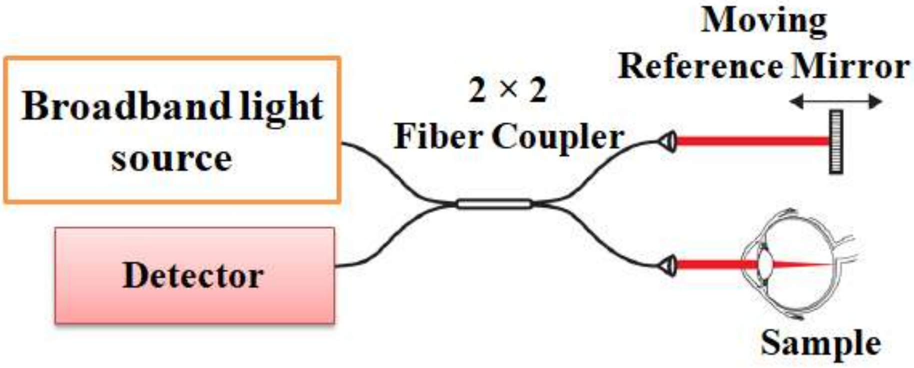

Figure 1.8 Schematic diagram of TD-OCT.

1.4.4 Fourier Domain Optical Coherence Tomography (FD-OCT)

In FD-OCT, signal detection relies on the transformation of the OCT time-varying signal along the optical axis, termed the A-scan, into the frequency domain. Thus FD-OCT has an advantage that full sample depth information can be extracted without scanning the reference mirror. FD-OCT was first introduced by A. F. Fercher, et al. in 1995 [60]. In 2003, R. Leitgeb et al. [61] and M. A. Choma et al. [53] showed that FD-OCT techniques provide sensitivities two to three orders of magnitude greater than TD-OCT. This sensitivity advantage would enable imaging hundreds of times faster than TD-OCT without sacrificing image quality. This dramatic improvement in imaging speeds in frequency domain detection made acquisition of 3D data sets feasible [61]. To analyze the spectrum of the interference signal in FD-OCT, in which the depth of the layer represents the frequency component and the reflectivity of that layer represents the amplitude [62]. Still, FD-OCT has also certain limitations. In FD-OCT, the optical frequency components yielded by the interferometer consists of two symmetrical components, they are complex conjugate to each other and called mirroring effect. The basic principle behind FD-OCT is Wolf's solution to the inverse scattering problem for determining the structure of weakly scattering objects. According to the Winner-Khintchine theorem, the spectral power amplitude of backreflected beam equals to the Fourier transform of the axial distribution of the object scattering potential [63].

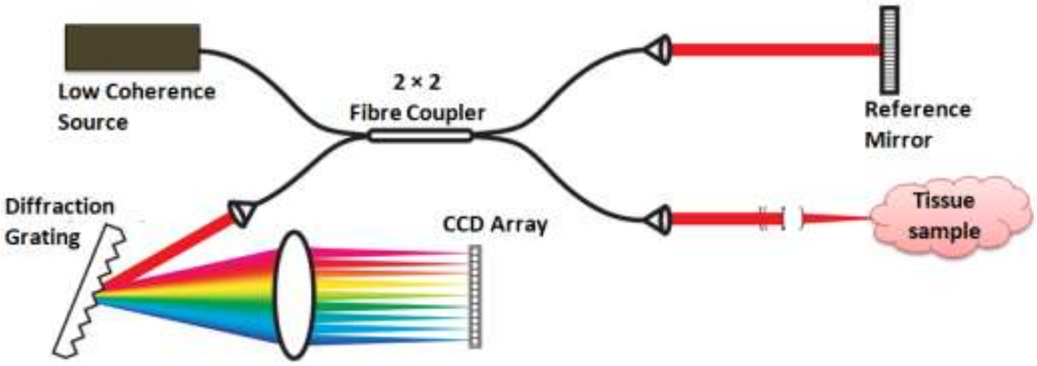

Figure 1.9 Schematic diagram of SD-OCT system [4].

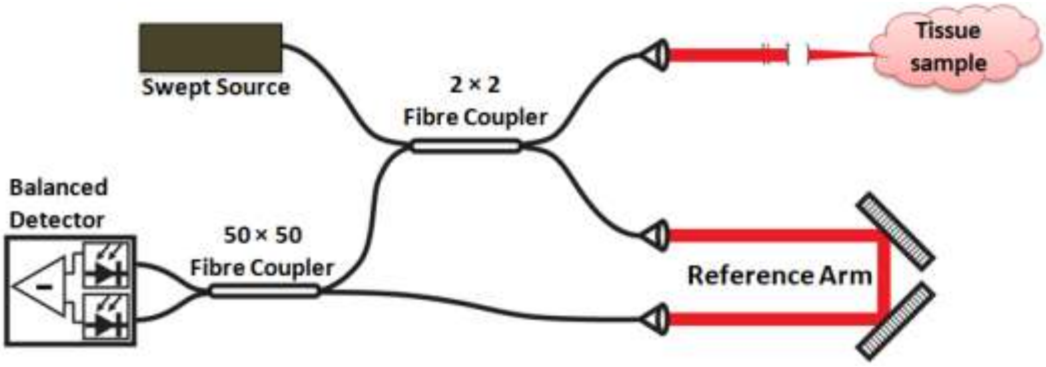

Figure 1.10 Schematic diagram of SS-OCT system [64].

Based on its implementation, the FD-OCT can be split into further two types: Spectral Domain OCT (SD-OCT) and Swept-Source OCT (SS-OCT). SD-OCT consists of a broadband light source and a spectrometer used in the detector arm to acquire the interference signal from the deep layers of the sample as seen in figure 1.9 [4]. The interference signal is dispersed by the diffraction grating and the corresponding to each individual wavelength components are detected by a CCD array. However, SS-OCT using a high speed tunable, narrow line width laser source and without dispersion components as seen in figure 1.10 [61]. In SS-OCT system, the given sample is probed with a narrow band instead of sampling the received spectrum over a finite wavelength. Some of my thesis chapter focus on discussion and utilization of SS-OCT systems.

1.4.5 Full-Field Optical Coherence Tomography (FF-OCT)

FF-OCT system is a technology extension of point-by-point scanning OCT system. In conventional OCT system we need three mechanical scan (one depth and two lateral scans) which will produce motion artifacts, non-repeatability and time-consuming [52]. FF-OCT system draws a lot of attention since it produces *enface* images and potentially faster operations. The basic principle behind the FF-OCT is low coherence interferometry. It uses low temporal and spatial coherence light source. In FF-OCT system a point detector is replaced by a 2D array of detector. The major parameters to perform full field OCT (FF-OCT) is the detector array used to detect the interference fringe pattern which classifying the OCT signal. In FF-OCT, the process of coherence detection is carried out in parallel at all the pixels. The transverse resolution of FF-OCT is similar to conventional microscopy whereas the axial resolution is determined by the spectral properties of the illumination source. Thus FF-OCT is an alternative approach to increase the imaging speed and acquire the larger area or full-field by an array of detector, such as, charged couple device (CCD) or complementary metal oxide semiconductor (CMOS) camera [31], [65]. Recently, the use of FF-OCT has been increased as a non-scanning, high resolution en-face imaging methods in several biological applications [66]–[69]. A schematic diagram of the FF-OCT based on Linnik interference microscope configuration which consists of beam splitter (BS), microscope objective (MO), neutral density filter (NDF), window glass (WG), angled mirror (AM), piezo-electric transducer (PZT), reference mirror (RM), collimating lens (coll lens) and 2D-CCD are shown in figure 1.11. Parallel acquisition allows simplification of the framework just as a higher acquisition speed as compare to point by point scanning OCT [39], [70].

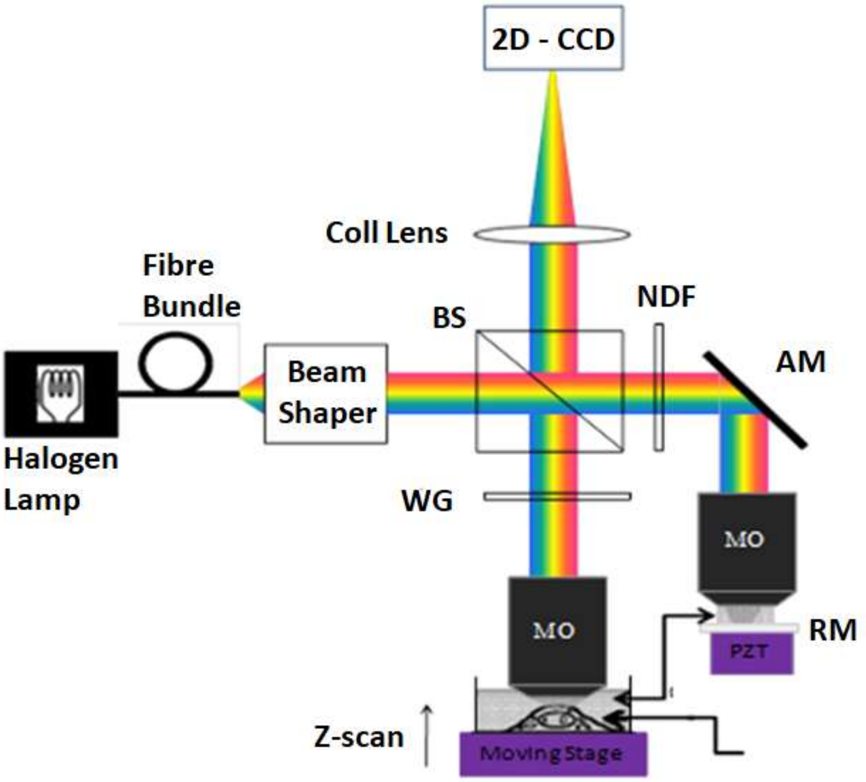

Figure 1.11 Schematic diagram of the FF-OCT system [71].

Moreover, FF-OCT offers the likelihood to utilize thermal light sources regardless of their low brightness by exploiting the much slower axial scan than in point scanning OCT [3], [72]. However, the brightness of thermal light sources remains insufficient requiring a trade-off between sensitivity and acquisition speed [73]. In FF-OCT, owing to a natural broad spectrum, a thermal light source offers a micrometer resolution along with the more benefits of low cost and simplicity. OCT, image acquisition depends on a detector array. In parallel TD-OCT techniques, the transverse en-face images can be obtained by utilizing full-field illumination and 2D area scan detector, referred as FF-OCT [30], [70]. Various FF-OCT frameworks have been employed utilizing 2D smart pixel silicon detector arrays [70] and CCD cameras [65], but in these frameworks for obtaining the depth structure of a sample the axial mechanical scanning of the reference arm must be performed.

1.5 COMPUTER AIDED DIAGNOSIS APPROACH

In the medical imaging field, doctors have to deal with images for analysing the abnormalities in a very short time. Imaging is the basic modality to diagnose any kind of disease at a very earliest stage with the assumption of the acquisition of image not harms any human body as image analysis is a very crucial task. Various imaging modalities such as X-ray, ultrasound, magnetic resonance imaging (MRI), endoscopy etc. have been investigated for providing images but sometimes they harm the human body [74]–[76]. For the quantitative and objective analysis, it is possible to develop computer aided diagnostic tool which automatically help the doctors to check the abnormalities in any kind of disease [77]. Computer-aided diagnosis (CAD) is the method to assist physicians to take diagnostic decisions with computer analysis correctly. CAD systems cover much advancement in pattern recognition, signal processing, computer vision and machine learning [78], [79]. A general CAD system is illustrated in figure 1.12. A CAD system includes Image processing, Select the region of interest, Feature Extraction, Selection and Reduction, Classification and Diagnosis as shown in figure 1.12.

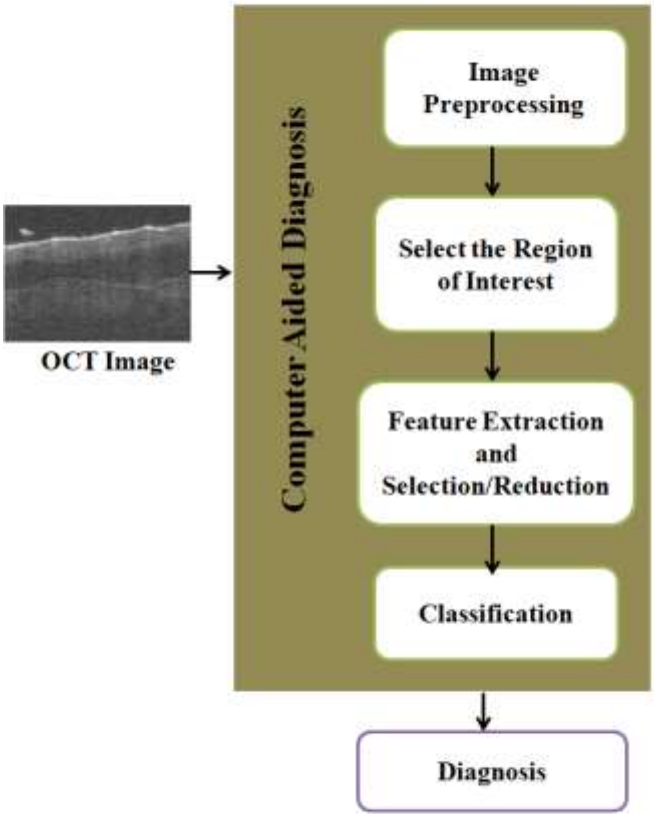

Figure 1.12 General representation of CAD system

In image pre-processing, quality of the image is improved through the utilization of enhancing, noise removal and standardization procedures. Pre-processing is fundamental in light of the fact that the viability of continuing advances like meaning of region of interest (ROI) and feature extraction are reliant on the quality of the input images. Determination of ROI is essential to isolate the objects of interest from the background. The significance of ROI in medical imaging can be characterized by (i) manual or semi-automated techniques, which requires manual interaction or (ii) completely fully automated methods, which don't require any manual intervention. Feature extraction alludes to identify and choose a lot of recognizing and adequate features from medical images for decision making with respect to the pathology of a tissue. Transforming and extracting a lot of helpful features from the input dataset is called feature extraction. Further, classification is the way toward separate objects into various classes. In medical imaging, classification is typically performed on a tissue or cells to recognize its healthy and infected state and distinctive phases of the disease. A classifier is regularly trained utilizing a training set, where at least one specialist has assigned labels to a set of objects. The term ‘machine learning’ refers to a set of algorithms which builds the computers with data-driven learning ability [80]. Machine learning has sparked tremendous interest over the past few years, a branch of machine learning that employs multilayered neural networks [81], [82]. The machine learning benefits in QPI applications that the classification and identification of cells and tissues for fast screening and diagnostic purposes. Various machine learning methods like neural networks, support vector machine (SVM), naive bayes classifier, random forest classifier, decision tree and adaboost etc. have been designed so far to make accurate classification systems for various medical images [15], [83]–[85].

In the field of applying machine learning for image analysis, extraction of meaningful features is very important to get the desired results using machine learning which demands expertise. To overcome this challenge deep learning (DL), also known as deep hierarchical learning, will be a potential tool which can automatically learn an effective feature representation for a specific problem, thus avoiding the complicated method of manually extracted feature [86]–[88]. In the present scenario, deep learning has achieved record-breaking performance to study diseases in the brain [76], [89], skin [90], lungs [91], blood cells [92], [93], and eye [94]. Recent development in the field of DL makes his remarkable impact in the field of artificial intelligence particularly speech signal processing, language processing and image processing [87], [88], [95]. DL extract features from the training data and these features were extracted at multiple levels (layers) which is called “feature hierarchies” [96]–[98]. Features are learned gradually from low-level to high-level since features at each layer are computed from the previous layer representations. Biomedical domain generally suffers from the limited amount of data and these data also contain high variability which will cause "overfitting". Due to overfitting, the features can't generalize well on data and training DL model from scratch requires extensive memory and large computational power, which limits its application in the biomedical domain. To overcome this problem "transfer learning" and "fine-tuning" would be a good solution. In transfer learning (TL), a pre-trained model is either used to fine-tuned on the limited data sets or extract features to assist in the classification task [94], [99]–[101]. In DL neural network, the first layer contains general features while the last layer contains the high-level features learned from the previous layers and therefore, they are specific. In the case of images, the major source of information is the spatial local correlation among the neighboring pixels. In that case CNN a class of DL will be a good option. In medical imaging analysis and interpretation of CNNs, a branch of DL, have an excellent record over other approaches [86], [93], [102], [103]. Thus, this will become an obvious choice for the analysis of quantitative phase imaging. The learnable weights and biases of the neurons serve as convolution filters. Different arrangement of the filters will lead to different architecture of CNN. The various transfer learning (TL) models are AlexNet, VGGNet, GoogleNet, ResNet and Inception models [99], [100], [104], [105]. These models were pre-trained on ImageNet for the classification task.

1.6 APPLICATIONS OF OCT

OCT have been widely investigated in clinical diagnosis to detect the different types of diseases [76], [106]–[110]. OCT is a young imaging modality that is still under process to find the better role play in the current medical applications [111]–[113]. During the past decades, OCT has become a suitable tool for developing high resolution, cross-sectional images in the biomedical field [52], [55], [114], [115]. The high spatial resolution allows precise investigations of both interior imaging and surface topography of any specimen. However, with the conventional methods used fiber coupler for sending and collecting the light, OCT can easily introduce into catheters and endoscopes and have been developed for intraluminal imaging [50], [116]. Further, OCT is also an important analytical tool for other biomedical applications like in developmental biology, cardiology, laryngology, gastroenterology, pulmonary medicine, dermatology, dentistry, etc. [14], [55], [117], [118]. Their histological data are evaluated by OCT, functioning as the optical biopsy to make a fast diagnosis at endoscopy. Previously, this was only feasible by using histological or cytological analysis, which is having a big problem to remove the tissue sample and processing for microscopic examination [119]–[121]. Usually, it’s a time-consuming process for the image examines manually which is very common in clinical applications. In addition, there is dependably a subjective factor related to the pathological examination of an image that builds the potential hazard for a specialist to make a false decision. In this manner, an automated framework will give important assistance to doctors. With the help of image analysis and machine learning algorithms, this research work plan to design reliable diagnostic models for analysing the medical image data to reduce the difficulties faced by medical specialists in image assessment. This thesis basically covers an OCT quantitative imaging in the applications of human skin tissues and blood samples.

1.7 GAPS IN THE RESEARCH

a) Most of biological objects and tissues are birefringent or anisotropic in nature, while conventional OCT gives only intensity image. It cannot directly differentiate between different tissues.

b) Point-by-point scanning, for 3D reconstruction of image, atleast three mechanical scan (one depth and two lateral scans) are required. The mechanical scanning system giving rise to motion artifacts due to mechanical jitter and limited repeatability.

c) Most of the biological samples are dynamic in nature hence the development of the single-shot interferometry is the need of the hour, which is only restricted by the speed of the recording device.

d) The axial resolution of the conventional OCT is governed by equation $A_r = 0.44\frac{\lambda_0^{\ 2}}{2\Delta\lambda}$ where, λ_0 is the central wavelength and $\Delta\lambda$ is the bandwidth of the light source. The axial resolution of conventional OCT is 10 micron, which is very poor for biological samples at the cellular level.

1.8 SCOPE AND MAIN OBJECTIVE OF THESIS

Based on the aforementioned problem definitions, the main objective of my research work is to develop a high-resolution OCT/ OCM system to obtain complex field (intensity and phase images) information. We also develop an image analysis algorithm that can extract the quantitative phase information from the complex field for the characterization of biological samples. In particular, the research focuses on the development of computer aided diagnosis system to investigate the various properties of normal and pathological conditions.

1.9 OVERVIEW OF THESIS CHAPTERS

The thesis has been organized into seven chapters. This section presents a brief description of the contents and division of the thesis. In the following chapters, we will give the description of each of the proposed methods and its results. Each chapter start with a literature review, elaborating on the methods and end with the most outstanding results. In the present chapter provides the review on the basics of OCT, its types and enormous aspects of FF-OCT system. Various QPI techniques along with a review of the current research are discussed. This chapter discussed about the PSI as well as OAI and how to apply in the biomedical field. Various statistical methods were discussed for the quantification of the parameters which were extracted from the images captured by the OCT system. Further, classification of the biological samples has been done by using numerous machine learning methods. We end up this chapter by discussing the brief idea about CAD systems for the ease detection of the biomedical samples and how well this method is helpful in biomedical field.

CHAPTER 2: DEVELOPMENT OF THE FULL-FIELD OPTICAL SPATIAL COHERENCE SYSTEM AND ITS CHARACTERIZATION

FF-OCM system based on spatial coherence known as full-field optical spatial coherence microscope system (FF-OSCM) has been developed. To achieve high resolution, we synthesized a pseudo-thermal light source by angular multiplexing of three diverging laser light (from the same light source) illuminating the diffuser. To reduce the speckle and spatial coherence, we generate the multiple light sources by combining the rotating diffuser and vibrating multi-mode fiber bundle (MMFB). As the spatial coherence of the light source was reduced, the obtained resolution of the developed framework is similar to temporal coherence based conventional OCT system. The developed framework was characterized in terms of temporal noise, spatial noise, axial resolution and lateral resolution etc.

CHAPTER 3: AUTOMATED IDENTIFICATION OF DIFFERENT STAGES OF MALARIA

Malaria is a life-threatening infectious blood disease affecting humans and other animals caused by parasitic protozoans belonging to the *Plasmodium* type especially in developing countries. The gold standard method for the detection of malaria is through the microscopic method of chemically treated blood smears. In the present study, 28 samples (15 healthy, 13 malaria infected stages of red blood cells) were recorded by the developed system. A multi-level ensemble-based classifier was designed for the quantitative prediction of different stages of the malaria cells. The proposed classifier was used by repeating k-fold cross validation dataset and achieve a high average accuracy of 97.9% for identifying malaria infected late trophozoite stage of cells.

Later on, customized CNN combine with multi-wavelength spatial coherence microscopic (SCM) system with the combined effect of angular, spatial, and temporal diversity to improve the diagnosis accuracy of different stages of malaria. A SCM is based on a purely monochromatic light source that delivers a narrow temporal and wide angular frequency spectrum. To overcome from limited sample size, we utilize multi-wavelength quantitative complex field imaging (both amplitude and phase). A customized CNN achieves good sensitivity and specificity in all the different stages of malaria. We believe that our proposed technique will be helpful for point-of-care testing of different stages of malaria infection without staining or expert.

CHAPTER 4: BURN TISSUE CHARACTERIZATION USING OPTICAL COHERENCE TOMOGRAPHY

In this chapter, the human skin tissue samples were imaged *in vivo* using the SS-OCT system. Burns are the most common cause of accidental death. In the worldwide population, millions of people suffer from burn injuries and need a medical assessment every year. Therefore, there is an urgent requirement of automation for the accurate assessment of burn tissues without the expert clinician. Normal and burn tissues were differentiating by extracting the morphological features from A-scan (back-scattered intensity profile) and B-scan (texture parameters) images. For the automatic detection of the burn skin from the normal skin machine learning based classifier was used. In our study, a generalized linear model was used as a classifier. The coefficient of linear model was determined by training the model on training set data and the same set of coefficients was applied to calculate the response of testing data set. The model quality was evaluated using performance curves. The result indicates that integration quantitative features from both A-scan and B-scan OCT images can be powerful *in vivo* diagnostic tool for quantitative analysis of burned tissues without a specialized facility and clinician.

CHAPTER 5: AUTOMATED BREAST CANCER MARGIN ASSESSMENT USING OPTICAL COHERENCE TOMOGRAPHY

Breast cancer is the leading cause of woman's death in the worldwide, especially in the underdeveloped countries. According to the International Agency for Research on Cancer of the World Health Organization (WHO) 2012 statistics, 8.5 million women died from breast cancer. The number of cases will significantly increase to more than 27 million by the end of 2030. We apply MEMS VCSEL SS-OCT system to classify healthy and malignant breast tissues. Our present work performs encouraging classification with the help of deep learning-based CNN model in distinguishing malignant breast tissue from normal breast tissue using OCT system. The effectiveness of the model was computed on both original and augmented datasets in terms of accuracy, loss, sensitivity, and specificity. The experimental results of the breast cancer tissue are also cross validated with the histopathology data. With more image data and addition of different classes of breast cancer will make the system more robust and support in clinician decisions. The cancer margin assessment results show the effectiveness of the model. We expect that our proposed method in future will be helpful to monitor the individual patient health progress and success of therapy by automatically extracting the hidden image information.

CHAPTER 6: PHASE SHIFTING FULL-FIELD OPTICAL COHERENCE MICROSCOPE: A TOOL FOR HUMAN BREAST TISSUE AND RED BLOOD CELLS IMAGING

Histology is the gold standard for tissues characterization due to its subcellular resolution. However it's time-consuming and would not possible intraoperative. Full-field optical coherence microscope (FF-OCM) is an alternative high-resolution enface imaging technique which doesn't need any sample preparation. In this chapter, a FF-OCM system is designed with the configuration of Mirau interferometer and 2D three-chip color camera. Further, the system is used to study human breast cancer tissues and stored RBCs. To extract the phase information five-step phase-shifting algorithm is used. The system shows a great potential for imaging breast tissue and RBCs.

CHAPTER 7: CONCLUSIONS AND FUTURE SCOPE

In this chapter, we summarize the results of the chapters and assess the future prediction.

CHAPTER 2

DEVELOPMENT OF FULL-FIELD OPTICAL SPATIAL COHERENCE MICROSCOPY SYSTEM

2.1 MOTIVATION

Over the last decades, quantitative phase microscopic imaging methods, including refractive index tomography, optical diffraction tomography, digital holography quantitative phase microscopy / spectroscopy have been employed so far for the biological studies [122]–[125]. Although, all these techniques are very much successful in the biomedical field but they have also certain disadvantages. To capture the dynamic behaviour of the biological cells such as membrane fluctuations, dry mass cell density etc., an off-axis interferometry or holography is preferred since it gives complete information in a single shot whose response solely depends upon recording device speed [24], [126], [127] . Low coherence interferometry based full-field optical coherence microscopy (FF-OCM) emerges as alternative imaging techniques to produce a complex image (both amplitude and phase image) with high resolution [68]. The axial resolution is half of the coherence length and is inversely proportional to the bandwidth of the light source. Therefore, the larger the bandwidth, better the axial resolution and the lateral resolution is governed by focusing condition of the imaging system [14], [38], [116]. OCM is a powerful modality that can achieve high resolution cellular imaging. Its main property is to combine the low coherence and confocal gating for imaging the scattering media. Low coherence light source acts as coherence gate and ignores the undesired backscattered light from the specimen whereas the confocal gate avoids out of focus light by means of using a pinhole in front of detector. Hence, the combined effect of confocal and low coherence gate produces higher contrast images with a high penetration depth in the scattering medium. OCM has becomes more useful in comparison to conventional OCT or confocal microscopy due to its high contrast and improved imaging depth [73]. Its main advantage is its sub-cellular resolution with high numerical aperture (NA) objective lens with a broadband light source, simplicity, cost and speed. However, conventional OCT based on broadband light source (SLD or thermal light) basically exploits the property of low temporal coherence [52], [66]. In case of low temporal coherence, the interference will only occur when the path difference between the reference and sample arm is within the coherence length which limits the utilization of whole camera field of view [128]. The other disadvantage with a broadband light source-based system is that it required dispersion compensation mechanism for dispersion correction [38], [129]. However, these issues can be resolved with the use of high temporal and low spatially coherent light source. The major advantage of this kind of light source (high temporal and low spatially coherent) it has a high fringe density over the whole camera field of view and it doesn’t require any dispersion compensation mechanism. A narrow band or monochromatic light source with high NA objective lens would be a good solution. Previous researchers have achieved high axial resolution from the broadband light source (halogen lamp) by passing through a narrow bandpass filter, but still it has large bandwidth as compared to laser [130]. Safrani et al. studied the effect of the spatial coherence for the determination of optical tomography and layer thickness with the help of a narrow spectral bandwidth light source achieved by passing the white light through a band pass filter of 10 nm bandwidth [131], [132]. Therefore, this spatial coherence-based source is more suitable for the dynamic biological sample which has a strong dispersion or inhomogeneous spectral response.

This chapter gives the detailed information about the development of a high-resolution full-field optical spatial coherence microscope (FF-OSCM) imaging system. We synthesized a pseudo-thermal light source by angular multiplexing of three diverging laser light (from the same light source) illuminating the diffuser. To reduce the speckle and spatial coherence, we generate the multiple light sources by the combination of rotating diffuser and vibrating MMFB. As the spatial coherence of the light source was reduced, the obtained resolution of the developed system is similar to temporal coherence based conventional OCT system [131], [133]. In the present system, mirau interferometer was used which is compact, follows the common path geometry leads to the insensitive external vibrations. Also, the present system is based on slightly off-axis, which need only single interferogram to extract the phase information which will be very helpful for dynamic process such as RBC [46], [134].

2.2 METHODOLOGY

Coherence properties of optical light sources play a significant role in the various optical imaging techniques such as interferometry, QPM, digital holography, and OCT [13], [38], [52], [130], [135]. Coherence is broadly divided into two parts: spatial and temporal coherence [63], [129]. The spatial coherence is further divided into two sub-categories: lateral and longitudinal spatial coherence [63], [129]. Spatial coherence gives the correlation of different optical fields at two different spatial positions, placed either longitudinal or lateral direction of the beam propagation, at the same moment of time [13], [136] whereas temporal coherence gives information about fixed or constant phase relationship, i.e., correlation between light sensations at two different moments of time. In the coherence theory of optical fields, the temporal coherence function is determined by Wiener-Khintchin theorem while spatial coherence function is determined by Van-Cittert Zernike theorem [63]. According to Wiener-Khintchin theorem, for a broad light source spectrum source frequency spectrum is the Fourier transform of the temporal coherence function [137]. Similarly, according to Van-Cittert Zernike theorem, source spatial distribution is the Fourier transform of the spatial coherence function [63].

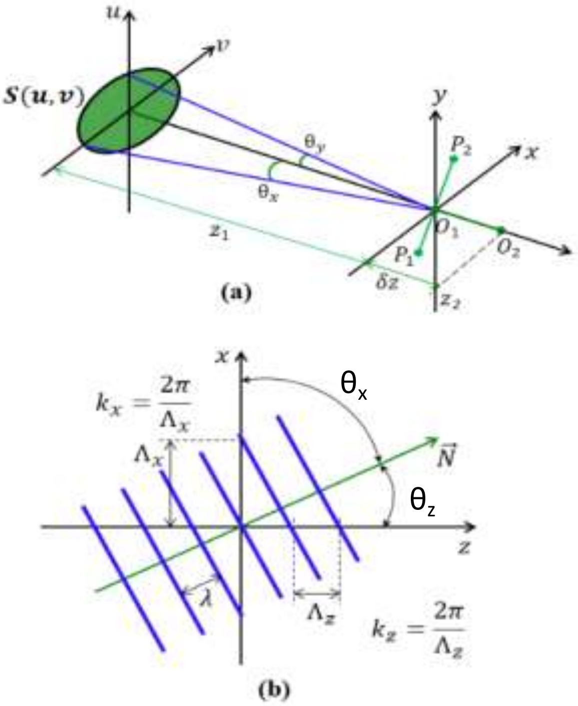

Figure 2.1 (a) Spatial coherence to the extended light source and (b) spatial periods and circular frequencies of a plane wave.

For spatially longitudinal incoherent light source, the coherence length is found by longitudinal spatial coherence (LSC) length instead of temporal coherence as in the case of low coherence interferometry [13], [63]. The LSC length of the spatially extended light source is defined by

$$\gamma_{long}(z_1, z_2) = \int_{-\infty}^{\infty} S(k_z)\exp(ik_z\delta z)dk_z \tag{2.1}$$

where, $\gamma_{long}(z_1, z_2)$ = LSC of the light source

$S(k_z)$= angular spectrum of the light field

k_z = longitudinal spatial frequency

$\delta z = (z_1 - z_2)$, difference between two-spatial points O$_1$ (z_1) and O$_2$ (z_2) in the observation plane as shown in figure 2.1 (a).

$$k_z = \frac{2\pi}{\Lambda_z} = \frac{2\pi}{\lambda} \cos\theta_z \tag{2.2}$$

where, Λ_z = spatial period along Z-direction as shown in figure 2.1(b),

λ = wavelength of the light source,

θ_z = angle between the z-axis and direction of propagating field,

The longitudinal coherence length is defined by

$$L_c = \frac{2\pi}{\Delta k_z} \tag{2.3}$$

where, Δk_z is the longitudinal spatial frequency range.

The longitudinal coherence frequency, which depends upon the temporal frequency as well as angular frequency is given by

$$L_c = \left[\frac{2\sin^2\left(\frac{\theta_z}{2}\right)}{\lambda_0} + \frac{\Delta\lambda}{\lambda_0^2} \cos^2\frac{\theta_z}{2}\right]^{-1} \tag{2.4}$$

where, λ_0 = central wavelength of the light source,

$\Delta\lambda$ = temporal spectrum width of the source

θ_z = half of the angular spectrum width.

For monochromatic light source $(\Delta\lambda << \lambda_0)$ expression (2.4) becomes

$$L_c = \frac{\lambda_0}{2\sin^2\left(\frac{\theta_z}{2}\right)} \tag{2.5}$$

hence, the axial resoloution (half of the coherence length, i.e. $\frac{L_c}{2}$) is determined by LSC rather than temporal coherence [129].

The lateral resolution is calculated by [136],

$$L_S \cong \frac{0.61 \times \lambda_0}{NA} \tag{2.6}$$

where, L_S = lateral resolution of the light source.

2.3 EXPERIMENTAL DETAILS OF THE DEVELOPED SYSTEM

Each component specifications are given in the table 2.1.

Table 2.1 Experimental Set-up Components

Components	Specifications
Laser Light Sources	Helium-Neon Lasers, wavelengths-Red 632 and Green 532 nm
Microscopic Objective Lens	Nikon Eclipse 50i
Beam Splitter	Thorlabs, Visible Non-polarizing beam splitter cubes
MMFB	0.1 core diameter, 100 fiber bundles
Rotating Diffuser	Thorlabs, Unmounted Ground Glass diffuser
Neutral Density Filter	Thorlabs, 0.1 OD, 79.5% transmission, 12.5 mm unmounted, metallic neutral density filter
Collimating Lens	Thorlabs, focal length ~ 17.5 mm
2-D CCD Camera	SamBa EZ-140, Sensovation AG, full well capacity =14500 e-, fps = 30, C-mount
Condenser Lens	Thorlabs, optical crown glass
Mirau Interferometer	20X, Edmund Optics, NA 0.4, Working Distance 4.7 mm, Resolving power 0.69
Mirror	1X Plane Mirror
Coupler	Thorlabs, 50×50 Fiber Coupler

CCD Camera: It is a 2-D CCD camera with image size 1392×1040 pixels and pixel size $4.65 \times 4.65\ \mu m^2$. The quantum efficiency for the camera is above 70% as shown in figure 2.2 for both the wavelengths (red and green).

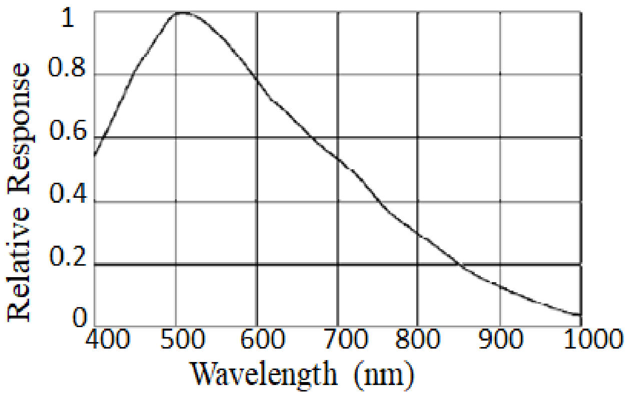

Figure 2.2 Response spectrum of a typical CCD Camera

Mirau Interferometer: The developed system uses a 20X magnification Mirau-interferometric objective lens as seen in figure 2.3(a) and (b). Mirau interferometer is compact, which allow us to integrate it into the microscope and nearly common-path geometry which leads to high phase stability and insensitive to the external noises.

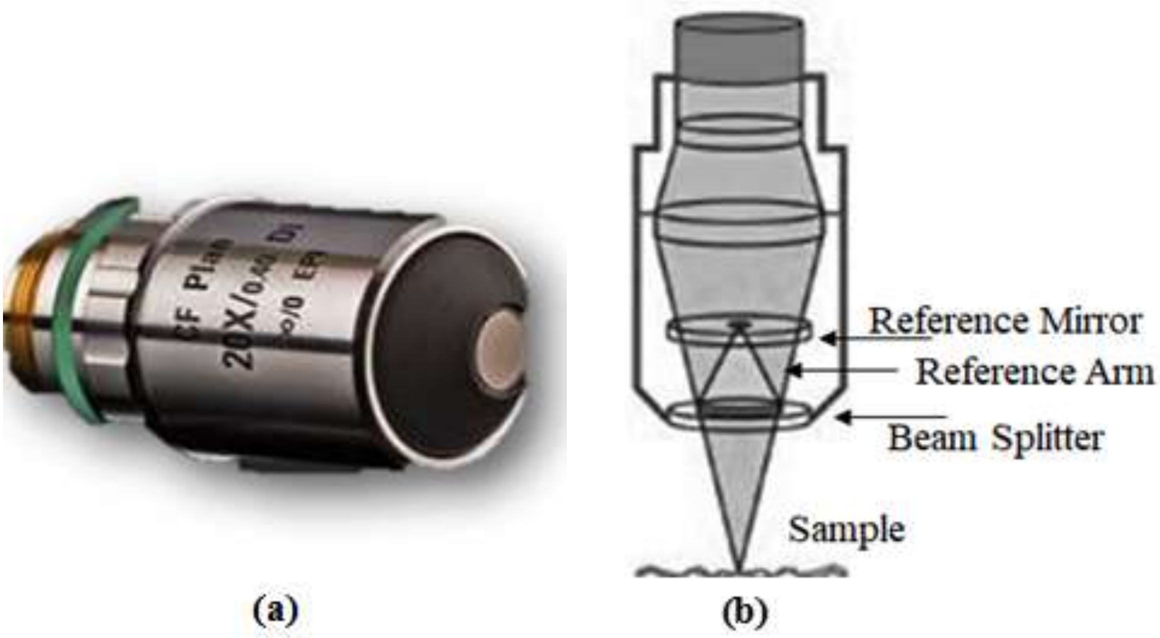

Figure 2.3 (a) 20X Mirau Interferometer (b) Schematic view of Mirau Interferometer

Experimental Description: The schematic diagram of the experimental setup is shown in figure 2.4. Two He-Ne lasers (632 nm and 532 nm) are used as light sources. Only one light source is used at a time. The red laser (632 nm) was incident onto the beam splitter (BS_1), which splits the beam into two parts, one part is going to microscopic objective (MO_1) another part is going towards MO_2. MO_2 is coupled with 50/50 fiber based beam splitter. A neutral density (ND) filter is placed in the direct beam path to equalize the intensity of all three beams. All the three diverging He-Ne laser light illuminates the rotating diffuser at an angle of $+40^0$, 0 and -40^0, respectively as shown in figure 2.4.

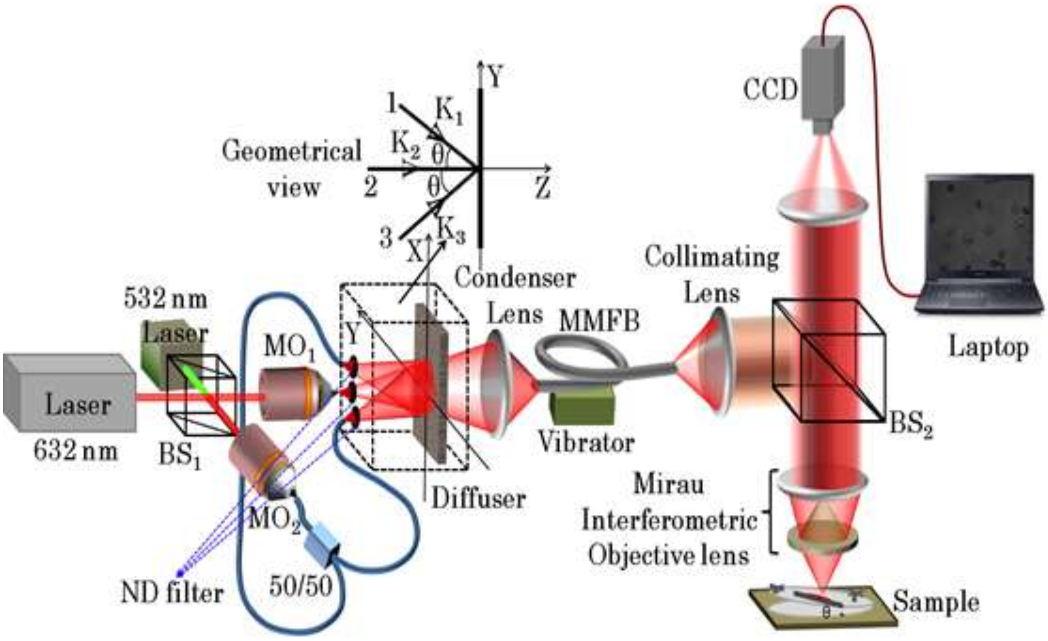

Figure 2.4 Schematic Diagram of FF-OSCM system; BS_1, BS_2-Beam Splitter, MO_1, MO_2-Microscopic objective lens, MMFB-Multi-mode Fiber Bundle, ND filter- Neutral density filter.

40° angles between the light beams is chosen to make speckle patterns generated from all three diverging beams statistically independent to reduce speckle contrast effectively. The intensity of all the three beams at the diffuser plane was approximately equal to ~ 1 mW/cm^2. The spot size on the diffuser plate is ~6 cm. The output light of diffuser is collected by a MMFB with a core diameter 1mm and contains 100 fibers of 0.1 mm core diameter each. MMFB furnishes an assembly of different modes with various stage speeds as different light beams and hence different phase delays are produced. The vibrated MMFB was further used to reduce the speckles. Thus, the yield originates from the MMFB acts as mutually spatially incoherent point sources therefore, the phase is completely randomized. The scattered output light of the MMFB is fully spatially incoherent is collected by a collimating lens (focal length ~ 17.5 mm) and fed to the microscope. The emerging collimated light was made incident on 20X Mirau interferometer, the transmitted light goes to the sample placed a slightly off-axis mirror, while the reflected beam is directed to an aluminized spot on the front surface of the microscope objective. The two beams recombine at the beam splitter and the interference pattern is recorded by the CCD camera. The field of view of the FF-OSCM image at CCD camera is 400 µm x 400 µm and the imaging speed of the system is 15 fps. The sensitivity of the FF-OSCM system is ~86 dB.

2.4 PERFORMANCE CHARACTERISTICS OF FF-OSCM SYSTEM

2.4.1 Axial Resolution

Axial resolution depends upon the coherence length of the light source and it scans that samples the light reflected back from the different depth positions [138]. The axial resolution is calculated experimentally by moving the sample mirror along the axial direction (z-direction) by a step size of 1µm. As the sample mirror moves in +z and –z direction the fringe visibility or contrast reduces. The envelope of this fringe contrast is coherence envelope and the LSC is the full-width half maxima of the coherence envelope.

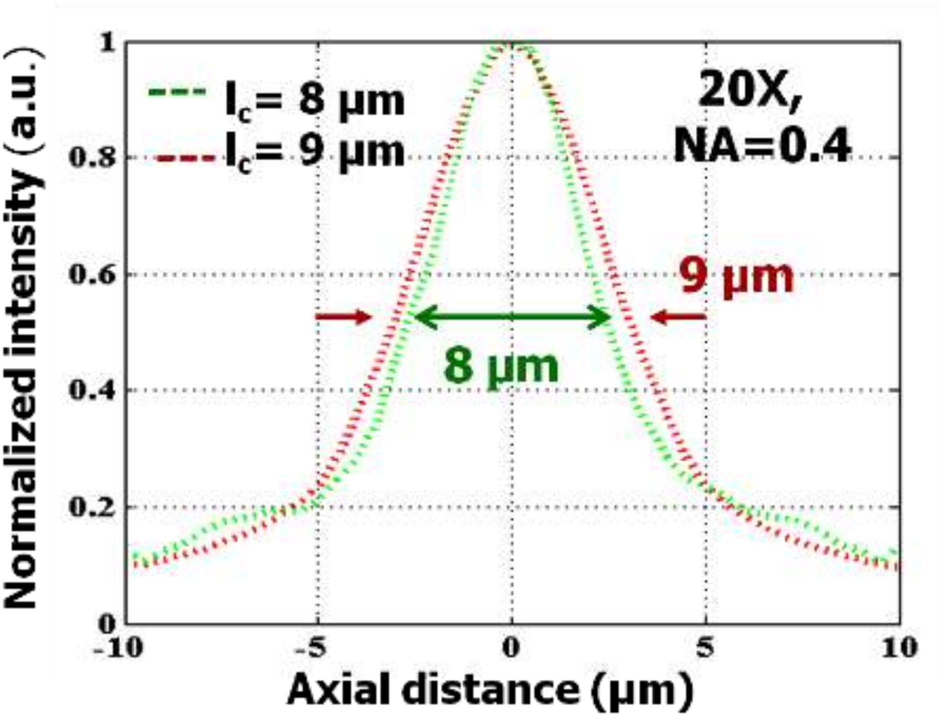

Figure 2.5 Axial resolution (half of the LSC length) with NA 0.4 (20X).

The axial resolution is the half of LSC length. Two different wavelengths red and green with objective lens (NA=0.4) are used in the experiment for the determination of the LSC or axial resolution as shown in figure 2.5. The measured axial resolution for red and green wavelength is 4.5 µm and 4 µm in the air, respectively whereas calculated value of the axial resolution from equation (2.5) is 3.78 µm and 3.18 µm for red and green in the air, respectively.

2.4.2 Lateral Resolution

Lateral resolution gives information that it moves the exploration point laterally in the second dimension [30]. To measure the lateral resolution of the system, we placed United States Air Force (USAF) test target as the sample, which was imaged using 0.4 NA objective lens. The system is able to resolve 6th elements in the 7th group element and the lateral resolution comes out to be 1.9 µm for red color wavelength as shown in figure 2.6 (a) and (b).

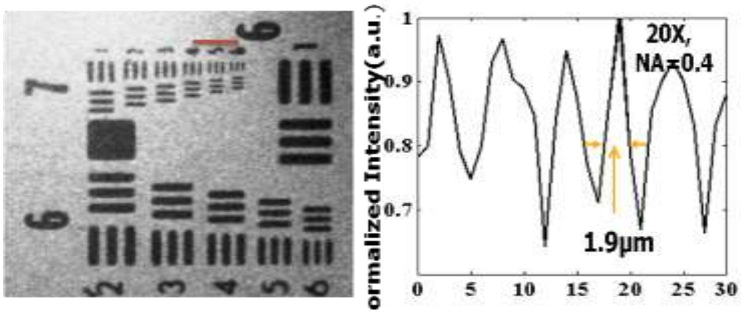

(a)

(b)

Figure 2.6 (a) Standard USAF resolution chart and (b) Normalized line profile of 6th elements in 7th group for red color wavelength.

The calculated value of lateral resolution from equation (2.6) is 0.96 µm and 0.81 µm for red and green, respectively. The measured lateral resolution through OCM intensity image is 1.9 µm and 1.1 for red and green color wavelength, respectively. There is a slight variation of lateral resolution of OCM measurement with optical microscope it may be due to the image edge contrast is not sharp, which could affect the final result.

2.4.3 Spatial and Temporal Phase Sensitivity

The spatial phase sensitivity of the system gives information of the spatial phase changes in the reconstructed phase map, which can be computed by imaging a standard flat mirror [139]. However, the temporal phase sensitivity describes the stability of an interferometer, which further leads to compute membrane fluctuations of the various biological cells [140].

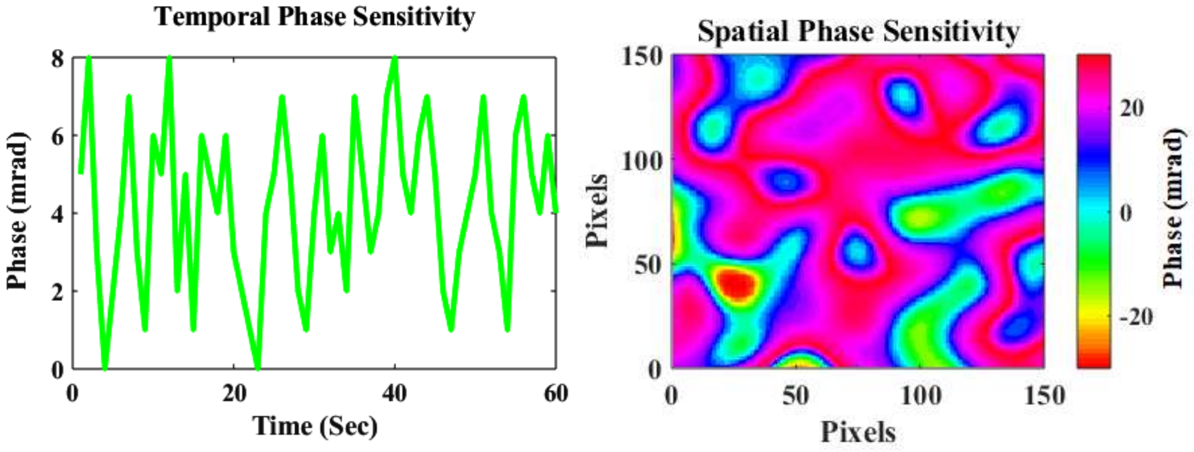

(a) (b)

Figure 2.7 Phase sensitivity of the present system (a) Temporal phase sensitivity and (b) Spatial phase sensitivity.

High spatial and temporal phase sensitivity is a very important feature of any quantitative phase microscopic system. The combination of the angular diversity (three beams of the same light source), vibrating fiber bundle and rotating diffuser will lead to an increase in the spatial phase stability of the interferometer. However, the temporal phase stability depends on the configuration of the interferometer. Since, Mirau interferometer follows the common path geometry and compact unit, so, the temporal phase stability of the developed system would be quite high. To calculate the phase stability, we placed an unprocessed clean 100 µm thickness glass cover slip and recorded 25 phase shifted interferograms and from these interferograms 25 phase images of the top of cover slip is recovered. From this, we computed spatial standard deviation of the phase images vs time. The median value of the phase is ~10 mrad. The corresponding recovered phase map is seen in figure 2.7(b). It can be shown from figure 2.7(b), recovered phase values are not same at each spatial location of the phase image.

2.4.4 Effect of angular diversity with rotating diffuser and vibrating MMFB on recorded interferogram

The developed system is used to record the interferograms of RBCs and it is seen from the figure 2.8(a) and (b) that the quality of the recorded image without angular diversity, rotating diffuser and non-vibrating MMFB is quite poor as compare to the quality of image recorded with the help of pseudo thermal light source (angular diversity, rotation diffuser and vibrating MMFB).

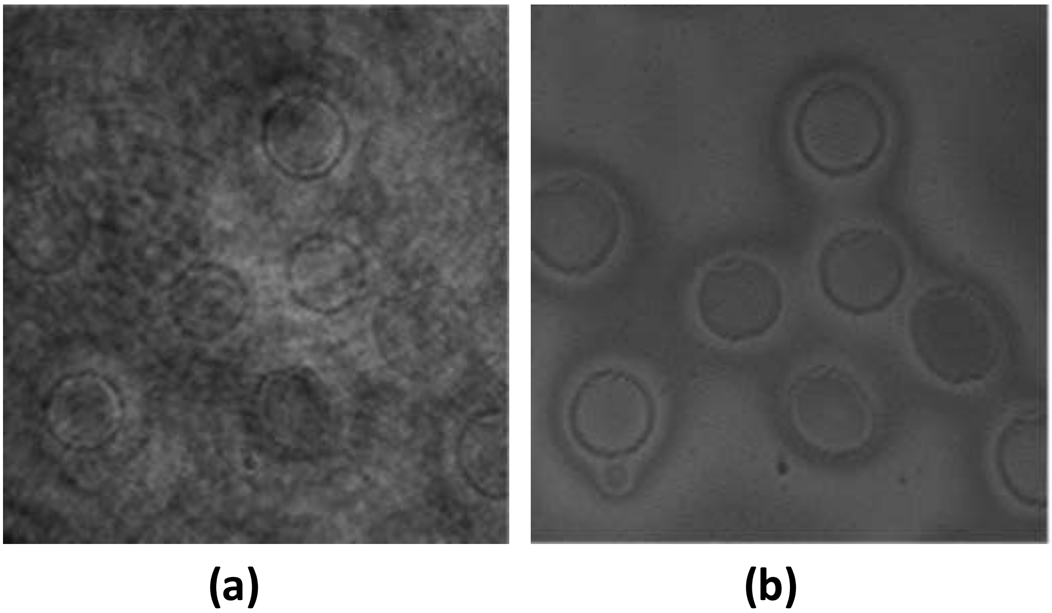

Figure 2.8 Interferograms recorded from (a) He-Ne laser light source without angular diversity, rotating diffuser and non-vibrating MMFB and (b) with pseudo thermal light source (angular diversity, rotation diffuser and vibrating MMFB).

2.5 METHODOLOGY

2.5.1 Data Acquisition

In the data acquisition, our system uses LabVIEW software written program to control the 2-D CCD camera in synchronization with the single shot recording. We used a National Instruments PXI-1031 board to send instructions and receive data and get a synchronous scanning and recording.

2.5.2 Data Analysis

To extract the phase information, the recorded interferogram of the various techniques has been applied such as Fourier transform, Phase-shifting and Hilbert Transform [141],. Hilbert transform is a powerful technique to extract the phase information from the single slightly off-axis interferogram [44], [45], [141], [142]. It has been widely utilised in the FF-OCT/ OCM system because of its computational efficiency and the simple to use. The perfect Hilbert transform algorithm is considered as a phase-shifter which provides every sinusoidal function a phase shift of $-\pi/2$ and is capable for obtaining the envelope corresponding to the original interference signal [45]. The Hilbert transform of any real-valued function u(t) is termed as:

$$h(x(t)) = HT\{u(t)\} = \frac{1}{\pi} P \int_{-\infty}^{+\infty} \frac{u(t)}{x-t} dt \tag{2.7}$$

where, P is the principal value taken in the integral. Computationally, h(x(t)) can also be written as:

$$h(x(t)) = \frac{1}{\pi x} P * u(t) \tag{2.8}$$

As mentioned above, the Hilbert transform can be assumed to be a filter that simply shifts the phase of its input by $-\pi/2$ radians. The analytic representation of an input signal is an analytic signal. The real and imaginary parts of a complex analytic signal $U(t)$ can be obtained as follows:

$$U(t) = u(t) + jh(t) \tag{2.9}$$

The analytic signal $U(t)$ can also be expressed in terms of its time-variant magnitude $M(t)$ and phase ϕ(t) in polar coordinates:

$$U(t) = M(t)e^{j\emptyset(t)} \tag{2.10}$$

M (t) can be regarded as a slow-varying envelope of U (t), while the phase derivative $\partial\emptyset(t)/\partial t$ is an instantaneous frequency [214]. Then, the magnitude $M(t)$ and wrapped phase ϕ(t) is simply determined by:

$$M(t) = |U(t)| = \sqrt{u(t)^2 + h(t)^2} \tag{2.11}$$

$$\phi(t) = \tan^{-1}\left(\frac{h(t)}{u(t)}\right) \tag{2.12}$$

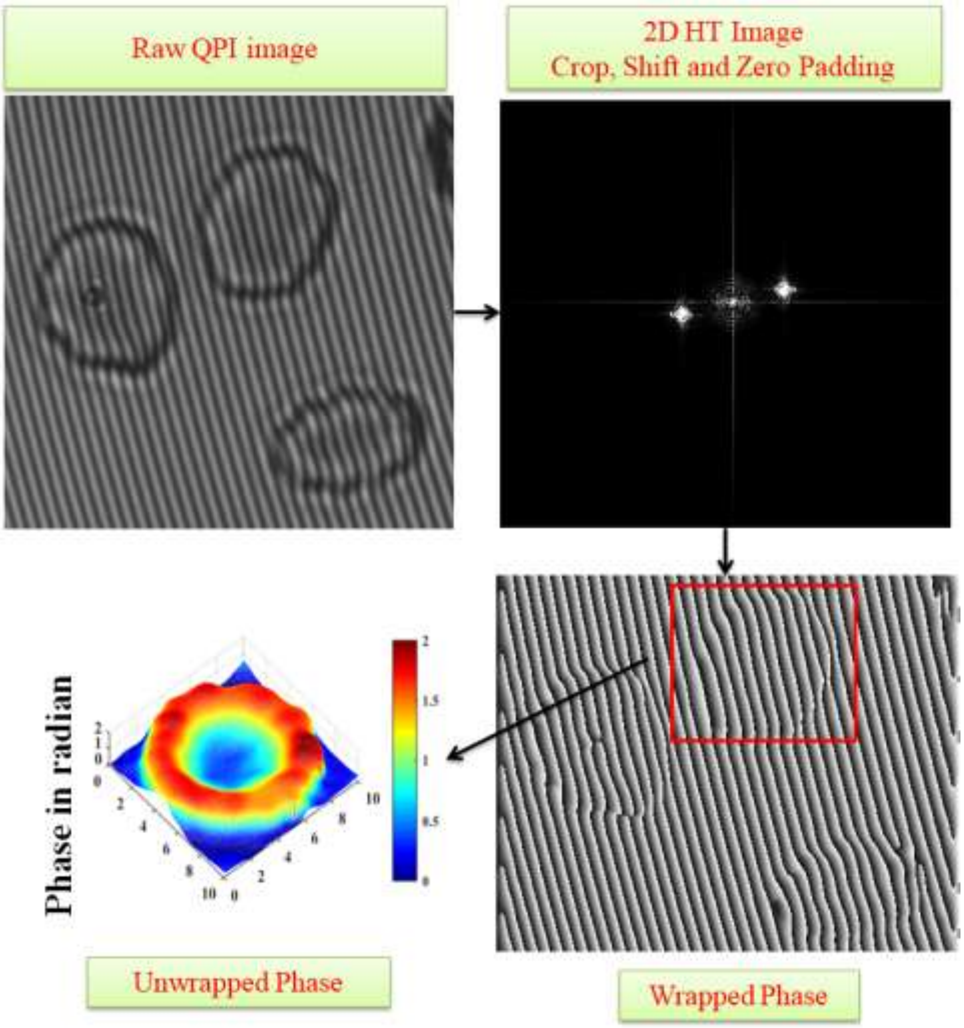

Figure 2.9 Phase extraction process from the recorded interferogram

Spatial interferograms were recorded by the developed FF-OSCM system. The phase map is extracted with the help of Hilbert transform. The dc component from the Fourier spectrum was removed and the inverse Fourier transform was then computed to obtain the complex analytical signal. The phase map was extracted from complex analytical signal by using equation no. 2.12. The Goldstein method was then used to obtain the unwrapped phase map. The whole process is explained in the figure 2.9.

2.6 CONCLUSIONS

In summary, this chapter provides a complete detail about the development of high-resolution FF-OSCM system based on pseudo thermal light source. In order to improve image quality, the concept of angular multiplexing was introduced. A pseudo-thermal light source with a combined effect of spatial, angular and temporal diversity has been designed to achieve a high resolution. A rotating diffuser and vibrating MMFB were used to further improve image quality or to reduce speckle. The developed system resolution is comparable to the conventional OCT system based on temporal coherence. In addition, the temporal and spatial phase sensitivity of the developed system is quite high. As the developed system based on a monochromatic light source, therefore, it does not require any chromatic abbreviation correction (as required in the case of broadband light sources based system). Moreover, this system is based on slightly off-axis interferometry that needs only single interferogram for extracting the quantitative information. The system is very helpful especially for studying the dynamic biological samples, as its performance only depends on the speed of the recording device.

CHAPTER 3

AUTOMATED IDENTIFICATION OF DIFFERENT STAGES OF MALARIA

3.1 INTRODUCTION

Malaria is a contagious disease via female Anopheles mosquito bite from one infected person to the healthy person having an adverse effect on the blood as seen in figure 3.1. According to 2015 statistics, 214 million malaria-infected cases were reported causing an approximate death toll of 438,000 worldwide [26], [143]. From the WHO record, the growing age children were more affected by the malaria parasite disease in the rural areas [143]. Identify the parasite itself in the RBCs and the response of the blood cells is an indication of malaria. It is mandatory to know the early stage malaria diagnosed from the patient's blood to avoid the risk of death and long-lasting infection, which increases the malaria associated diseases [26], [144], [145]. Different stages of malaria-infected RBCs are early and late trophozoite. In general, in early trophozoite stage, no change in size and two or more chromatin dot present on it while in late trophozoite stage, vacuolated and dark pigment occur on RBCs. The identification of different stages of malaria will be helpful to assess the impact of promising antimalarial medications, and antibodies focusing on the distinctive erythrocytic phases of Plasmodium falciparum (P. falciparum) parasites [146]. Due to the low cost and renowned method, microscopic testing is the gold standard technique for the diagnosis of malaria [144], [147], [148].

Figure 3.1 Female Anopheles mosquito

3.2 DIAGNOSIS OF MALARIA INFECTED RBCs USING MACHINE LEARNING

In the last decades, various microscopic imaging methods have been employed for the malaria infected stages of cell studies by using structural, biochemical and mechanical features. However, there are few limitations of these techniques, either they are suffering from poor interference signal contrast for deep layers or system is too complex [26], [125], [144]. But, the present system is based on slightly off-axis, which need only single interferogram to extract the phase information which will be very helpful for the study of behaviour of cells such as RBC [46], [134]. For the early diagnosis and fast screening process, machine learning models used in medical imaging-based applications. Further, to overcome the complications for assessing the high dimensional data and minimizing the diagnostic errors, machine learning automation systems is used [87], [88], [122], [125], [149], [150]. Initially, we have used various machine learning models individually to classify the malaria infected RBCs and healthy RBCs, but their performance is not up to a satisfactory level (accuracy < 95%). To attain the higher accuracy, sensitivity, and specificity, we designed multilevel ensemble machine learning model using morphological features dependent on quantitative phase images rather than intensity images for the classification. The feature reduction technique is applied to the datasets, it helps in reducing the computational time. The developed FF-OSCM system (discussed in chapter 2) with machine learning based ensemble model has a high accuracy for automated identification of malaria infected stages. In the beginning of this chapter, we report the automatic identification of malaria infected unstained blood samples from the novel multilevel ensemble classifier model using FF-OSCM system.

3.2.1 Sample Preparation

28 blood samples were collected from the hospital. Out of which, 15 healthy and 13 malaria infected stages of RBCs (5 early trophozoite and 8 late trophozoite) and stored into Ethylene diamine tetra-acetic acid (EDTA) anticoagulant tubes. RBCs samples were firstly diluted in phosphate buffer saline (pH~7.4) solution to maintain the cellular microenvironment and centrifugalized, and then gave some time for the cell settlement. Thin blood smears were formed on aluminium coated reflection type glass slide. The sample stage is slightly tilted (tilt angle ~8^0) to increase the fringe density and the interferograms were recorded with the help of the FF-OSCM system. With the help of numerical focusing, we choose the best contrast interferogram or the bottom most axial layers of the RBC's, which

have complete information of the RBCs because the height of RBC is less than axial resolution of the system.

3.2.2 System methodology

FF-OSCM system was used for obtaining the images of healthy and malaria infected RBCs. The detail of the system was already discussed in section 2.3.

3.2.3 Results and Discussion

In this section, an automated FF-OSCM system was used to discriminate malaria infected stages of RBCs from the healthy RBCs. Spatial interferograms were captured using the different wavelengths (red and green) of two light sources (one light source used at a time) from the region of interest (ROI) to generate the amplitude and phase ($\Delta\emptyset(x, y)$). The phase images of RBCs at different stages are shown in figure 3.2 for red wavelength. In total, 13 morphological features were computed from 13 malaria infected patients (5 early trophozoite and 8 late trophozoite stages) and 15 healthy patients are summarized in table 3.1. Samples of the total of 28 subjects with an average of 20 RBCs from healthy and 24 RBCs from infected stages per subject were measured. The total RBC images were - 300 healthy RBCs, 120 early trophozoite RBCs and 192 late trophozoite RBCs was analysed. Once, the slightly off-axis spatial interferograms were recorded for red wavelength. The recorded spatial interferogram was Fourier transformed, positive or negative first order spectrum was filtered by spatially filtered and then inverse Fourier transformed was performed to obtain wrapped phase. Phase unwrapping is performed by Goldstein's method [17].

A number of quantitative features extracted from the phase images of RBCs are major axis length, minor axis length, elongation, eccentricity, perimeter, area, maximum phase value, minimum phase value etc., as mentioned in table 3.1. Similar, analysis had been performed for green wavelength also. The extracted parameters from the phase images for both the wavelengths (red and green) were average out, which will further reduce the coherent noise artifacts [151]. The quantitative changes in the mean values of the size dependent features area and perimeter are seen in table 3.1. In the case of malaria infected stages (early trophozoite and late trophozoite) of RBCs, the mean value of the eccentricity feature increases, so the samples are distorted from its normal shape. There are other important features that also be used for discriminating malaria infected stages against the healthy one, which are computed from the phase profile of the cells.

Table 3.1 Morphology features based on RBCs phase images of the healthy and malaria infected stages of RBCs from the mean values of red and green wavelength

Features	Definition	Mean values of malaria infected stages of RBCs (red and green wavelength)		Mean value of healthy RBCs (red and green wavelength)
		Late trophozoite stage	Early trophozoite stage	
Major Axis Length of RBC cell (µm)	a	8.192	8.318	9.313
Minor Axis Length of RBC cell (µm)	b	7.056	7.314	8.649
Elongation	a/b	1.173	1.154	1.078
Eccentricity	$\frac{\sqrt{\left(\frac{a}{2}\right)^2-\left(\frac{b}{2}\right)^2}}{a}$	0.472	0.439	0.344
Max phase value (radian)	$\Delta\phi_{\max}(x,y)$	3.086	2.669	2.032
Average phase value (radian)	$\overline{\Delta\phi}(x,y)$	1.165	1.028	1.186
Median phase value (radian)	$\widetilde{\Delta\phi}\,(x,y)$	1.014	0.936	1.335
Area (µm^2)	$\pi ab/4$	45.489	47.92	63.335
Perimeter (µm)	$2\pi\sqrt{\frac{a^2+b^2}{2}}$	25.33	26.138	29.60
Standard deviation of phase(radian)	$\frac{\sqrt{\sum\left(\Delta\phi(x,y)-\overline{\Delta\phi}(x,y)\right)^2}}{N}$	0.799	0.669	0.574

Variance of phase (radian)	$\frac{\sum \left(\Delta\phi(x,y)-\overline{\Delta\phi}(x,y)\right)^2}{N}$	0.638	0.447	0.329
Symmetry	$Mean\left[\frac{(\Delta\phi(x,y)\cdot\Delta\phi(x',y'))}{\|\Delta\phi(x,y)\|^2}\right]$	0.868	0.857	0.983
	$Minimum\left[\frac{(\Delta\phi(x,y)\cdot\Delta\phi(x',y'))}{\|\Delta\phi(x,y)\|^2}\right]$	0.776	0.759	0.972

*where x, y represents the no. of pixels in the horizontal and vertical direction of the RBC phase image and N represents total no. of pixels of the particular phase image, respectively.

The mean values of the average phase value and median phase value are decreased, while the maximum phase value increases, as listed in table 3.1 for malaria infected stages of RBCs. Mean phase values of all the samples are almost associated with a small region so standard deviation and variance are reduced for healthy RBCs, as given in table 3.1.

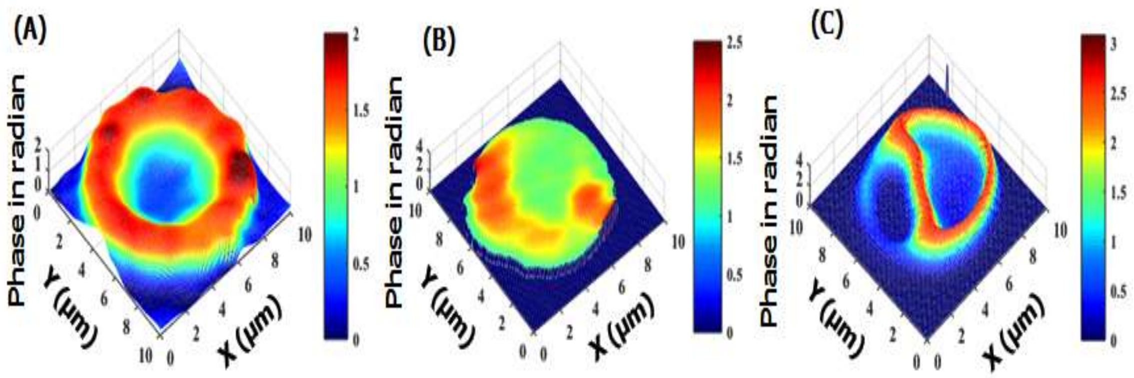

Figure 3.2 Phase images of RBC (A) Healthy, (B) Early trophozoite and (C) Late trophozoite malaria infected stages, respectively

Furthermore, symmetry is also calculated to discriminate malaria infected stages of RBC as mentioned in table 3.1, which is defined as the dot product of phase images and rotated phase images across the angles of the full rotation reference to the original phase image. We have performed student's t-test to calculate the p-value (< 0.001) for all the quantitative morphological features and highly significant results show the discrepancies occur in malaria infected stages and healthy RBCs, presented in table 3.1.

3.2.4 Description of Machine Learning Classifier

Out of 420 RBCs phase images dataset for the discrimination between the healthy RBCs and early trophozoite malaria RBCs stage, 294 images are used as a training dataset to train all the classifiers and 126 images are used as a testing dataset to acquire the response of all the classifiers mentioned in the table 3.2. The detail of the all the machine learning classifiers with tuning parameters is given in table 3.2. The methods are available in the R open source software. R is licensed under GNU GPL.

Table 3.2 Description of Machine learning Classifier

Classifier	Method	Required Package	Tuning parameters
Decision Tree [152]	Rpart	None	usesurrogate=0, maxsurrogate=0
ELM [153]	Elmtrain	elmNN	nhid=10
Random Forest [154]	RF	Random forest	mtry=2, ntree=500
SVM [155]	Ksvm	Kernlab	kernel=”rbfdot”, type=”C-svc”
RRF [156]	RRF	RRF	None
AvNNet [157]	avNNet	Caret	size, linout, trace
Neural Network [158]	Nnet	Nnet	size=10

Similar, analysis is performed for the discrimination between the healthy RBCs and late trophozoite malaria RBCs stage, but in this case 492 RBCs phase images dataset, 344 images used as training to train and 148 images used as testing to get the final result. To improve the computational time, a feature reduction technique or principle component analysis (PCA) technique was applied to the feature extracted from phase images, which having less contribution (i.e. elongation, eccentricity, average phase and perimeter) with slightly compromising with the accuracy in detecting malaria infected stages of RBCs. The remaining nine parameters were employed as a predictor and response variables to achieve the efficient results. The performance metrices and their corresponding formulae (given in equation no. 3.1 to 3.3) of all the classifiers for the detection between early trophozoite vs healthy RBC and late trophozoite vs healthy RBC is shown in table 3.3 and table 3.4, respectively. We used seven different models individually to classify malaria infected different stages of RBCs and healthy RBCs, but their performance is not up to a satisfactory level (accuracy < 95%).

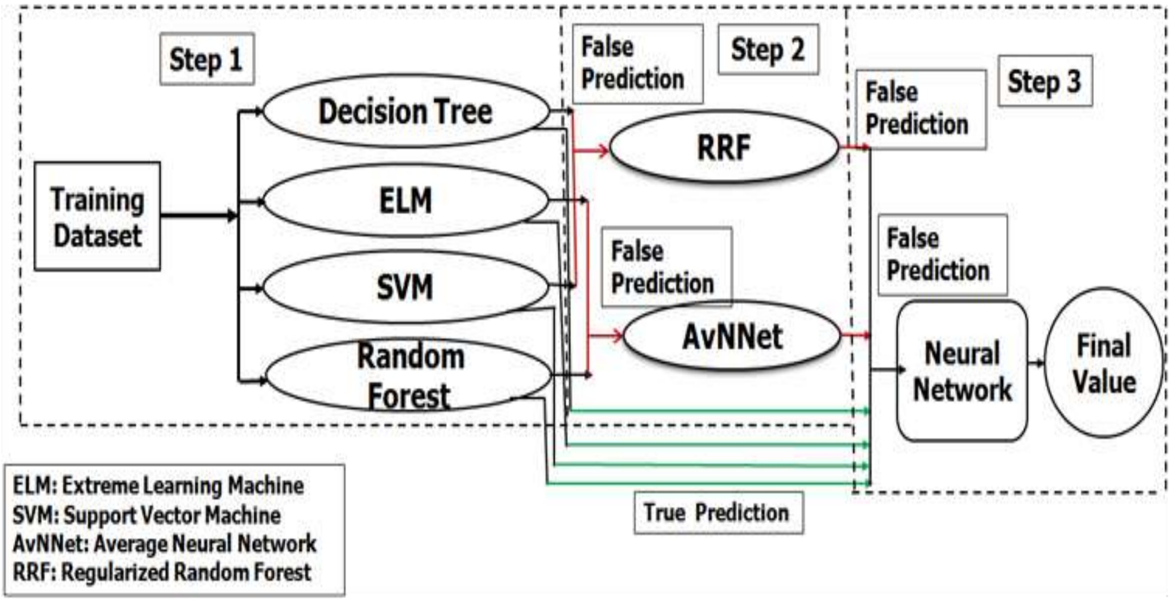

Figure 3.3 A Multi-Ensemble Model classifier.

The following performance evaluation metrics are given in equation no.3.1 to 3.3:

Accuracy: It describes the correctness performance of the classifier.

$$Accuracy = \frac{TP + TN}{TP + TN + FP + FN} \tag{3.1}$$

Sensitivity: It measures the positive class correctly as belongs to the positive cases only.

$$Sensitivity = \frac{TP}{TP + FN} \tag{3.2}$$

Specificity: It measures the negative class correctly as belongs to the negative cases only.

$$Specificity = \frac{TN}{TN + FP} \tag{3.3}$$

Mathew Correlation Coefficient (MCC): It measures the correlation coefficient between the actual class and predicted class. The MCC values lies between -1 to +1. If the MCC values close to +1 then it represents the perfect prediction otherwise disagreement results between prediction and actual class.

$$MCC = \frac{TP \times TN - FP \times FN}{\sqrt{(TN + FN)(TN + FP)(TP + FN)(TP + FP)}} \tag{3.4}$$

where, TP is the true positive or correctly predicts the positive cases, TN is the true negative or correctly predicts the negative cases, FN is the false negative or incorrectly predicts the negative cases and FP is the false positive or incorrectly predicts the positive cases.

To further improve the accuracy, sensitivity and specificity, we designed a multilevel ensemble classifier by using a different combination of individual models. The most efficient multilevel ensemble-based classifier with high accuracy, sensitivity and specificity, which includes seven classifiers is shown in figure 3.3. In this classifier, both true and false predictions are used to get accurate proposed model. For reducing the false positive outcomes, true predictions are utilized to the input of other classifiers. The models perfectly learn the data to get reliable and accurate results as the data is travelled through all models.

Table 3.3 Performance evaluation of multilevel ensemble model for early trophozoite and healthy RBCs

Classifiers	Accuracy (%)	Sensitivity (%)	Specificity (%)
Decision Tree	75.4	78.6	72.3
ELM	78.5	80.6	76.6
Random Forest	81.7	83.8	79.6
SVM	83.3	85.4	81.2
RRF	88.1	88.8	87.3
AvNNet	92.8	93.6	92.1
Neural Network	96.1	96.8	95.2

Following steps were taken to get the final value of the classifier for the determination of both malaria infected stages, In step-1, four classifiers are trained from 70% dataset and get prediction from 30% dataset and 79.5 average accuracy attained from the training dataset are given in table 5.3, in step-2, the false prediction from the two classifiers i.e. Decision tree and SVM are joined to train the RRF classifier and the false prediction from the two classifiers i.e. ELM and random forest are joined to train the AvNNet classifier and get 90.4 average accuracy as seen in table 2.3, In step-3, the true prediction from step-1 and the false prediction from step-2 are merged to train the neural network classifier.

Table 3.4 Performance evaluation of multilevel ensemble model for late trophozoite and healthy RBCs

Classifiers	Accuracy (%)	Sensitivity (%)	Specificity (%)
Decision Tree	77.7	79.4	76
ELM	80.4	82.2	78.6
Random Forest	83.1	84.9	81.3
SVM	87.2	89	85.3
RRF	91.2	93.1	89.3
AvNNet	93.9	94.5	93.2
Neural Network	97.9	98.6	97.3

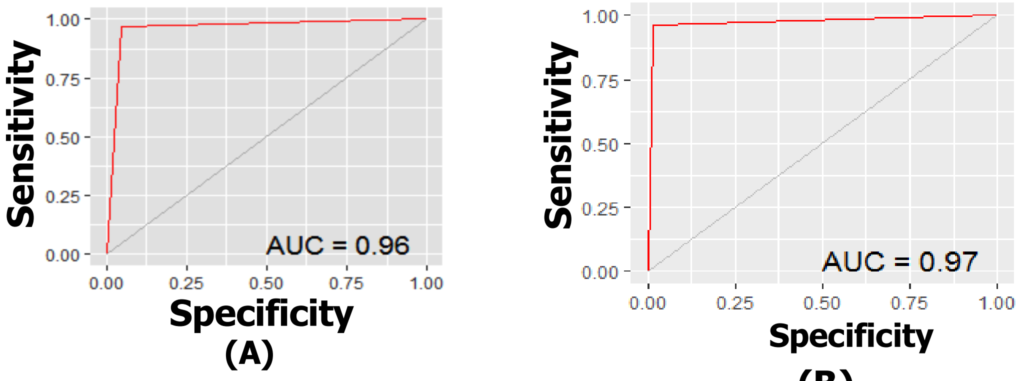

(A)

(B)

Figure 3.4 ROC curve for testing dataset (A) Early trophozoite malaria infected RBCs and (B) Late trophozoite malaria infected RBCs.

A set of classifier performance can be seen in table 3.3 and the results achieved are accuracy 96.1%, sensitivity 96.8% and specificity 95.2% for the discrimination between the malaria infected early trophozoite RBCs and the healthy RBCs. In table 3.4, the results achieved are accuracy 97.9%, sensitivity 98.6% and specificity 97.3% for the discrimination between malaria infected late trophozoite RBCs and the healthy RBCs. The proposed classifier was obtained more accuracy as compared to the single classifier as mentioned in the table 3.3 and table 3.4 for early and late trophozoite malaria infected RBCs, respectively certainly its computation time is high as compared to single classifier. Figure 3.4 shows the ROC for malaria infected stages and healthy RBCs images dataset.

3.3 MALARIA INFECTED STAGES CLASSIFICATION USING DEEP LEARNING WITH LIMITED LABELLED DATA

Several efforts have been made to use machine learning for automatic detection of malaria infection from microscopic images of stained blood cells to avoid human interpretation error [84], [147], [148]. Most of the machine learning methods such as K-NN, Naive Bayes, ANN, and SVM etc., uses morphological measurement, color features and statistical features for the classification of malaria parasite-infected RBCs [84], [159], [160] but their achieved accuracy varies from 84–95% in detecting parasites from stained blood cells [84], [125], [144]. As discussed, though there are many attempts to automate the detection of different stages of malaria based on morphological features but their sensitivity and specificity is poor due to overlapping color intensities which makes it difficult to classify early and late trophozoite as shown in figure 3.5.

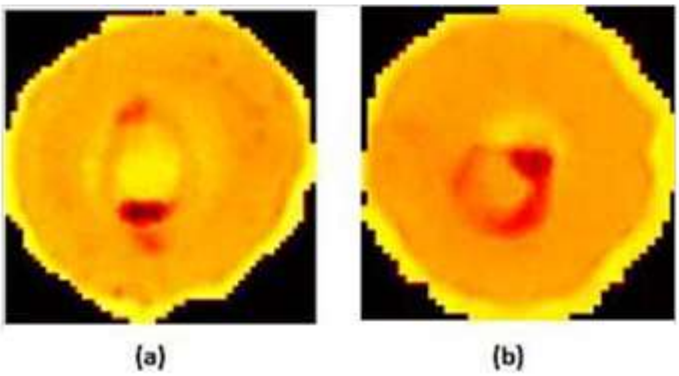

Figure 3.5 Bright field images of (a) Early trophozoite and (b) Late trophozoite RBCs, respectively.

In the case of images, the major source of information is the spatial local correlation among the neighboring pixels. In that case, CNN is a class of deep learning (DL) will be a good option for the classification [91], [161]. In medical imaging analysis and interpretation CNN's, a branch of DL, have an excellent record over other approaches [86], [91]. Thus, this will become an obvious choice for the analysis of images. Different arrangement of the filters will lead to different architecture of CNN. Biomedical domain generally suffers from the limited amount of labelled data and these data also contain high variability which will cause "overfitting". Due to overfitting, the features can't generalize well on data and training DL model from scratch requires extensive memory and large computational power, which limits its application in the biomedical domain. To overcome this problem "transfer learning" and "fine-tuning" would be a good solution. In this section, we demonstrated how a customized CNN with a multi-wavelength spatial coherence microscope (SCM) for automatic identification of different stages of malaria-infected red blood cells with limited labelled data. The cells have different absorption, emission and scattering properties with respect to each wavelength. Multi-wavelength imaging will helpful in extracting the different information embedded in it. As refractive index is a function of wavelength and is directly correlated with structural and biomechanical characteristics of the sample [162]. Multi-wavelength imaging will also increase the sample size which is necessary for data-hungry DL for automatic classification of the cells. This approach is helpful in the classification of healthy and infected (early and late trophozoite) RBCs as well as early and late trophozoite RBCs. Our approach uses multi-wavelength SCM to extract the phase information of the RBCs for each wavelength and fed it as an input to CNN, this method has not been used in the medical imaging literature so far. We also compared the performance of pre-trained CNN's (AlexNet, VGGNet, GoogleNet, ResNet and Inception models), with our customized CNN. In this study, we demonstrated how the multi-wavelength SCM system with fine-tuning customized CNN leads to comparative performance with other deeper CNN’s, but have a better performance in terms of computation time for detecting the different stages of malaria with limited number of labelled data.

3.3.1 Experimental Study of Spatial Coherence Microscope (SCM) System

For analysing the malaria infected stages of RBCs, SCM system was used. The schematic diagram of the system is presented in figure 3.6, which includes three lasers (632 nm, 532 nm and 460 nm), and the rest detail of the experimental set-up is same as given in section 2.2.

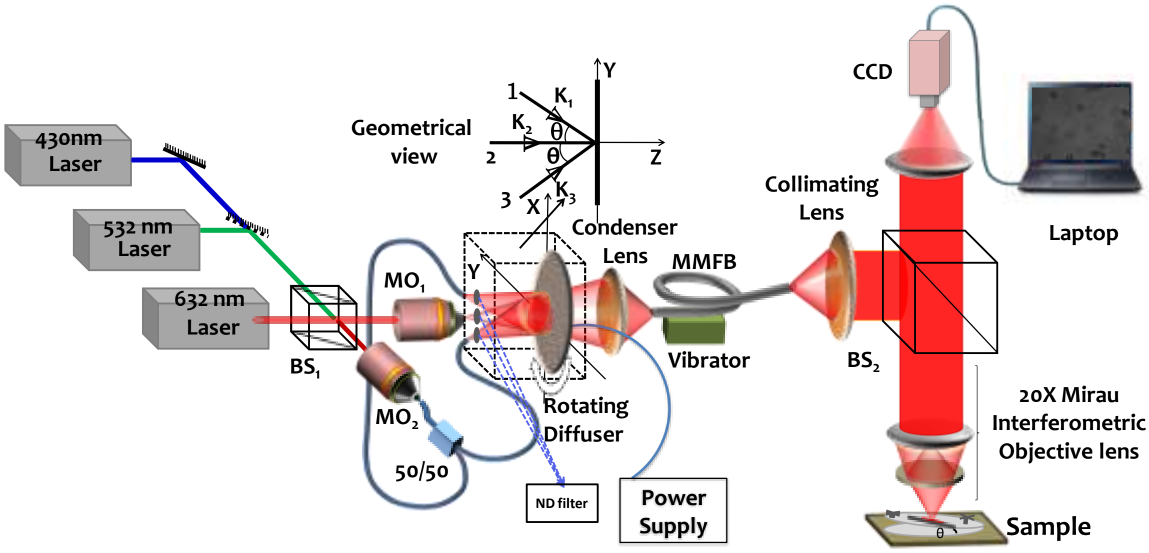

Figure 3.6 Schematic diagram of SCM system.

3.3.2 Materials and Methodology

An experimental study was conducted on 36 human blood samples and the samples were taken from Ganga Pathology lab. Blood samples preparation is already discussed in the section 3.2.1.1 .

3.3.2.1 RBC Patch Extraction

Entropy of each image of size n×n is calculated with the help of equation no (3.5).

$$Entropy = -\sum_{i=1}^{L} P_i \log P_i \tag{3.5}$$

where, L is the maximum phase value, P_i is the probability of each phase value in the phase image, which can be obtained from equation no (3.6).

$$P_i = \frac{f(i,j)}{n^2} \tag{3.6}$$

where $f(i,j)$ is the ith histogram count and n^2 is the number of pixels in the patch of an image.

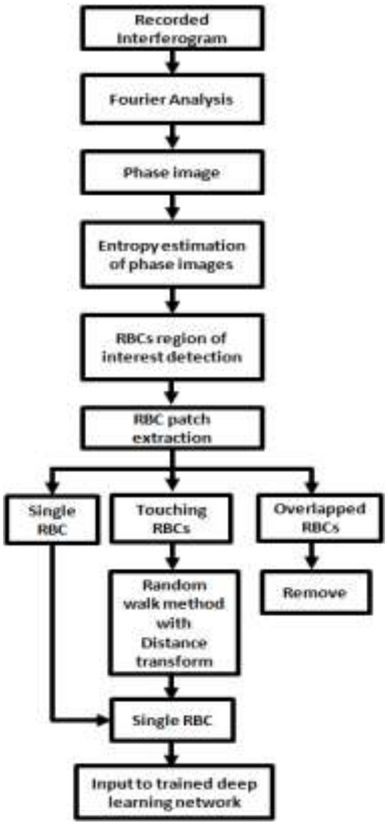

Figure 3.7 Flowchart of RBC patch extraction algorithm.

The entropy threshold is set to be 1.0 radian obtained by the number of trails and the higher entropy region is extracted i.e. RBC region. Now remove all those artifacts whose area is less than 60 x 60 pixels^2. The RBC patch is extracted with the help of the maximum and minimum pixel of coordination from the boundary pixels. There are number of patches which consist of touching and overlapping RBCs. Overlapping RBCs are excluded from the study and the RBCs which are touching are separated with the help of random walk method [163] in association with the distance transform [164] and the whole process is explained in figure 3.7.

3.3.2.2 Data Augmentation

DL is datasets hungry, and to get a labelled data is generally difficult in the medical field. Our dataset is relatively small (1000 images). However, in our case, we develop the QPI system using multi-wavelength red, green and blue, which will increase the sample size by 3 (RGB phase images). Therefore, with the help of our system, we increase the labelled dataset [96], [106]. To further increase the datasets, the images were rotate (45^0, and 135^0) but make sure that the numbers of samples for each class of RBCs must be same thereby balancing out the dataset.

3.3.2.3 Methodology

The whole description of the methodology to identify healthy vs infected and early vs late trophozoite malaria-infected stages is shown in figure 3.8.

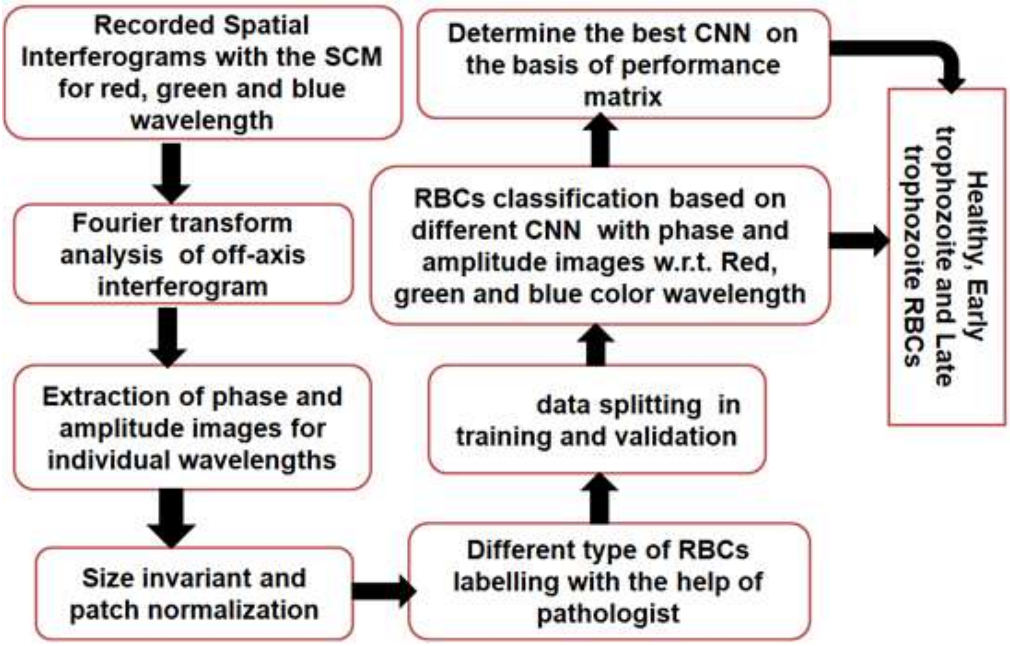

Figure 3.8 Overall workflow of our proposed training and learning methodology for the malaria infected RBCs CNN classification model.

Spatial interferograms were recorded w.r.t. each wavelength (red, green and blue). Once, the slightly off-axis spatial interferograms were recorded for each wavelength, the recorded interferogram was Fourier transformed. The first order peak was filtered out via spatially filter and then inverse Fourier transformation was performed to extract amplitude and phase information [17]. The same process has been repeated for each wavelength.

3.3.2.4 Models Description

In this study, we exploit the different layers architecture of CNN for the classification purpose such as AlexNet, VGG16, ResNet50, GoogLeNet, and custom - made network.

AlexNet: operates on input images of size 227x227x3. It has five convolution layers, three pooling layers, three fully connected layers and it also includes dropouts [100].

VGG-16: similar architecture as AlexNet but consist more convolution layers. It operates on input image of size 224 x224x3. It is composed of 13 convolution layers, 5 pooling layers, 3 fully connected layers and along with activation rectified linear unit (ReLU) and dropouts [97].

ResNet50: is a 50-layer Residual Network. This network introduces is residual learning, which tries to learn residual instead of learning some features. Residual are nothing but subtraction of learned feature from the input of that layer [104].

GoogLeNet: builds on input size 299x299x3. It includes four convolution layers along with batch normalization (BN) and activation ReLU, four pooling layers and nine inception layers which have convolution blocks followed by batch normalization and activation ReLU and also includes pooling. The inception module is an intrinsic component of GoogLeNet [90].

Customized CNN network: A number of CNN architectures are designed with a different number of convolutional layers, and each layer has different size (3x3, 5x5) and a different number of filters. Each convolutional layer is alternation with ReLu and pooling layers and a different number of filters. To minimize overfitting a dropout layer is added. The proposed CNN model and the optimization parameters are specified in table 3.5. The proposed model consists five convolution layers and two fully connected layers. To introduce non-linearity and to make fast convergence learning ReLU layer is added to all the convolution and fully connected layers. All the negative activation values become zero by ReLU layer. To reduce the spatial dimension max pooling layer is added to the second and fourth convolution layer after ReLU layer. Gaussian distribution with standard deviation 0.01 is used to initiate all the network weights for all the layers.

Table 3.5 Customized CNN architecture

Layer	Type	Input	Kernel	Filters	Stride	Pad	Activations	Output
Data	Input	120x120x3	N/A	N/A	N/A	N/A	N/A	120x120x3
Conv1	Convolution	120x120x3	3x3	64	1	1	ReLU	120x120x64
Conv2	Convolution	120x120x64	3x3	96	2	2	ReLU	61x61x96
Pool2	Max Pooling	61x61x96	2x2	-	2	0	-	30x30x96
Conv3[a]	Convolution	30x30x96	2x2	128	2	1	ReLU	16x16x128
Conv4	Convolution	16x16x128	3x3	256	1	1	ReLU	16x16x256
Pool4	Max Pooling	16x16x256	2x2	-	2	0	-	8x8x256
Conv5	Convolution	8x8x256	3x3	256	2	1	ReLU	5x5x256
fc6[b]	Fully Connected	5x5x256	9x9	1000	1	0	Tanh	1000x1
fc7[c]	Fully Connected	1000x1	1x1	1	1	0	Sigmoid	1

a. 20% dropout rate at the time of training
b. 50% dropout rate at the time of training
c. L2-regularization at the time of training

To improve the performance of the network, dropout layer with probability (0.2) is added after third convolution layer and probability (0.5) is added after first fully-connected layer. L2 regularization technique with a value of $\lambda = 10^{-3}$ is used for weight decay to avoid network from overfitting of the training data [165]. The learning rate is 0.0001 which after every 4 epochs decays by using inverse decay policy during training. Stochastic gradient descent (SGD) is used to optimize the loss function with a batch size of 32. To avoid any impact on learning all the dataset was randomly shuffled. To avoid loss function to trap into local minima and to move global minima, the momentum factor is set to 0.9. All the models were pre-trained on natural image dataset ImageNet and fine-tuned on our training dataset. The training and validation sets were randomly splitting.

3.3.3 Results and Discussion

In the present study, different transfer learning models were used to discriminate malaria-infected RBCs from the healthy RBCs and different stages of malaria (early vs late trophozoite).

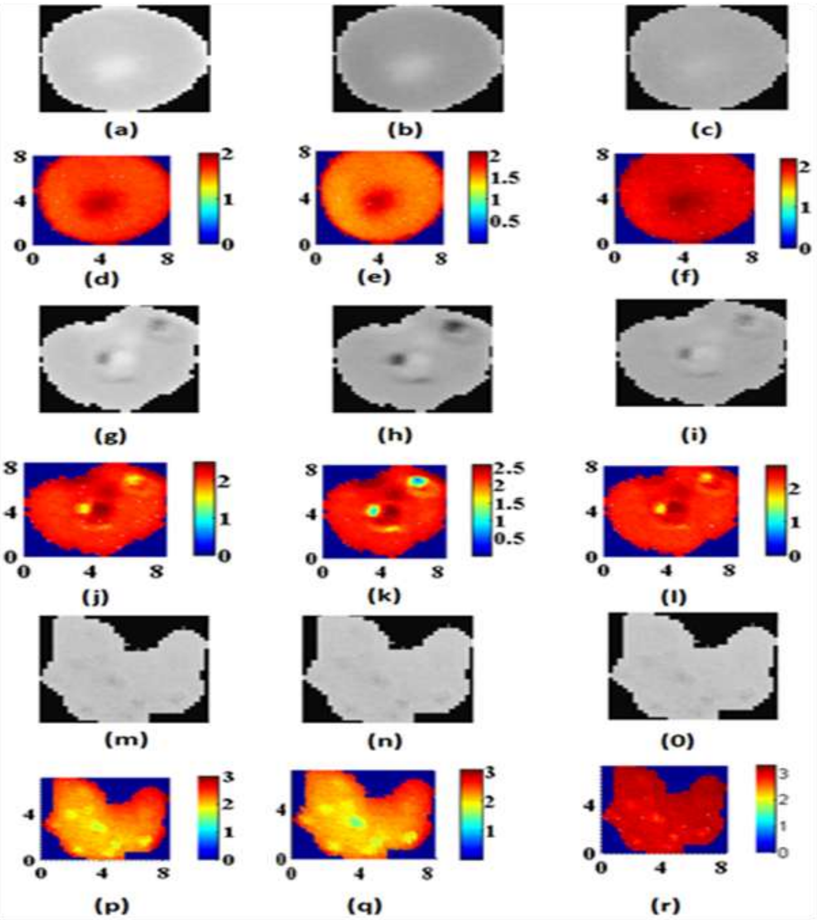

Figure 3.9 (a), (b), (c) and (d), (e), (f) are the amplitude and phase (radian) images of healthy RBCs for red, green and blue wavelength, respectively, (g), (h), (i) and (j), (k), (l) are the amplitude and phase (radian) images of early trophozoite RBCs for red, green and blue wavelength, respectively, and (m), (n), (o) and (p), (q), (r) are the amplitude and phase (radian) images of late trophozoite RBCs for red, green and blue wavelength, respectively.

To evaluate the performance of CNN used for the classification of healthy vs infected RBCs and early vs late trophozoite RBCs several experiments have been performed. Figure

3.9 shows the amplitude and phase images for healthy, early trophozoite and late trophozoite for red, green and blue wavelengths, respectively. In total 36 subjects (8 healthy, 15 early trophozoite and 13 late trophozoite) were used for analysis. The sample was split based on subjects into three non-overlapping subsets: to train the dataset 5 healthy, 10 early trophozoite and 7 late trophozoite subject was used, for validation 2 healthy, 3 early trophozoite and 4 late trophozoite subject was used and to test the dataset 1 healthy, 2 early trophozoite and 2 late trophozoite subject was used. For training and validation, 7 healthy, 13 early trophozoite and 11 late trophozoite subject datasets were used while for testing, 1 healthy, 2 early trophozoite and 2 late trophozoite subject datasets were used. The testing dataset is saved in a different folder and doesn't take a part in the training or validation of the network.

Further, to evaluate each network performance by feeding only phase information w. r. t. three wavelengths as a three-input channel. For each sample of the three wavelengths (red, green and blue), we have recorded 10 fields of view (FoV) at the different location of the same slide. The ground truth for the images was determined by a trained person who is expert in parasite identification. There are number of RBCs that even the trained pathologist was not able to find out the difference between early and late trophozoite from the bright field images. These phase images were removed from the training, but still used in testing. The total RBCs phase images extracted from training and validation dataset were – 3045 out of which 632 healthy RBCs, 602 early trophozoite RBCs and 611 late trophozoite RBCs, per subject for each wavelength were selected and analyzed. For dataset balancing, we chose 600 RBCs of each stage and the total number of RGB phase images RBCs images are 5400. To increase the robustness of the network data augmentation technique is also applied (45^0 and 135^0 rotation). Hence, the total number of sample size for training and validation is 16200. The testing is performed on 350 phase images extracted from healthy, early and late trophozoite RBCs. We cropped the small patch of size 60 x 60 pixels^2 phase images, which contains the single RBC. All RBC patch images were normalized to the same size 60 x 60 pixels^2. A different model has different receptive fields, therefore, we upsampled the size of cropped images according to the network requirement. All three wavelengths phase images were used at the input channel of the network. Therefore, the final size of the image at the network input is m x n x 3, where m and n are the number of input pixels to the different network. The input data sample was increased with the help of data augmentation technique. Data augmentation technique is used to improve the robustness of RBCs classification CNN model. In our experiment, all the TL models and custom model is trained using SGD with a momentum factor of 0.9 and the learning rate for the pre-trained network is 0.0001. All the models were trained for 50 epochs and the minibatch size for AlexNet and VGG16 is 64 whereas, for ResNet50, GoogLeNet and customized network the minibatch size is 32 due to memory constraints. All the models were trained and tested on a desktop computer running the Windows 10 operating system with Nvidia GTX 1070 Ti GPU, Intel (R) Xeon (R) CPU E5-1620, 3.60-GHz processor, 16 GB of RAM and 1 TB HDD.

Table 3.6 Performance metric for the identification of healthy and infected RBCs for testing datasets

Models	Sensitivity	Specificity	Accuracy	MCC
AlexNet	0.971	0.963	0.971	0.941
VGG16	0.981	0.966	0.973	0.947
ResNet50	**0.983**	**0.969**	**0.976**	**0.952**
GoogLeNet (Inception-V3)	0.981	0.967	0.974	0.949
Customized CNN	**0.979**	**0.965**	**0.972**	**0.945**

Table 3.7 Performance metric for the identification of early and late trophozoite RBCs for testing datasets

Models	Sensitivity	Specificity	Accuracy	MCC
AlexNet	0.901	0.903	0.901	0.803
VGG16	0.901	0.904	0.903	0.806
ResNet50	0.906	0.903	0.904	0.809
GoogLeNet	**0.907**	**0.917**	**0.912**	**0.824**
Customized CNN	**0.903**	**0.907**	**0.905**	**0.810**

A comparison study was conducted on healthy vs infected RBCs (early and late trophozoite RBCs) and early vs late trophozoite RBCs using different deep CNN's training model. Table 3.6 shows the performance metrics of all the models for the classification of healthy and infected (early and late trophozoite) RBCs, while table 3.7 shows performance metrics of all the models for the classification of early and late trophozoite RBCs for testing dataset in terms of accuracy, sensitivity, specificity and MCC. The significance of these performance metrics is already discussed in section 3.2.4.

Table 3.8 Computational test time of all the models

Network	Test time per image (ms)
AlexNet	38
VGG16	70
ResNet50	208
GoogleNet	348
Customized CNN	17

The results present that in table 3.6 and 3.7, shows that Customized CNN model has a comparable performance with the other transfer learning model with less number of layers. The customized network has a lower run-time which overall decreases the computational time and increases the throughput with respect to time as mentioned in table 3.8.

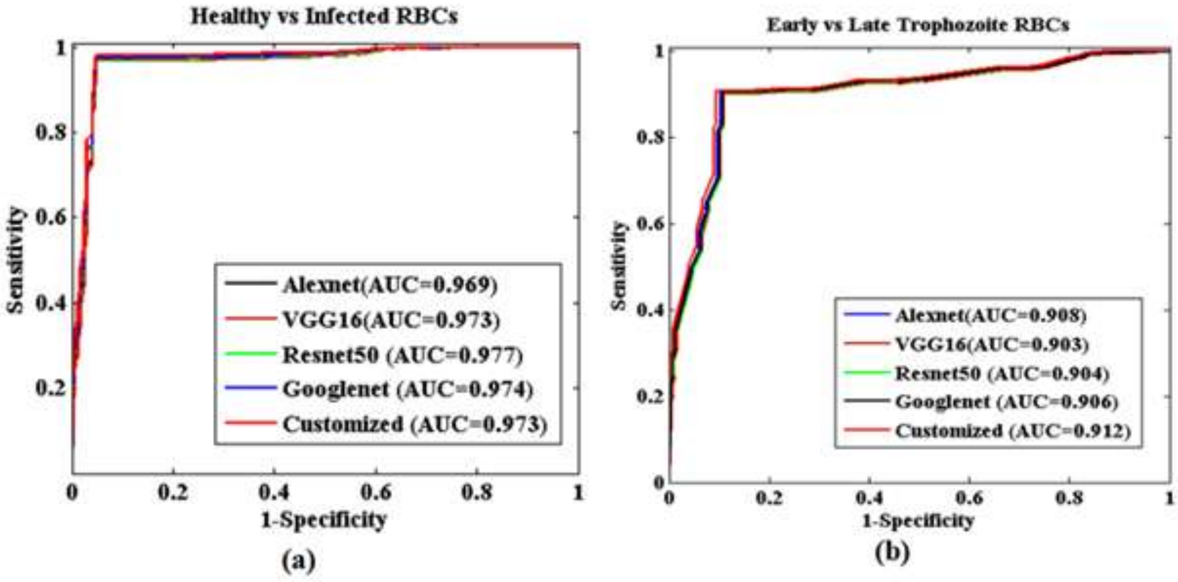

Figure 3.10 AROC for testing dataset of all the models (a) Healthy vs malaria infected RBCs and (b) Early vs late trophozoite malaria infected stages of RBCs.

Sensitivity and Specificity in the previous studies [125], [160] using QPI and machine learning is high in the case of healthy and malaria-infected RBCs (95% - 98%) however, in the case of malaria-infected stages (early and late trophozoite) achieved poor sensitivity i.e. 45.0% - 66.8% and 99.8% specificity [125]. In our study, we achieved 97.7% accuracy, 98.3% sensitivity and 96.9% specificity, respectively for healthy and malaria infected RBCs whereas in the case of malaria-infected stages between early and trophozoite 91.2% accuracy, 90.3% sensitivity and 90.7% specificity, respectively. The area under the ROC curve (AROC) for all the models is shown in figure 3.10. Figure 3.10(a) shows the AROC for all the models for healthy vs infected RBCs and figure 3.10(b) shows the AROC for all the models for early vs late trophozoite RBCs. The customized network performance with less number of layers is comparable to the other deeper networks.

3.1 CONCLUSIONS

In summary, FF-OSCM system was used to quantitatively characterize the healthy and malaria infected stages of RBCs. The extracted morphological features from the phase images were used to train the multi ensemble for an automated classification of RBCs with high accuracy, sensitivity and specificity. Both true predictions and false predictions are used to get accurate proposed model. The proposed model achieved 96.1% and 97.9% accuracy in detecting early trophozoite stage and late trophozoite stage. The present model was exclusively trained for morphological features based on phase images, in future biochemical and mechanical properties will also be exploiting to train the model to further increase the accuracy. The experimental setup being simple, compact and single-shot in nature and can be applied to any desired wavelength with high 3D resolution even in the case of highly scattering media.

Later on, we have designed an automated, high-throughput multi-wavelength SCM system based on low spatial coherence for *ex-vivo* imaging RBCs and DL algorithms applied for the classification of different stages of malaria RBCs. The purpose of multi-wavelength SCM with CNN promises of serving as an effective diagnostic system, where there is a limited labelled data sample. The results obtained in this section suggest that using CNN over conventional methods with limited labelled datasize for considerable improvement in specificity and sensitivity and also give an idea for working on focused area of images for malaria cells diagnosis. We strongly assume that this study can be dominant to significantly improve the screening accurate results for other health-related issues.

CHAPTER 4

BURN TISSUE CHARACTERIZATION USING OPTICAL COHERENCE TOMOGRAPHY

4.1 INTRODUCTION

Burns are the most common cause of accidental death. In the worldwide population, millions of people suffer from burn injuries and need a medical assessment every year [166]. Various causes that are involved to the skin burn tissues are electricity, hot fluids, radiations, chemicals etc. [167]. Burn tissue can be broadly classified into two categories -less severe burn (narrower) and more severe burn (deeper) as shown in figure 4.1 [168]. Less severe burns are also known as superficial or partial superficial burn, which can be healed by therapy itself, whereas, more severe burns require appropriate surgical excision to cure [169]. Presently, diagnostic and therapeutic decision making of burn injuries solely depends upon the experience of clinician or doctor. Even in the case of experienced doctor, the accuracy is only 60-80% [167]. The internal properties of skin change due to burn effect. Hence, the removal of non-viable tissue of burn victims is the primary goal of the clinician [170]. Under-debridement increases the risk of infection if inadequate amount of skin substitutes is placed on burn injuries and over-debridement reduce the skin's regenerative capacity and will increased postoperative scarring [171], [172]. Therefore, there is need of a technology for the accurate assessment of burn tissues without the expert clinician.

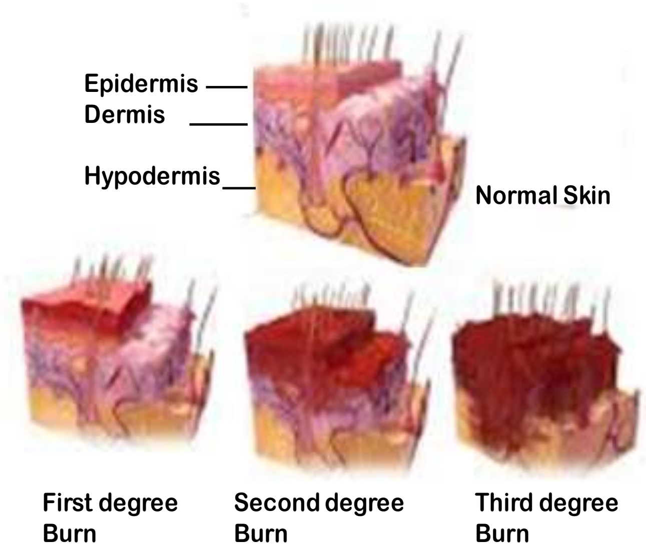

Figure 4.1 Normal and Burned Skin

A number of imaging modalities have been developed so far for the assessment of burn injuries such as color photography, indocyanine green imaging [173], near-infrared spectroscopy [174], laser Doppler imaging [175], laser speckle imaging [176], ultrasound [168], multispectral imaging [177], hyperspectral imaging [107] and photo-acoustic imaging [168]. One of the major disadvantages of the above technologies is either they have poor axial resolution or they operate in contact mode [178]. OCT is a non-contact, non-destructive, non-invasive, three-dimensional, cross-sectional imaging technique and has become a valuable tool for the detection of microstructural changes in the stromal collagen distribution, which effects the scattering and elastic properties of tissue [179]. Several studies have suggested that OCT can be used for the characterization or diagnosis of skin related disease e.g. skin cancer, sun damaged skin, actinic keratosis etc. [107], [179]–[182]. OCT has very high resolution, it is able to visualize sub-dermal features with associated skin related diseases [116], [170], [183], [184]. Previous applications of OCT to assess the burn severity have focused on the polarization sensitive OCT (PS-OCT) and spectroscopic OCT (SOCT) [180], [181]. PS-OCT detects the changes in collagen formation and not able to give the quantitative information whereas, SOCT burn assessment solely based on the measurement of tissue scattering spectra [185], [186].

In this study, normal and burn tissues are categorized by the texture classification and machine learning model is used for improving the accuracy [184], [187], [188]. In the last decades, the applications of CAD algorithms on OCT images are renowned [80], [122], [188]–[190]. It has the capability to determine the efficient results of pathological images and direct focus of the clinicians to the region of interest on OCT images. CAD algorithms are well established nowadays as various models have been developed in prior works linear discriminant analysis (LDA), logistic regression model or RF etc. [95], [154], [191]. Previous reports have achieved accuracy as high as 90% by applying different machine learning algorithms for the burn injury in an animal model [192]. Here, we seek to improve the discrimination of the tissues by using various features that are extracted from the computational (A-scan) and textural (B-scan) analysis. SS-OCT system is used for the quantitative assessment of burn injuries in the present chapter. Normal and burn tissues were categorized by extracting the morphological features from A-scan (back-scattered intensity profile) and B-scan (texture parameters) images. A generalized linear model was used as a classifier. The coefficient of the linear model was determined by training the model on training set data (34 samples) and the same set of coefficients was applied to calculate the response of testing data set (22 samples). The model quality was evaluated using convergence curve and AUC. In this study, A-scan and B-scan derived features from OCT images were used for in-vivo quantitative assessment of healthy and burn tissues.

4.2 EXPERIMENTAL STUDY OF MEMS VCSEL SWEPT SOURCE OCT SYSTEM

A fiber-based MEMS (Micro Electro-mechanical system) VCSEL (Vertical Cavity Surface Emitting Laser) (Model No. SL1310V1-10048, Thorlabs) SS-OCT system was utilized for studying the burn injuries of human skin. Figure 4.2 represents a schematic diagram of SS-OCT system consisting of a laser light source module, an imaging module and stand-alone probe. This framework utilizes a swept light source (central wavelength 1300 nm and wavelength-swept at 100 kHz) includes a MEMS-tunable VCSEL and a spectral bandwidth 10-dB i.e. 100 nm. The light stimulates from the laser source module splits 50:50 between the reference and sample arm of the SS-OCT system based on a Mach–Zehnder interferometer. A 5X objective lens (LSM03, Thorlabs), at a focal length of 25.1 mm in air, was utilized to collect the output light from the sample arm. 6.0 mW of average optical power was occurrence on the skin surface, which is far beneath the ANSI (Z136.1) at 1300 nm.

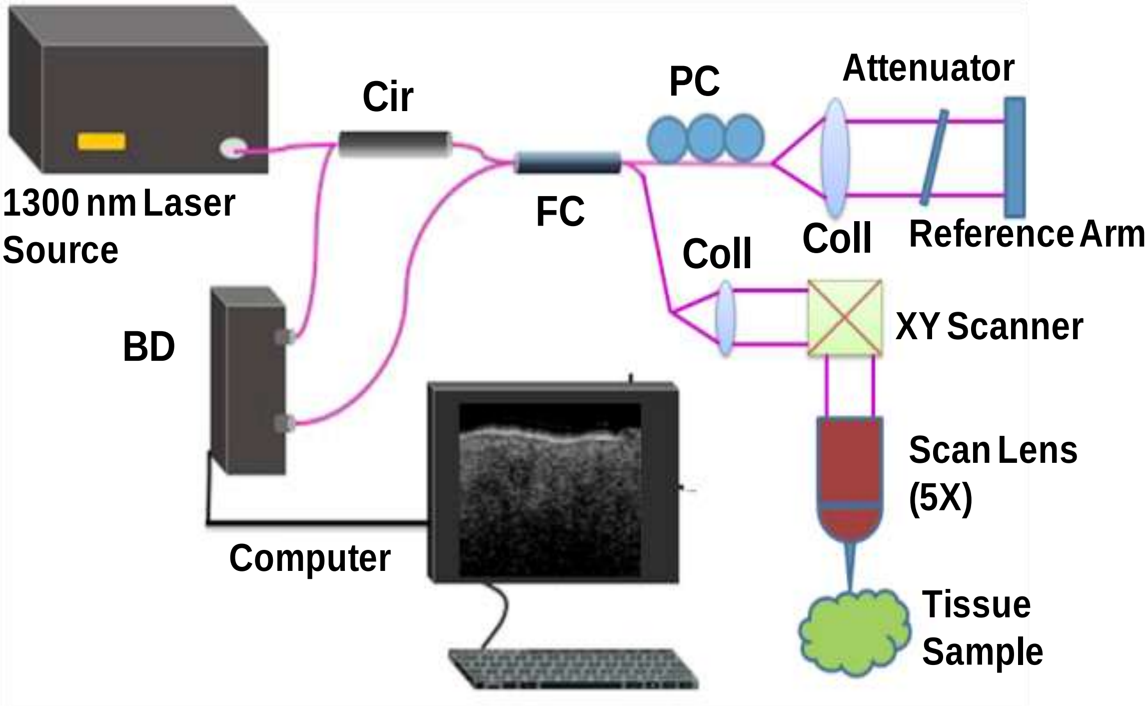

Figure 4.2 Schematic representation of MEMS VCSEL SS-OCT system; Cir: Circulator, PC: Polarization Controller, FC: Fiber Coupler, BD: Balanced Detector, Coll: Collimator.

The interferometric signal was obtained by a dual-balanced photodiode and sampled as a function of time utilizing 12 bits A/D converter at 500 MS/s. In air, 12 µm axial resolution and 22 µm lateral resolution was present. At the depth range from 0.5 mm to 4.5 mm, in air, sensitivity of the framework was ~107 dB. The key advantage of utilizing MEMS VCSEL SS-OCT system is its more SNR at a higher depth of penetration (~2.5 mm in tissue), fast acquisition rate (0.916 sec for 2 × 2 × 2.5 mm^3 scanning area), which is helpful in our proposed architecture for the differentiation of infected from the healthy tissue.

4.3 METHODOLOGY

4.3.1 Computational or A-scan analysis

Using OCT images, the computational analysis is based on obtaining an individual A-line (with dB unit in logrithmic scale). The change in the backscattered light or OCT intensity as a function of depth can be expressed by Beer-Lambert law [193],

$$I(z) = I_0 e^{-\mu z} \tag{4.1}$$

where, I_0 = incident light,

μ = attenuation coefficient of the light,

and z = depth of the light travelling in the sample.

Equation 4.1 represents the intensity decays induced by the sample, relatively large intensity occurs at the air-sample interface. These intensity decays are measured in dB unit. The attenuation property depends upon the optical scattering and absorptions of the tissue [194]. For the extraction of the slope parameter (first property), to deal with characterization of the sample, we fit linear line on each A-line as shown in figure 4.3 (b) and (e) for both normal and burned skin tissue, respectively. The linear line is subtracted from the A-line, the slope information from A-line is removed and the mean of the signal is approximately zero. As the mean of the signal is zero, we calculate the fluctuation in the intensity signal, which is a standard deviation as seen in figure 4.3(c) and (f) for both normal and burned skin tissue, respectively. Further, quality of the given sample can be found by evaluate the standard deviation as a second parameter. The whole process is also explained in figure 4.3 properly.

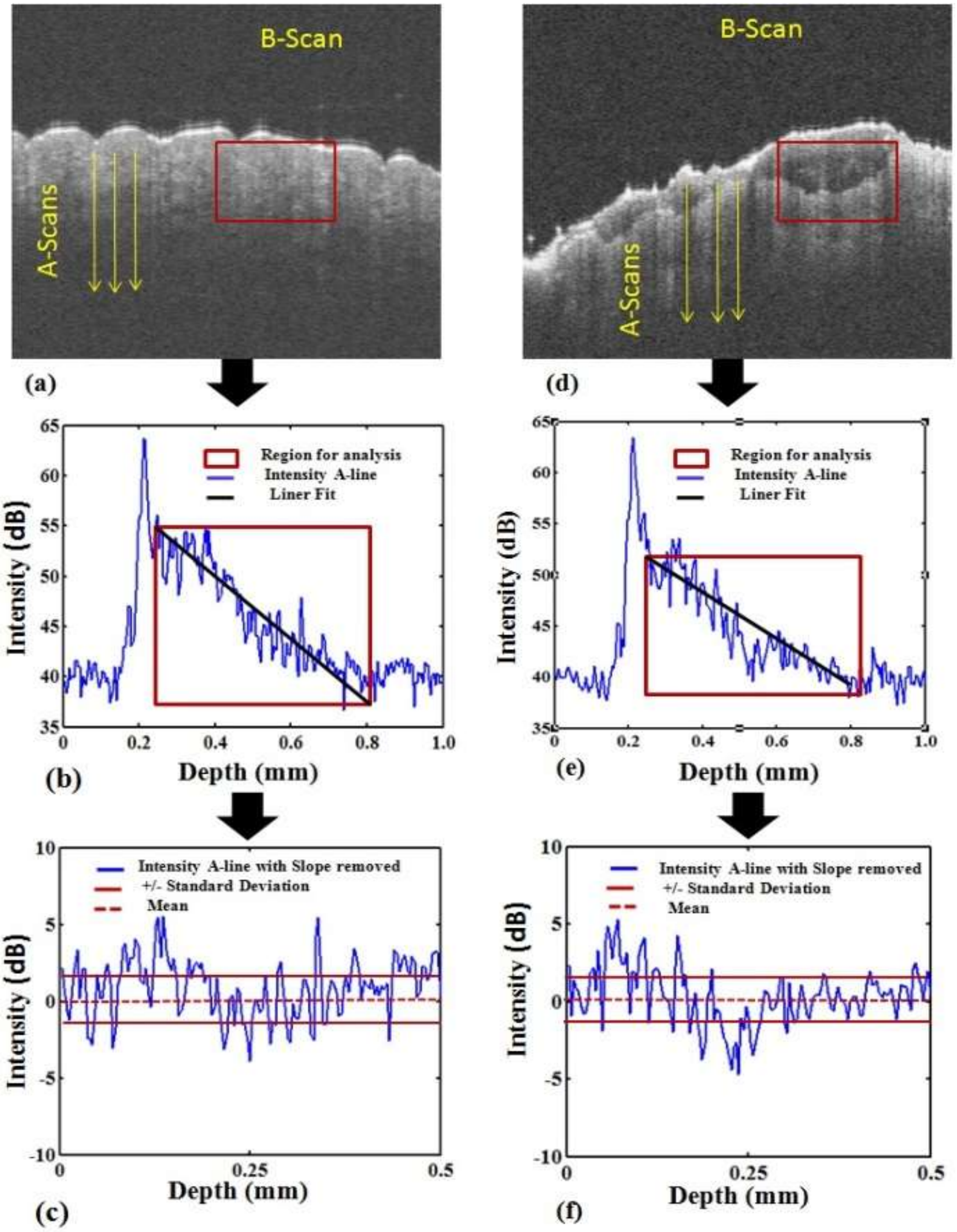

Figure 4.3 (a, d) OCT processed image, (b, e) A-line extracted from OCT image with the region of interest, and (c, f) after removed slope standard deviation of the signal for normal and healed burn tissue, respectively.

4.3.2 Texture or B-scan Analysis

Texture analysis in OCT images represents the spatial deviations in the form of intensity. A 2-D texture analysis is employed, which can be used to find the intensity distribution. As spatial distribution of the intensities changes, the texture of images changes accordingly. Gray-Level Co-Occurrence Matrix (GLCM) technique was presented by Haralick in 1970 on the basis of spatial distribution of the intensities [195]. The GLCM is found from the region of interest of the image at a particular pixel distance and direction by counting the number of gray level occurrences adjacent to another gray level. Gray levels represented by the Column and rows of the matrix and the probability of gray level co-occurrence represented by the elements of the matrix. We extracted the six most potential statistical features from the B-scan images such as mean, variance, entropy, skewness, speckle contrast, variance and kurtosis, from the normalized histogram of normal and burn tissues. These features are given in Equation (4.2) to Equation (4.7).

Mean: This feature corresponds to measure the average pixel intensity.

$$Mean\,(\mu)=\frac{1}{N\times M}\sum_{i=1}^{N}\sum_{j=1}^{M} x_i y_j \tag{4.2}$$

Variance: This feature is used to evaluate the heterogeneity in histogram distribution.

$$Variance(\sigma^2)=\frac{1}{N\times M}\sum_{i=1}^{N}\sum_{j=1}^{M} \left(f_{i,j}-\mu\right)^2 \tag{4.3}$$

Entropy: This feature is the measurement of randomness in an intensity distribution.

$$Entropy=-\sum_{i=1}^{N}\sum_{j=1}^{M} p(x_i,y_j)\log_2 p(x_i,y_j) \tag{4.4}$$

where, p is the probability of ith and jth pixel of each image.

Speckle Contrast: This feature is used to measure the quantified values of the mutual interference within the given sample.

$$Speckle\ Contrast=\frac{\sigma}{\mu} \tag{4.5}$$

Skewness: This feature corresponds to find the asymmetry of the histogram distribution.

$$Skewness = \frac{1}{N \times M} \sum_{i=1}^{N} \sum_{j=1}^{M} \left[\frac{f_{i,j} - \mu}{\sigma} \right]^3 \tag{4.6}$$

Kurtosis: This feature quantity is measuring the flatness of spatial intensity distribution.

$$Kurtosis = \frac{1}{N \times M} \sum_{i=1}^{N} \sum_{j=1}^{M} \left[\frac{f_{i,j} - \mu}{\sigma} \right]^4 - 3 \tag{4.7}$$

where, x_i and y_j are the i^{th} and j^{th} pixel level, $f_{i,j}$ is the i^{th} and j^{th} histogram count, σ is the standard deviation and $N \times M$ is the total no. of pixels.

4.4 MACHINE LEARNING CLASSIFIER

These six textural or B-scan features were combined with two A-scan features resulted in a total 8 features to describe each single image of every sample. These features were used as predictor variables, and response variable was the diagnostic result of burn and normal skin tissues. Least sum of squares method was utilized for identification. It is a mathematical formulation in which we have to minimize the error between the actual and predicted values as defined in Equation (4.8). Training was evaluated on 75% of the data chosen randomly.

$$Objfun = \left(\sum_{i=1}^{T} \sqrt{\left(X_i - \sum_{j=1}^{n} w_j * P_{ij} \right)^2} \right) \tag{4.8}$$

where, T is the total no. of observations in the dataset,

X is the target,

w is the weight corresponding to each feature,

n is the number of observations in a particular feature,

P is the no. of features.

4.5 RESULTS AND DISCUSSION

A total of 56 human skin tissue samples were imaged in vivo from 56 different people with the OCT system, consisting of 28 normal and 28 burned tissue sample. All the burn injury samples have more than two years post-burn. The region of area is automatically selected from the center of the image and window size is of 100 pixels. Each sample volume was taken 1600 x 960 x 500 pixels^3. To avoid the air-sample interface, the initial point was taken 10 pixels below the interface as illustrate in figure 4.3(a). An axial region of 1 mm was taken to process A-line for all the given samples. The depth-dependent reflectivity profile, A-line (dB unit in log scale) was obtained from the OCT images as shown in figure 4.3(b). As the depth of the sample increases, the amplitude of the OCT signal reflectivity decreases. To evaluate the attenuation coefficient, for each sample, we averaged 200 B-scan images and 100 adjacent A-lines from the centre of the B-scan image, which corresponds to 464 µm in the lateral distance. Slope parameter was obtained by fitting the linear line on each A-line and subtracting the linear fit line from the A-line, change in intensity signal or standard deviation was calculated. The whole process is explained in figure 4.3 (a-c). Similar analysis as shown in figure 4.3 (a-c or d-f) has been performed for all the 56 samples (normal and burn). The attenuation coefficient for normal and burn skin is $0.018 \pm 0.01 dB/\mu m$ and $0.014 \pm 0.01 dB/\mu m$, respectively as presented in table 4.1. The greater absolute value of slope for normal as compared to burn tissue is an indication of more light attenuated for the same penetration depth. The standard deviation for normal and burn skin is $2.8 \pm 0.2\, dB$ and $2.4 \pm 0.2\, dB$, respectively as shown in table 4.1.

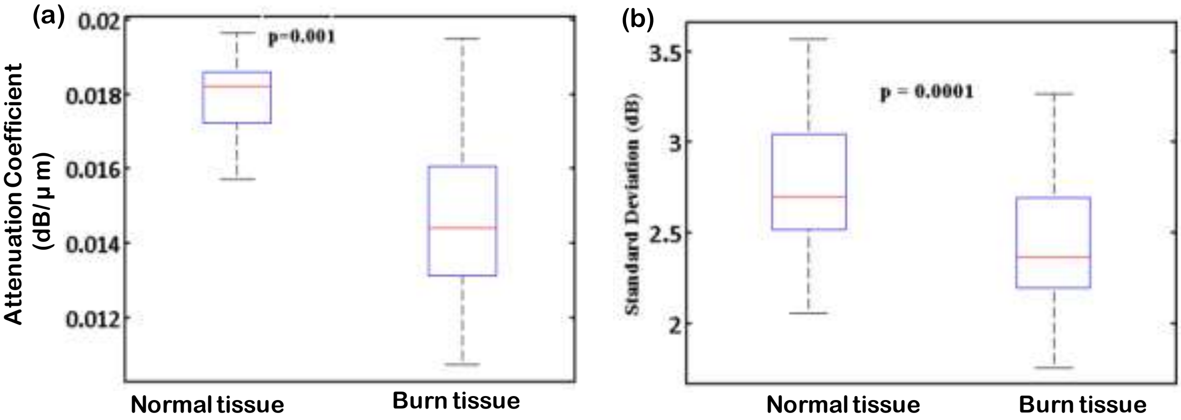

Figure 4.4 Box plots of A-line quantified parameters with significant p-values (a) Attenuation Coefficient in dB/µm (b) Standard Deviation in dB for normal and burn tissues, respectively.

The changes in intensity signal or standard deviation is higher for normal as compared to burn tissue is an indication of more variation of birefringence along the depth as seen in figure 4.4. Within the B-mode images of 1600 x 960 pixels (height x width), a region of interest (ROI) of 500 x 150 pixels sub-image was chosen corresponding to a physical area of ~210 x 63 µm^2. Six features were obtained from the normalized histogram of 56 samples (28 normal and 28 burned). In each sample we consider 200 B-scan images and 100 A-scan images on every B-scan image.

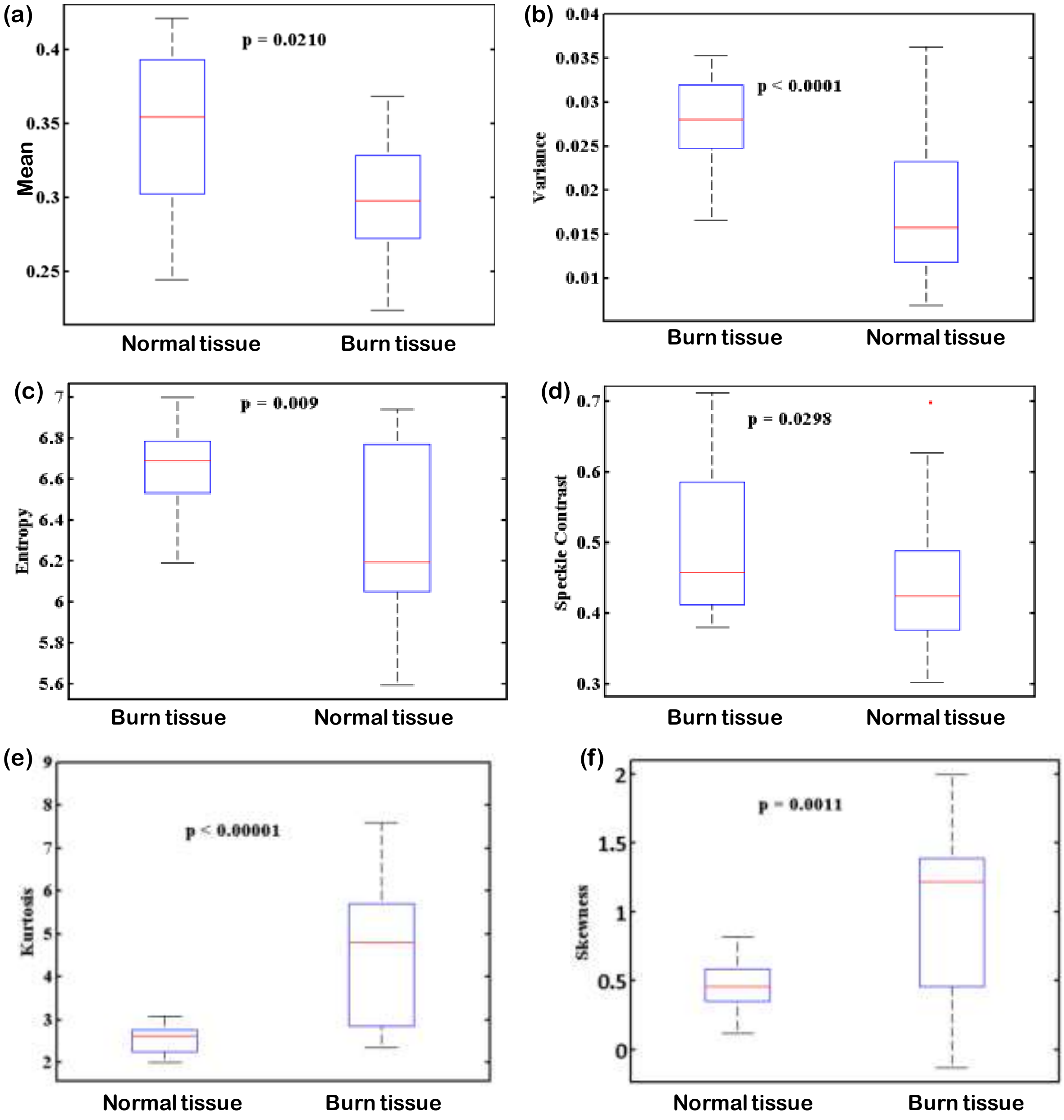

Figure 4.5 Box plot of B-line quantified features with significant p-values (a) Mean (b) Variance (c) Entropy (d) Speckle Contrast (e) Kurtosis and (f) Skewness for the normal and burn tissues, respectively.

So, therefore, a total 56 x 200 x 100 data points are used for classification out of which 34 x 200 x 100 data points are used training while 22 x 200 x 100 data points are used for testing. Table 4.1 shows the corresponding values of the normalized features of A-scan and B-scan. It can be seen from the figure 4.5 (a) that the burn tissue group has lower mean intensity value as compared to the normal tissue, which may be due to aggravated necrosis and reduced collagen concentration. The box plots are shown in figure 4.5 (b)-(f) that entropy, speckle contrast, variance, skewness and kurtosis of burn tissue is higher as compare to the normal it may be because burn tissues have thicker collagen so burn tissue becomes more heterogeneous. It can be also observed from figure 4.2(a) and 4.2(d) that the normal tissue is smoother and homogeneous, while the burned tissue has fragmented, degenerated, and heterogeneous poorly structured architecture.

Table 4.1 A-scan and B-scan features of burn and normal tissues with significant p-values

Features	**Burn skin**	**Normal skin**	**P value**
Attenuation coefficient(dB/µm)	0.014±0.01	0.018±0.01	0.001
Standard deviation (dB)	2.4±0.2	2.8±0.2	0.0001
Mean	0.31±0.2	0.35±0.2	0.0210
Variance	0.028±0.01	0.015±0.01	<0.0001
Entropy	6.7±0.1	6.1±0.1	0.009
Speckle Contrast	0.46±0.05	0.43±0.05	0.04
Skewness	1.3±0.05	0.45±0.05	0.0011
Kurtosis	4.8±0.1	2.8±0.1	<0.00001

Least sum of squares method-based classifier was utilized for the automated classification between the normal and burn tissue based on the feature vectors associated with the A-scan and B-scan OCT images. The convergence curve in figure 4.6 illustrates a typical characteristic of least sum of squares model.

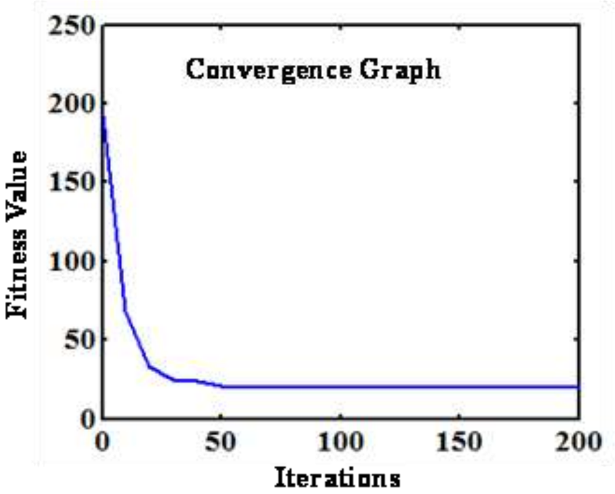

Figure 4.6 Convergence graph between iterations and fitness value.

It shows a rapid convergence at the first 25 iterations, followed by progressive improvements as it approaches the optimal solution in next 30 iterations. After performing 200 iterations on the training dataset, we have found best curve weights, as given in table 4.2.

Table 4.2 Weight values corresponding to their features

Target	Features							
Class (Burn/ Normal)	Attenuation Coefficient	Standard Deviation	Mean	Variance	Entropy	Speckle Contrast	Skewness	Kurtosis
	9.6	0.05	-1.51	7.36	0.2	0.10	0.34	-0.32

Figure 4.7 represents the AUC curve for the testing dataset. Sensitivity and specificity of 91.6% and 90% were calculated respectively, with average AUC at 95% confidence interval being 0.91, yielding an overall accuracy of 91%. With the help of this model, we can automatically classify the normal and burn tissues even without a specialized facility and clinician. We also performed the logistic regression algorithm for classification but in our case, we achieved higher accuracy for linear regression as compare to logistic regression.

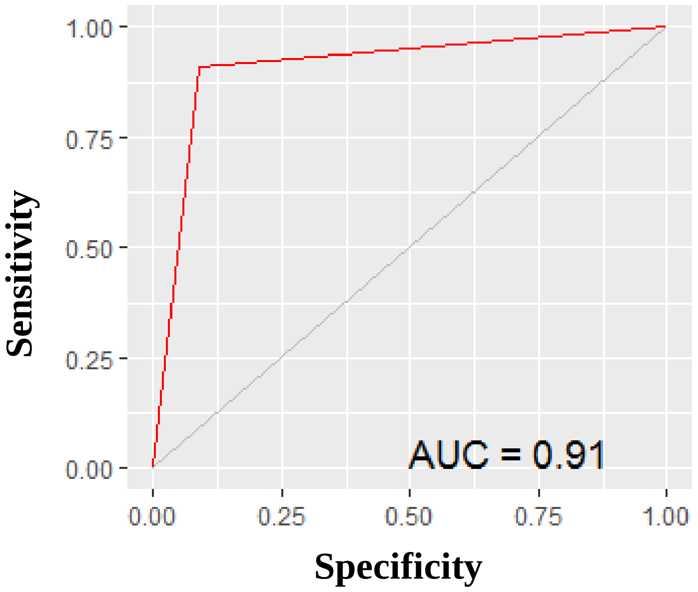

Figure 4.7 AUC graph for the testing dataset.

This technique prompts a quick and accurately quality assessment of burn tissues. The main drawback of the present system is its limited depth of penetration, which is a few hundred microns in the skin and the limited number of samples.

4.6 CONCLUSIONS

In summary, this chapter describes the human skin tissue samples were imaged *in vivo* using the OCT system. Two A-scan and six B-scan quantitative features were extracted from the normal and burned tissue images. Least sum of squares method-based learning model was used for classification with 91% accuracy. The result indicates that integration quantitative features from both A-scan and B-scan OCT images can be powerful *in vivo* diagnostic tool for quantitative analysis of burned tissues without a specialized facility and clinician. It will also assist burn surgeons in preparation and execution of burn surgery. Future work will be emphasized on differentiating between various grades of burn injuries and also studying the freshly burn injuries.

CHAPTER 5

AUTOMATED BREAST CANCER MARGIN ASSESSMENT USING OPTICAL COHERENCE TOMOGRAPHY IMAGES

5.1 INTRODUCTION

Breast cancer is the leading cause of woman's death in the worldwide, especially in the underdeveloped countries [196]. Cancer is commonly found when it has progressed to the later stages [197]. A cancer is usually formed by the accumulation of somatic mutations, which are further regulated by epigenetic changes that converts normal cells into malignant form [198]. According to the International Agency for Research on Cancer of the WHO 2012 statistics, 8.5 million women died from breast cancer. The number of cases will significantly increase to more than 27 million by the end of 2030 [199]. Many risk factors for developing the breast cancer include age, woman’s personal history, hormonal therapy, race, dense breast and radiation exposure [95], [200]. Biopsy has normally used the method of medical testing for the cancer detection in which the tissue samples stained with hematoxylin and eosin (H & E) are removed from a patient and then examined by a trained pathologist using bright field microscope to determine the occurrence or extent of a disease [201], [202]. The histopathologist determines cancerous regions or degree of cancer by visually determines the cell regularities and tissue distribution. Sometime the pathologist has a different diagnosis opinion of the same tissue, especially in the case of a non-experienced which delays the right diagnosis. Thus, the detection of cancer by the histopathologist is very subjective in nature [119], [121]. Recently, various computer-aided diagnosis techniques are developed for the classification of cancerous breast tissues based on histology images to assist the physicians and histopathologist who are less experienced [77], [95], [105], [161], [201], [203]. The inherent drawback of a computer aided system based on histological images is the lack of in-vivo observation in real time and sampling errors due to a limited number of samples representing larger areas of tissue. To overcome these issues an alternative imaging technique is needed which will perform the real-time, non-invasive, and rapid screening.

OCT is a non-contact, non-invasive, high-resolution (approaching the histopathology level), three-dimensional imaging technique [202], [203]. The penetration depth of 1-2 mm makes it more suitable for the surgeons to rapidly visualize the tissue morphology beneath the surface over the larger surface area in a non-invasive manner [183], [204]. In the recent past, a few pilot study has been investigated for breast cancer detection using OCT which incorporates human tissue imaging, [113], [204]–[206] animal preclinical studies, and intraoperative studying [207], [208]. Full-field OCT and Full-field optical coherence elastography have been also utilized for breast cancer margin assessment [77], [113], [207], [209]. Machine learning model has been established for the automatic quantification of breast tissues using OCT systems [210]–[212]. The previous studies for the assessment of breast cancer margin involve various features extracted from either OCT A-line features or features extracted from OCT B-scan images (texture analysis, fractal analysis) [113], [204]–[206]. The maximum specificity to detect cancer-positive margins obtained for OCT images acquired is less than 90% [113], [204], [206]. The main drawback of manually derived features that an important feature could be omitted by the human designers. Even an expert derived feature could not contain the entire feature space that describes the pathology. To overcome this challenge deep learning will be a good solution. The biggest advantage of deep learning, it does not need a manual or handcraft extraction of features. Deep learning itself learns to extract features while training. Recent studies show deep learning methods are rapidly growing for imaging classification [88], [161], [213], [214]. Modernized deep learning networks have played significant performance in automatic image recognition in different streams such as medical imaging analysis etc.[88], [100], [215]–[217]. Deep belief networks (DBNs), deep neural networks (DNNs) and CNNs are the main types of deep learning, CNNs are very helpful when the information is stored in the spatial location, especially in imaging based applications [92], [218]–[220]. The major problem with DNN or CNNs is its data hungry and in the field of medical imaging, there is limited labelled data. An alternative to this training a CNN from scratch, a fine-tuned network which is already pre-trained on a large labelled dataset of different applications. There are various CNNs which are pre-trained on millions of images from ImageNet that can be fine-tuned on our dataset using transfer learning [86], [92], [99]. Transfer learning model transfers the knowledge in the low layers of a base CNN which trained from a large database of ImageNet to our specific task. These networks are AlexNet, GoogLeNet, ResNet, and inception, etc. [76], [99], [100], [214], [217]. It will be important to explore the integration of pre-trained CNN with imaging systems to improve detection of disease. Inception-v3 is the present state of the art so it becomes an obvious choice for the classification. In the present study, we apply a fine-tuned pre-trained CNN Inception-v3 model with reverse active learning to classify healthy and malignant breast tissues using MEMS-VCSEL SS-OCT images. The detail of the SS-OCT system was discussed in the previous chapter in section 4.2. The sensitivity, specificity, and accuracy achieved from the network is 90.2%, 91.7%, and 90%, respectively for the testing datasets, which significantly outperforms the previous work [113], [204]–[207]. Further, the trained network is utilized for assessment of breast cancer margin to predict the tumor with negative margins. The algorithm will be used for real-time, rapid, in-vivo, intra-operative margin assessment over large surface areas while preserving tissue structure.

5.2 METHODOLOGY

5.2.1 Pre-Processing

To differentiate between healthy and malignant tissues, B-scan (x-z) images were recorded with SS-OCT system. In general, the tissue surface has a curvature and during the training of the network the image patches belongs to the surface may contain some background or DC component which may affect the network performance. To avoid the effect of background on the network we first flattened the images before cutting the patches from the whole image. The flattening process is explained in the figure 5.1. From the highest identified layer, the bottom layer was chosen at a depth of 250 pixels (~1.2 mm).

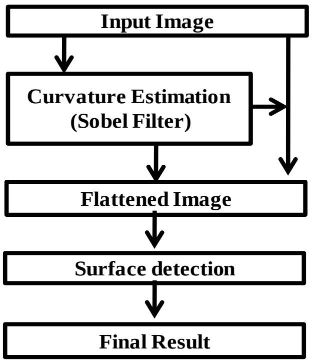

Figure 5.1 Flow chart of flattening the surface of image

250 pixels were picked heuristically to significantly avoid pixels with low SNR as appeared in figure 5.2. Rest of the pixels of the images were removed. All the processed images were of size 735 x 250 x 1 pixels. To normalize the intensity a mean value of intensity is subtracted from the individual processed OCT images.

5.2.2 Hardware

The processing of the data was performed using a Windows 10 system with Intel (R) Xeon (R) CPU E5-1620 0 3.60-GHz processor, 1 TB HDD, 64 GB RAM, a CUDA-enabled Nvidia quadro P4k GPU with 8 GB VRAM graphical processing unit (GPU), Matlab R2018a, and CUDA 9.0 dependencies for GPU acceleration.

5.2.3 Inception-v3 Architecture

CNN architecture which is normally used in image processing applications builds on four main operations: convolution with trained filters and weights, activation rectified linear unit (ReLU), pooling and classification.

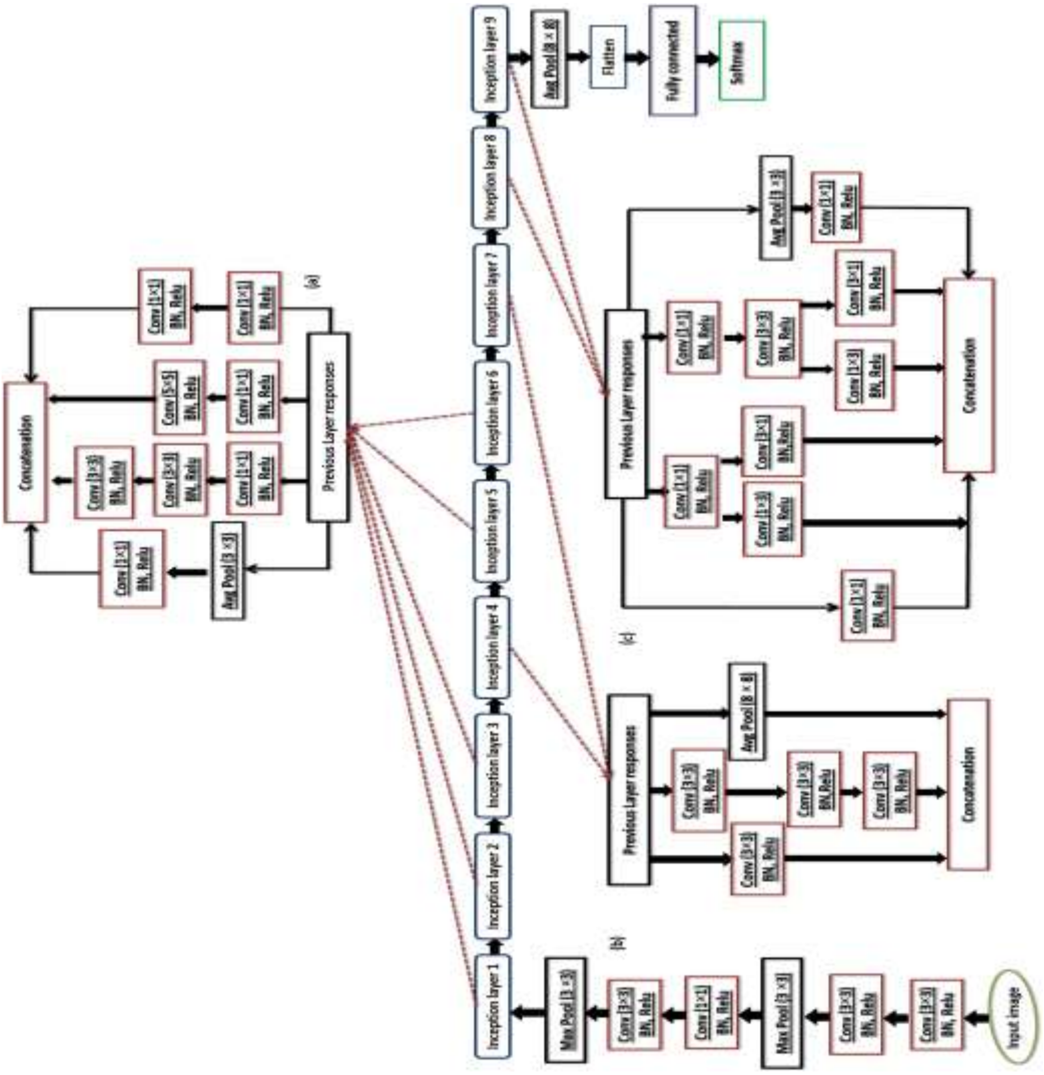

Figure 5.2 Inception-v3 architecture with separately inception layer (a) consists inception layer 1,2,3,5 and 6 (b) includes inception layer 4 and 7, and (c) includes inception layer 8 and 9, respectively.

Given an image or the responses, the convolution layer convolves with a set of filters (learnable), the activation layer alters negative values by zero, the batch normalization (BN) acts as a boost operation, the pooling layer replaces each element based on a algebraic function (maximum or mean) of neighboring elements to reduce the image size and the fully connected layer is a conventional artificial neural network (ANN). The network learns the features automatically through convolutional layers which consist of filters whose weights are learned during the training. The early level is identifying the local features while the higher level is responsible for global features.

5.2.4 Description of Inception Layers

The inception layers process the given information in the independent streams of information processing and concatenate along the depth at the output as shown in figure 5.2 (a, b and c). The detail of each layer of the architecture is given in Table 5.1. In figure 5.2(a), four independent streams are used for inception layer 1, 2, 3, 5 and 6 but in the last stream of the module include average pooling follow by the convolution block for data compression. Similarly, in figure 5.2(b), the inception layer 4 and 7 consists three independent streams of information processing and concatenates along the depth at the output. The third stream includes average pooling block, the size being 3×3 as seen in figure 5.2(b).

Table 5.1 Inception-v3 with inception layers architecture

Layer	Input size	Patch size/stride	Output size
Convolution	299×299×3	3×3/2	149×149×32
Convolution	149×149×32	3×3/1	147×147×32
Convolution	147×147×32	3×3/1	147×147×64
Max Pool	147×147×64	3×3/2	73×73×64
Convolution	73×73×64	1×1/1	73×73×80
Convolution	73×73×80	3×3/1	71×71×192
Max Pool	71×71×192	3×3/2	35×35×192

Inception 1	35×35×192	-	35×35×256
Inception 2	35×35×256	-	35×35×288
Inception 3	35×35×288	-	35×35×288
Inception 4	35×35×288	-	17×17×768
Inception 5	17×17×768	-	17×17×768
Inception 6	17×17×768	-	17×17×768
Inception 7	17×17×768	-	8×8×1280
Inception 8	8×8×1280	-	8×8×2048
Inception 9	8×8×2048	-	8×8×2048
Avg Pool	8×8×2048	8×8/1	1×1×2048
Flatten	1×1×2048	-	1×1×2048
Fully connected layer	1×1×2048	-	1×1×2048
Softmax Classifier	1×1×2048	-	1×1

Figure 5.2 (c) performs the information for inception layer 8 and 9, it has four independent streams of information processing and concatenates along the depth at the output. At the end of the overall network as given in figure 5.2, all the features map is flattened in a huge one-dimensional vector and softmax function is used to classify healthy tissue and the malignant breast tissue.

5.2.5 Modifications to Inception-v3 pre-trained on ImageNet

1) Removal of last three layers: predictions, predictions_softmax and ClassificationLayer_predictions.
2) Addition of three layers: Fully_connected_Layer, softmax_Layer and Classification_Layer
3) Fully connected layer: have only two outputs.
4) To learn the feature space shifts between ImageNet data and OCT data, weights are randomly initialized of all fully connected layers and convolutional layers in auxiliary branches.
5) To avoid expertly introduced learning rates at different epochs as in the case of stochastic gradient descent (SGD), adaptive gradient algorithm (ADAGRAD) results in impulsive step lengths [221].

Note: All the naming of the layers is corresponding to Neural Network toolbox, Matlab R 2018a.

5.3 RESULTS AND DISCUSSION

An experiment was performed on 48 subjects of age between 35-60 years including healthy and malignant breast tissue. To perform this study, the samples were collected from All India Institute of Medical Science (AIIMS) New Delhi. Ethical clearance was accepted by Ethics committee of IIT Delhi and AIIMS. After imaging the tissue, for 24 hrs it’s placed in 10% Formalin and then for the histology process, it is transferred to 70% ethanol. From every specimen, several 2 μm-thick slices were taken out in the OCT B-scan direction with a gap of 6 μm between levels and each slide stained with hematoxylin-eosin (H&E). These slides were images with the help of 50x. During OCT reconstruction algorithm for every B-scan image, 8 B-scan images were average out.

5.3.1 Dataset

An *ex vivo* study was performed using MEMS-VCSEL based SS-OCT system on 48 subjects (22 healthy and 26 malignant excised tissue). The sample was split based on subjects into three non-overlapping subsets: to train the dataset 70% subject was used, for validation 20% subject was used and to test the dataset 10% subject was used. For training and validation, 20 healthy and 23 malignant excised tissue subject datasets were used while for testing, 2 healthy and 3 malignant excised tissue subject datasets were used. The testing dataset is saved in a different folder. There is an equal distribution for both the classes in between splits. To significantly improve the performance of the network an automated reverse active learning training strategy is used to classify the breast tissues. The size of the final processed image is 735x250 pixels^2. Each image has been sub-divided into small patches to train the network. A window or patch of size 150x150 pixels^2 is selected and slide over the entire image. Every time the window contains the 2/3 overlapping pixels. The total size of the sample is 1460. This will generate 21,900 image patches for each class.

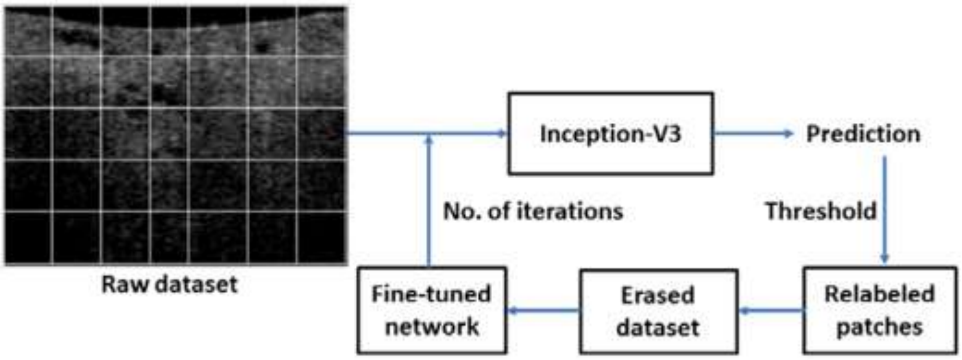

Figure 5.3 Reverse active learning.

To overcome the challenges of overcoming fitting and to increase the cardinality of the training data (both the classes) data augmentation techniques have been applied. Each test sample first duplicated with augmentation transformations, and then classified with an averaged prediction. The augmented datasets consist of the original, rotated and horizontally flipped patches.

- Horizontal flipping: The dataset images were horizontal flip to increase the cardinality of the training datasets.
- Rotation: The dataset images rotated by an angle of 90^0, 180^0, and 270^0 to increase the size of the training datasets.

All the samples images were pre-processed as previously mentioned. To increase the sample size data augmentation (horizontal flipping and rotation) technique was used which resulted in 2,19,000 training images. Each patch is labelled to the corresponding image. However, there might be some images where the whole image doesn’t suffer from cancer and there are some patches which might be normal, but they are mislabelled as cancerous and vice-versa. To detect those mislabelled patches and removed them from the training dataset a reverse active learning training strategy is used, which is shown in figure 5.3. Each patch of an image is upsampled to 229 x 229 x 1 and was concatenated thrice to make the size of each patch to the required network input. Therefore, the final size of each patch image is 229 x 229 x 3. We evaluated the effectiveness of the model on both original and augmented datasets in terms of accuracy, sensitivity, and specificity. For the training/validation split 90% of the subject dataset is used. 77% of this dataset is used for training and 23% is used for validation from both healthy and malignant subject. A momentum optimizer with momentum 0.9 and a batch size of 32 is used to minimize the loss. The network weights are initialized with the pre-trained weights of the inception v3 model on ImageNet [221]. The initial learning rate is 0.0001 and decreases exponentially every 500 mini-batch iterations with a decay factor of 0.9. The weights are regularized with weight decay with L2 penalty multiplier of 0.003. A 0.5 dropout ratio is applied to the first two fully-connected layers.

Table 5.2 The numbers of training dataset without augmentation in each iteration

No of iterations	Training dataset
1	30353
2	28347
3	27338
4	26784
5	26112

Table 5.3 Patch-based average classification accuracy for number of iterations without augmented datasets

Iteration number (K)	Training dataset (%)	Validation dataset (%)	Sensitivity (%) for validation dataset	Specificity (%) for validation dataset
K=0	92.17	83.27	81.33	85.21
K=1	92.73	89.84	86.57	93.11
K=2	92.91	91.84	88.91	94.77
K=3	93.11	92.11	89.74	94.48
K=4	93.60	92.41	89.93	94.89

The network is initially trained on the original dataset i.e., without augmentation and once its performance reached to a satisfactory level. Now the trained network is used for the prediction of the original training dataset and those patches which have confidence lower than 0.5 were removed. The network was retrained till its performance reaches to satisfactory level. After each iteration, the number patch images were listed in Table 5.2. The reverse active learning fine-tuned the network and improves the performance significantly. It can be observed that from the Table 5.3 that the proposed patch-based classification with reverse active learning training the obtained average accuracy on training and validation set are 92.90 % to 89.89 %. The testing accuracy is 86.09 %. Furthermore, we notice that after 3 times of iteratively refinement, the mislabelled patches in the original training set were basically removed and the accuracy stopped increasing.

Table 5.4 The numbers of training set in each iteration with augmented dataset

No of iterations	Training dataset
1	151767
2	140764
3	135687
4	132670
5	131769

Table 5.5 Patch-based average classification accuracy for number of iterations with augmented dataset

Iteration number (K)	Training dataset (%)	Validation dataset (%)	Sensitivity (%) for validation dataset	Specificity (%) for validation dataset
K=0	96.57	89.97	87.71	95.23
K=1	97.93	93.93	91.63	96.23
K=2	97.99	94.04	92.09	95.99
K=3	98.77	95.09	93.57	96.61
K=4	98.02	95.61	93.74	97.48

Now, the network is trained on augmented datasets and those patches which have confidence lower than 0.5 were removed. Furthermore, data augmentation each patch was augmented to four patches. If two augment patches were detected as mislabelled and removed, the remaining two patches were also removed from the training dataset. The network was retrained till its performance reaches a satisfactory level. After each iteration, the number patch images were listed in Table 5.4. It can be observed from Table 5.5, that the proposed patch-based classification with reverse active learning training the obtained average accuracy on the training and validation set is 97.85% to 92.09 %. The testing accuracy is 90.12 %. Figure 5.4 represents the ROC for the testing dataset.

We also include the shearing augmentation and different angle rotation, but it badly affects the performance of the network. The increase in the number of epochs doesn't increase the performance of the network only the time consumption increases. Augmentation techniques help in increasing the accuracy, sensitivity and specificity. The data augmentation generating virtual images using flipping and rotation at different angle position helps to increase the robustness of the network.

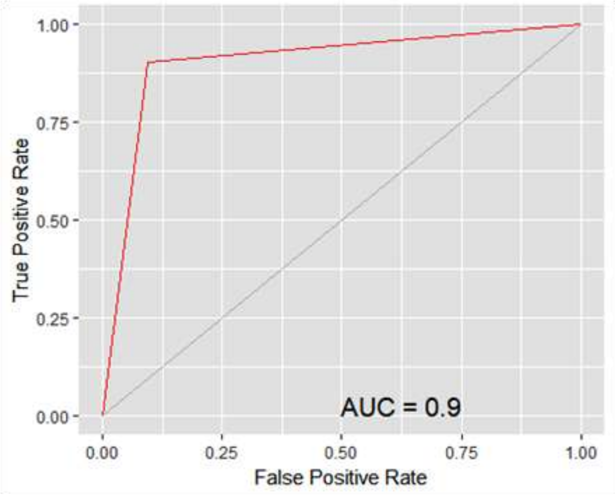

Figure 5.4 ROC for augmented testing dataset

There are some misclassified images as shown in figure 5.5, which is classified as normal in place of cancer tissue. The possible reason for that it might be some of the tissue which has mix response, cancers as well as normal tissue but the area of cancer is very small and could be classified as normal one. It's also possible that some of the subjects may be falsely included. These reasons affect the performance of the network.

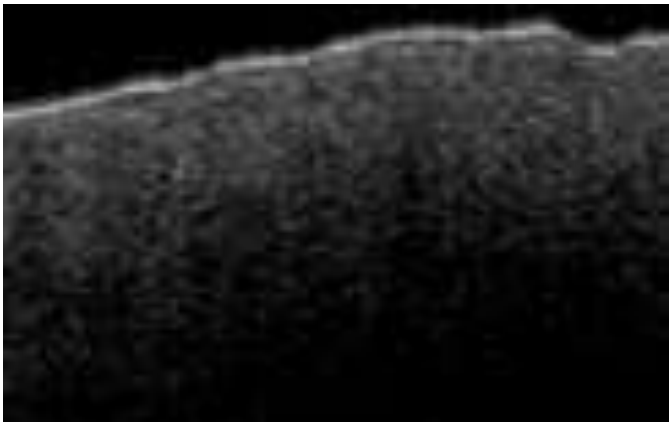

Figure 5.5 B-scan OCT image of cancerous tissue

5.3.2 Cancer Margin Assessment

For cancer margins assessment, we choose B-scan images which have both healthy and malignant tissues. The Image is pre-processed and flattened.

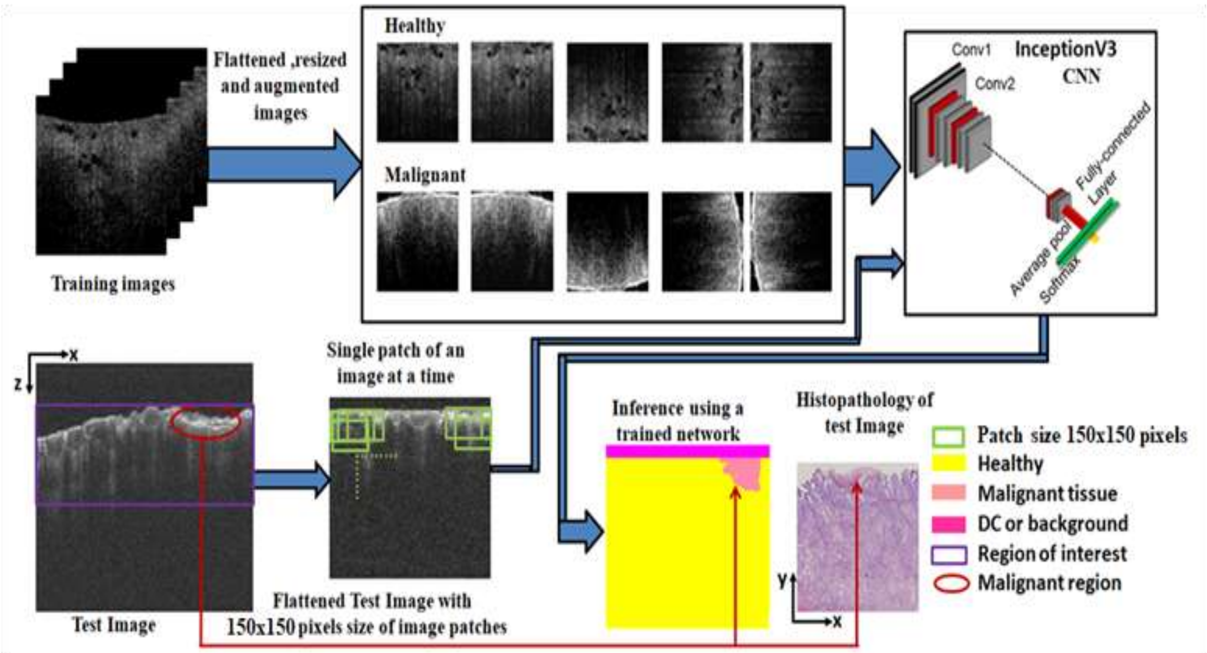

Figure 5.6 The framework of the cancer margin assessment showing training in upper and inference in lower stages.

We extract a patch of size 150 x 150 (x-z) pixels image starting from the topmost layer of the tissue and upto the bottommost layers (~250 pixels) with an overlapping patch of 2/3 in the next patch. We found that in some cases the speed of the prediction increases but the margin assessment gets poor. Each patch is upsampled and classified with the help of the already trained network. The process is repeated for the region of interest (735 x 250 pixels) of an image. In CNN, the final fully-connected layer with softmax activation layer provides the vector probabilities for each sample. Each pixel of the patch is allocated a predicted class either 0 or 1 obtained from the network. For each pixel, we average the predicted classes over all patches in which the pixel is included. In this way, every pixel has an average prediction between 0 and 1. We set a threshold value i.e., if the pixel value is greater than 0.5 it will become 1and more likely to be malignant tissue. If it's less than 0.5 it will become 0 and more likely to be healthy tissue. The whole process is explained in figure 5.6. The test image is first pre-processed (flatted and upsampled) and then fed to the already trained network. The network separates the malignant portion of tissue from the normal tissue with the help of the above-mentioned algorithm. The light pink color in figure 5.6 represents the malignant portion of tissue, yellow color represents the healthy part of the tissue and magenta color represent DC or background. The test OCT B-scan (x-z) image shown in the figure 5.6 have a cancerous boundary, which is also confirmed from the cross-sectional histology image (x-y). There might be some errors in finding the exact boundaries of malignant tissue but it will assist the surgeon in locating the malignant tissue region. We also tried a different size of patches such as 40 x 40 pixels, 60 x 60 pixels,10 x 10 pixels, 20 x 20 pixels and a threshold 0.33, 0.75. By the number of iterations, we found the best solution for the patch size is 30 x 30 with a threshold value of 0.5. This process is tested for the number of samples. In this preliminary study, database size is small, we can fine-tune only the last fully connected layer of the deep CNN. For the better performance and robustness of the model, the larger dataset will be collected to fine-tune more layers of the pre-trained deep CNN. With the help of CNN, we can localize the region of the cancer tissue and with the high-end system, this would become a feasible solution for intra-operative applications.

5.4 CONCLUSIONS

Our study performs encouraging classification with the help of deep learning-based CNN model in distinguishing malignant breast tissue from normal breast tissue using an OCT system with high sensitivity 90.2% and specificity 91.7 %, respectively. With more image data and addition of different classes of breast cancer will make the system more robust and support in clinician decisions. The cancer margin assessment results show the effectiveness of the model. We expect that our proposed method in future will be helpful to monitor the individual patient health progress and success of therapy by automatically extracting the hidden image information.

CHAPTER 6

PHASE SHIFTING FULL-FIELD OPTICAL COHERENCE MICROSCOPE: A TOOL FOR HUMAN BREAST TISSUE AND RED BLOOD CELLS IMAGING

6.1 INTRODUCTION

Non-destructive imaging of the internal structure of the biological samples is the active area of research [3], [57], [222]. Optical microscopy is a non-contact and non-invasive imaging technique for the investigations of biological cells and tissues for both in vivo and in vitro analysis [14], [38], [57], [160], [188], [223]–[225]. In the recent years, lot of research is going on the development of optical microscope whose to achieve a lateral resolution comparable to the histology to explore the microstructure of the biological cells and tissues [50], [56], [226]. Confocal microscopy is a very high resolution (<1 µm) cross-sectional imaging technique but the depth of penetration in most of the biological samples is very less (<200 µm) [34], [169], [227]. Optical coherence tomography (OCT) is another noninvasive imaging technique to achieve high resolution (less than confocal) and deeper penetration depth (~1mm) opened a new field of research in biomedical imaging [3], [19], [50], [56], [228]. The basic principle behind the OCT is low coherence interferometry. Full-field optical coherence tomography (FF-OCT) also known as Full-field optical coherence microscopy (FF-OCM) is an technology extension of an OCT to achieve higher resolution comparable to histology with little comprise of depth of penetration [3], [68], [227], [229], [230]. It uses a 2D array of photodector in place of a photodetector as in the case of conventional OCT system to avoid transverse scanning. The axial resolution of the system is governed by the bandwidth of the light source and the spatial resolution of the system is a function of numerical aperture (NA) [68], [85], [137], [138]. Currently most of the FF-OCM system are based on low coherence interferometry uses SLD as a light source [33], [54], [139]. To achieve a better axial resolution (<1µm) Halogen and Xenon lamps are the good alternative to SLD. Xenon lamp provides good irradiance as compare to halogen lamp but it also produces artifacts to images and is also costly. FF-OCM system can be used for *ex vivo* study of cell and tissues without any staining and pre-processing steps. The phase map in the FF-OCM can be obtained by an arithmetic operation of multiple phase shifted interferograms. This method is based on phase shifting interferometry [33], [231], [232].

In the present chapter, a phase-shifting full-field optical coherence microscope (PS-FF-OCM) based on white light source is used for the quantitative phase imaging of different biological samples. It uses a low-cost white light source, a conventional optical microscope, a nearly common path Mirau-interferometric objective lens and a three-chip color CCD camera. Phase shifted interferograms were recorded by the 3-chip color CCD camera and five phase-shifted algorithms is used for extracting the phase information from these recorded interferograms. The present system is used for the imaging and quantification of excised human breast tissues obtained from 12 different patients and later on the system is used for the study of stored RBCs.

6.2 PRINCIPLE OF PS-FF-OCM System

The system works on the principle of low coherence or white light interferometry. Images information is extracted from the recorded interference images. Interference will occur when the path difference between object and reference mirror is within the coherence length. Two light beams (reference and object) interfere after an interaction of the object beam with the measured object, i.e. the beam is transmitted or reflected by the object and the beam is transmitted or reflected by the reference. The distribution of the intensity of the interference field is then detected, e.g. using a photographic film, CCD camera, etc. The phase difference between the reference and the object beam can be determined by phase-shifting algorithms [233], [234]. The phase shifting technique is based on an evaluation of the phase of the interference signal using phase modulation of this interference signal. With the help of PZT, the phase is shifted by moving the reference mirror (within the Mirau Interferometer) mechanically. Due to the non-linear movement or vibrations occur in PSI, some errors can be generated. In PSI, all the measurements correspond to known phase shifts. If there is an increment or decrement in the phase shift due to the movement of PZT or vibrations then resultant shift in phase does not subdivision of 2π. So shift error in reference phase leads to error in measured phase maps [235]. In order to minimize this error, many algorithms are developed such as Carre’s [235], Hariharan [233] and Schwider [231] algorithms which are insensitive to such kind of errors. Among of all the algorithms, Hariharan algorithm is utilized to achieve the five frame phase maps. To extract the phase information from the recorded interferograms 5-step phase shifting algorithm is used [231]. The intensity distribution of recorded interferogram by the camera at any point is given by equation (6.1):

$$I_i(x,y) = \mathrm{I}'(x,y) + I''(x,y)\cos[\Delta\emptyset(x,y) + \delta_i] \quad (6.1)$$

i = 1,……..,5

where, I' is the function of the background intensity, I'' is the function of the amplitude modulation, $\Delta\emptyset$ is the phase difference of the wave fields that interfere and δ_i is the phase shift of ith intensity measurement.

Five step phase shift algorithms

For quantitative phase maps, five frame phase shifting interferometry is widely preferred over the other phase shifting interferometry because of minimum phase error [236]. Five-phase shifted interferogram were recorded by assuming a linear phase shift of a between frames [237]:

$$\delta_i = -2\alpha, -\alpha, 0, \alpha, 2\alpha$$

i= 1, 2, 3, 4, 5

Then

$$I_1(x,y) = I'(x,y) + I''(x,y)\cos[\emptyset(x,y) - 2\alpha] \quad (6.2)$$

$$I_2(x,y) = I'(x,y) + I''(x,y)\cos[\emptyset(x,y) - \alpha] \quad (6.3)$$

$$I_3(x,y) = I'(x,y) + I''(x,y)\cos[\emptyset(x,y)] \quad (6.4)$$

$$I_4(x,y) = I'(x,y) + I''(x,y)\cos[\emptyset(x,y) + \alpha] \quad (6.5)$$

$$I_5(x,y) = I'(x,y) + I''(x,y)\cos[\emptyset(x,y) + 2\alpha] \quad (6.6)$$

By solving the equations (6.2) to (6.6):

$$\frac{\tan[\emptyset(x,y)]}{2\sin\alpha} = \frac{I_2 - I_4}{2I_3 - I_5 - I_1} \quad (6.7)$$

Differentiating the equation (6.7) with respect to α

$$\frac{d}{d\alpha}\left\{\frac{\tan[\emptyset(x,y)]}{2\sin(\alpha)}\right\} = \frac{-\cos(\alpha)\tan[\emptyset(x,y)]}{2sin^2(\alpha)} \tag{6.8}$$

when, $\alpha = \pi/2$ the equation (6.8) becomes zero, therefore the phase becomes insensitive to phase shift calibration errors, and equation (6.8) reduces to equation (6.9):

$$\emptyset(x,y) = \tan^{-1}\left[\frac{2I_2-2I_4}{2I_3-I_5-I_1}\right] \tag{6.9}$$

6.3 EXPERIMENTAL STUDY OF PS-FF-OCM SYSTEM

The PS-FF-OCM system was developed with the help of halogen lamp (white light) source, collimating lens, beam splitter, Mirau interferometer, PZT (Piezo, Jena, MIPOS 3) and a 3-chip color CCD (JAI GigE AT-140GE) camera. Figure 6.1 shows the schematic diagram of PS-FF-OCM system.

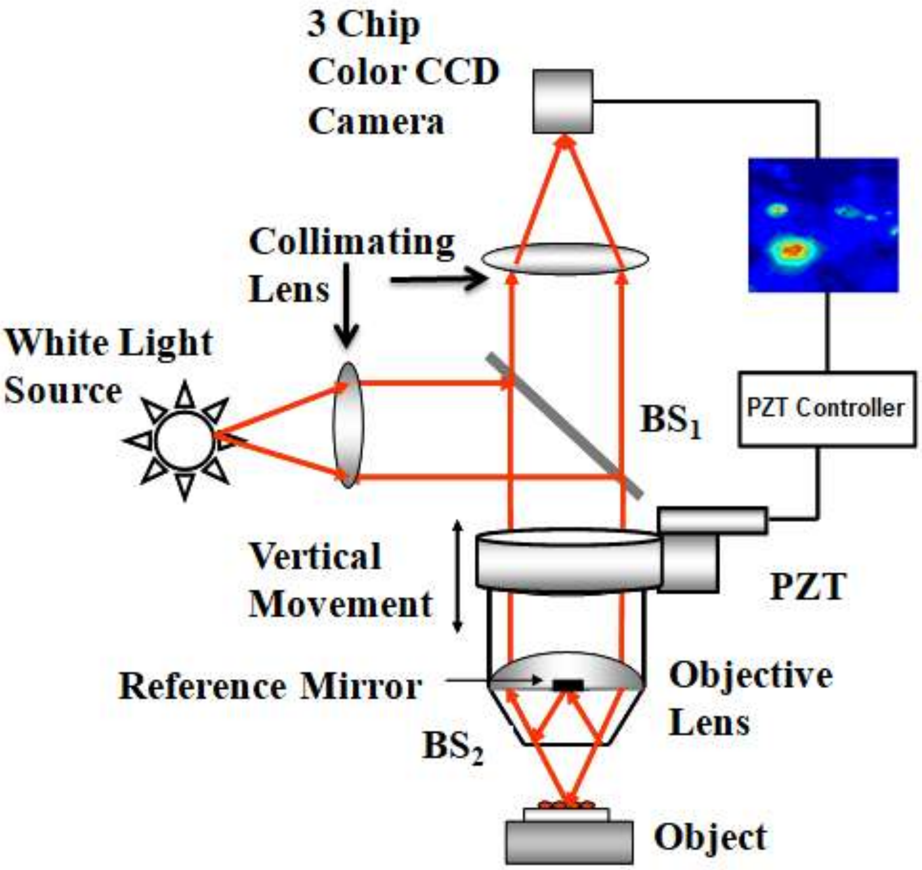

Figure 6.1 Schematic diagram of PS-FF-OCM system.

Light coming out from the white light source (coherence length of approximately 1 mm) is collimated by the collimating lens and made incident onto a beam splitter (BS_1). Further, the beam splitter directs the beam towards Mirau interferometer (Model No 503210, 50X/0.55 DI, WD 3.4 Nikon, Japan). Within the interferometer the light travels the same path upto beam splitter (BS_2) and divides into two parts, one part of the beam is going towards sample and other part is going toward reference mirror (within the interferometer). The beam reflected from the reference mirror and the beam reflected from sample again recombines at BS_2. When the path difference between the reference beam and sample beam is within the coherence length interference occurs and recorded by CCD camera.

Further, the PZT attached to the Mirau interferometer is driven by the amplifier and the whole system is interfaced with a personal computer. To introduce the phase-shift between the reference and sample beam, the PZT moves the interferometer with inbuilt reference mirror in the axial direction. The five phase-shifted interferograms were recorded by the 2-D CCD camera (1392 × 1040 pixels with pixel size 4.65 × 4.65 μm^2, 20 frames/second) and stored in the interfaced computer for further processing.

6.4 PERFORMANCE OF PS-FF-OCM SYSTEM

Coherence is an important factor for getting the interference fringes. Interference will occur only when the OPD between the reference and object arms lie within the coherence length of the light source. The white light interference pattern is recorded by a three chip color CCD camera. Hence, these two factors are very important in this experiment. In the present chapter we use white light halogen lamp whose spectrum is given below.

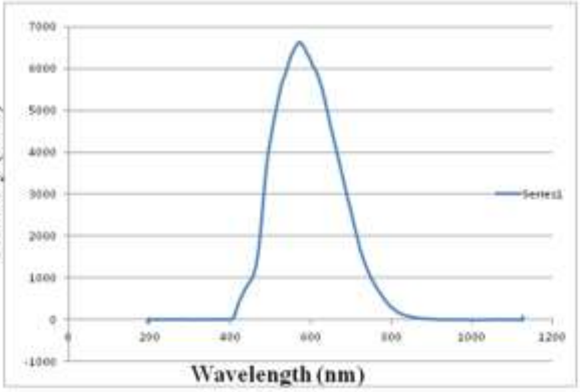

Figure 6.2 Spectral distribution of white light source (halogen lamp).

The spectrum of the white light source used in the microscope is recorded and the peak wavelength and bandwidth of the spectrum is computed and the spectral distribution can be seen in figure 6.2 The wavelength ranges from 400 nm – 800 nm and the shape of spectrum is nearly Gaussian. It can be seen from figure 6.2 that the peak occurs at wavelength 600 nm and FWHM is 200 nm. Coherence length of the halogen lamp can be calculated from equation (2.4) and comes out to be 1.6 μm where λ_0 is 600 nm and $\Delta\lambda \approx 200$ nm.

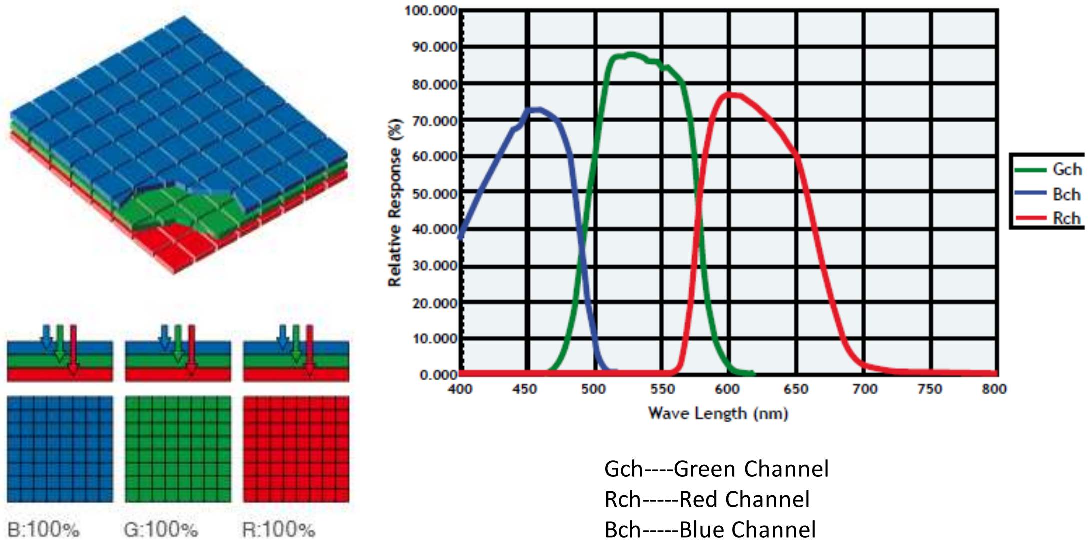

(a) (b)

Figure 6.3 (a) Image sensor and (b) spectral response of the three-chip color CCD camera, respectively.

To capture color information, a three-chip color CCD camera is used. The primary color filters of this image sensor are arranged in the layout shown in the figure 6.3 (a). According to the spectral response curve of the color CCD camera shown in the figure 6.3 (b), there is a small intensity cross talk between the blue and green and green and red channels. For the characterization of the system the axial and lateral resolutions were determined experimentally. To get the axial resolution, we placed a reflecting mirror in place of sample and scanned it on axially direction (Z-direction) and stacked these interferograms. The envelope of these stacked interferograms was obtained. The full width half maximum (FWHM) of this envelope is the coherence length and the measured value is to be 1.2 μm as seen in figure 6.4 (a). Hence, axial resolution is 0.6 μm, (which is half of the coherence length as already discussed in the chapter 2) where X-axis is the axial distance in the Z-direction in micron and Y-axis represents the normalized intensity.

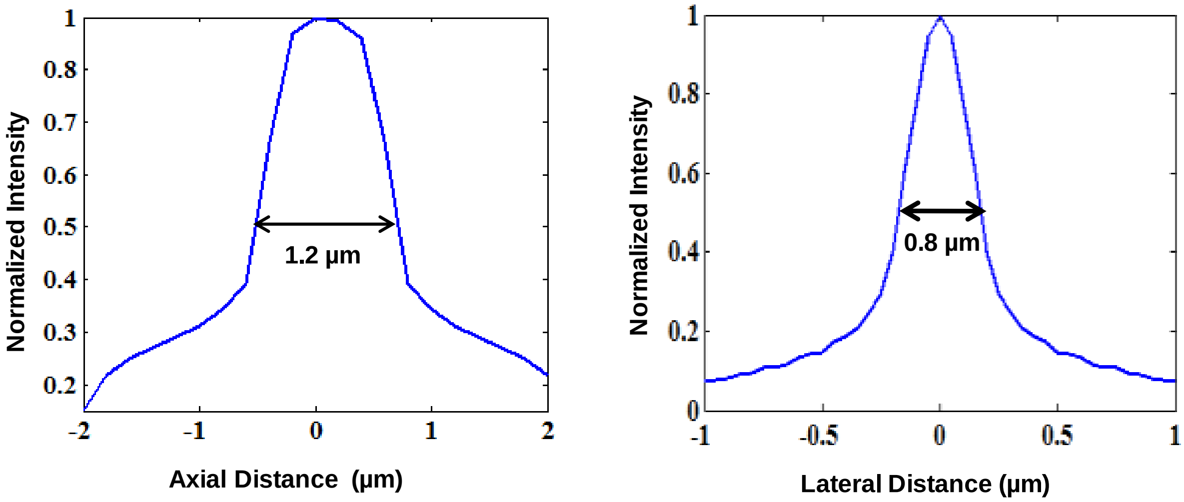

Figure 6.4 (a) Axial resolution and (b) lateral resolution of PS-FF-OCM system, respectively

For the calculation of the lateral resolution of the system, 1μm diameter polystyrene beads were place at the sample stage and were imaged by the system. The wavelength of illumination source is larger than the size of polystyrene beads, the image of each of them represents the point-spread function (PSF) of the microscope which is calculated by the 50X Mirau objective lens. Hence the PSF which is basically a line profile as a function of lateral position is shown in figure 6.4 (b), i.e., the measured lateral resolution is 0.8 μm, where X-axis is the lateral distance perpendicular to the direction of illumination and Y-axis represents the normalized intensity. Multiple white light interferogram of breast tissues and stored RBCs were recorded to use phase shifting algorithms for quantitative phase evaluation.

6.5 HUMAN BREAST CANCER TISSUE IMAGING USING PS-FF-OCM SYSTEM

6.5.1 Introduction

The importance of the diagnosis of the human breast cancer is already discussed in the previous chapter at page no. 69. Over the last few years, various non-invasive optical imaging techniques have been employed for *in vivo* and *ex vivo* cancer tissue diagnosis such as reflectance confocal microscopy, OCM, coherence-controlled holographic microscopy, DHM and spatial light interference microscopy [29], [85], [118], [238], [239]. The major disadvantage of the above-mentioned optical techniques that either they are using laser light source which will generate speckles or point-by-point scanning system which will generate motion artifacts as well as time-consuming [52], [66]. FF-OCM system with light source offers high resolution as well as relatively fast assessment due to two-dimensional CCD camera instead of a photodetector. In the present study, we demonstrate the PS-FF-OCM system for finding the quantitative phase images of the normal and malignant breast tissues. Due to a good axial as well as lateral resolution of the system, it's an ability to differ adipose tissue, fibrous stroma, breast lobules and ducts, as well as *in situ* and invasive carcinomas. The present study is designed to find the presence or absence of relevant features of the malignant tissue with the help of the PS-FF-OCM system which can give the accurate information. Morphological features were extracted from phase images of the normal and malignant breast tissues recorded by PS-FF-OCM system.

6.5.2 Experimental Results

An *ex vivo* experimental study was done on 12 subjects (6 healthy and 6 malignant tissue) freshly excised breast tissue over an area of ~2 cm^2 using PS-FF-OCM system. All the tissue samples were collected from AIIMS New Delhi to perform the study. The sample preparation process is already discussed in the previous chapter at page no. 71. Figure 6.5 shows the five exactly $\pi/2$ phase shifted interferograms of human breast tissue.

.

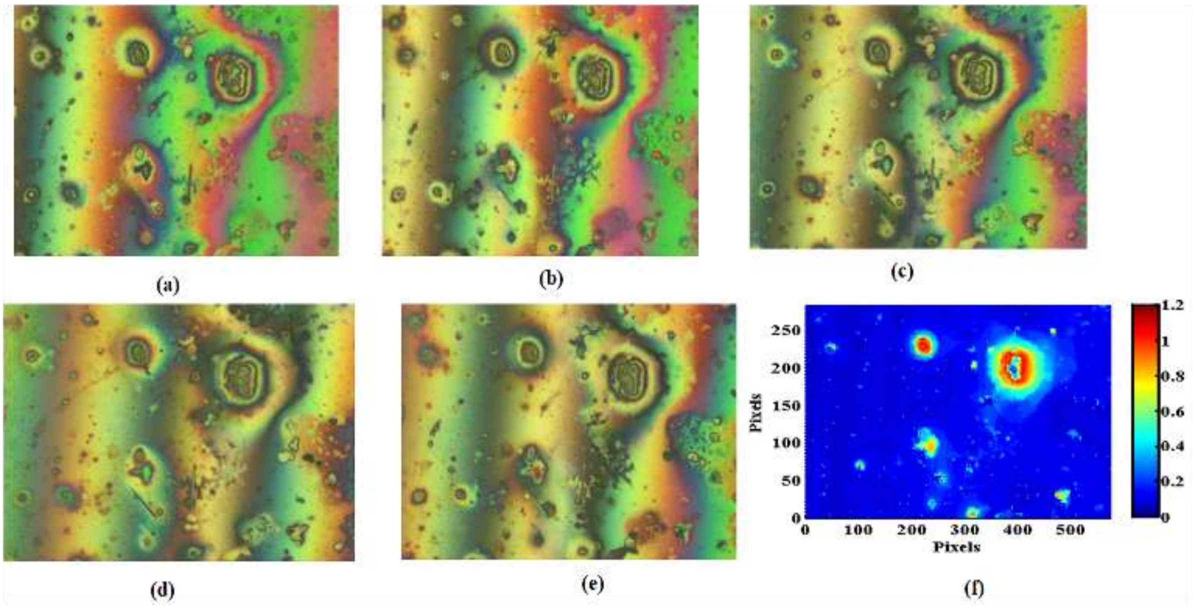

Figure 6.5 Malignant Human Breast Tissue (a)-(e) Five Phase shifts interferogram and (f) phase image (radian), respectively.

To differentiate between healthy and malignant breast tissues, five phase-shifted interferogram were recorded with the help of PS-FF-OCM system as shown in figure 6.5 (a)-(e). An algorithm for extracting the phase information is written in a MATLAB. The phase information is extracted with the help of equation no (6.9) as shown in figure 6.5 (f) malignant human breast tissue. The morphological features were extracted of the normal and malignant human breast tissues phase images. Three features were extracted from phase images such as spatial mean phase, entropy and spatial standard deviation, which is calculated by the equations (6.10), (6.11) and (6.12).

Spatial Mean Phase (S_φ): describes the mean phase value of the human breast tissue.

$$S_\varphi(x,y) = \overline{\Delta\phi}(x,y) \tag{6.10}$$

where, x, y represents the no. of pixels of the phase image in horizontal and vertical direction.

Entropy: describes the randomness of the human breast tissue.

$$Entropy(x,y) = -\sum_{i=1}^{N}\sum_{j=1}^{M} p(x_i, y_j)\log_2 p(x_i, y_j) \tag{6.11}$$

where, p is the probability of each phase value of the phase image and discussed previously in chapter 3, i^{th} and j^{th} are the pixels in the horizontal and vertical direction, $N \times M$ is the total no. of pixels.

Spatial Standard Deviation (S_{std}): signifies the variations in the phase values of the human breast tissue.

$$S_{std}(x,y) = \frac{\sqrt{\sum \left(\Delta\phi(x,y) - \overline{\Delta\phi}(x,y)\right)^2}}{N} \tag{6.12}$$

Table 6.1 shows the mean values of all the features were extracted from the normal and malignant human breast tissue. The malignant human breast tissue has higher spatial mean phase value as compared with the normal one that attributes to aggravated necrosis and reduced collagen concentration.

Table 6.1 Mean values of normal and malignant human breast tissue

Features	**Human Breast tissues**	
	Normal	***Malignant***
Spatial Mean phase	0.106 (radian)	0.64 (radian)
Entropy	2.96	3.201
Spatial Standard Deviation	0.147 (radian)	0.249 (radian)

Furthermore, the other features entropy and spatial standard deviation also gives the higher mean values in malignant breast tissues, which describes more heterogeneity and clustering associated with cancer growth. It can be observed from the figure 6.3(f) that the malignant tissue has highly degraded and heterogeneous stroma.

6.6 STORED RED BLOOD CELLS IMAGING USING PS-FF-OCM SYSTEM

6.6.1 Introduction

Blood storage is necessary to procure the emergency transfusion while surgical treatment. It is useful in medical exercise to exchange blood release or to compensate the loss of blood constituents [240]. Blood storage can be possible up to 42 days under certain condition [241]. The long duration storage of the blood affects the changes in the blood properties e.g. see the alterations in the morphological features of the RBCs [240]. During storage red blood cells will undergoes numerous functional, biochemical and structural changes. Three different shapes of RBCs (discocyte, echinocyte and spherocyte) are seemed within a period of 42 days. In the last decades, QPI methods has been presented as a valuable tool to extract the relevant information of the three dimensional biological objects such as live cells, red blood cells etc [134]. Several studies have been done to determine the changes in the RBCs shapes and their morphological features during storage time using various optical imaging techniques such as scanning electron microscopy, Spatial light interference microscopy (SLIM) and digital inline holographic microscopy [241]. However, the system was very complex which they had used and time consuming process [240], [241]. In this section, the quantitative phase images of the RBCs were extracted from the stored RBCs with the help of PS-FF-OCM system. This system is very useful for finding the quantitative information of the biological studies as already discussed. We can express the morphological changes in the stored RBCs in terms of various parameters such as spatial mean phase, spatial root mean square, spatial standard deviation, spatial skewness and spatial kurtosis are discussed in this chapter later.

6.6.2 Experimental Results

An experimental study was done on 20 stored RBCs samples. Blood samples were collected from the pathology lab. Sample preparation process for the experimental study and ethical clearance is already discussed in chapter 3.

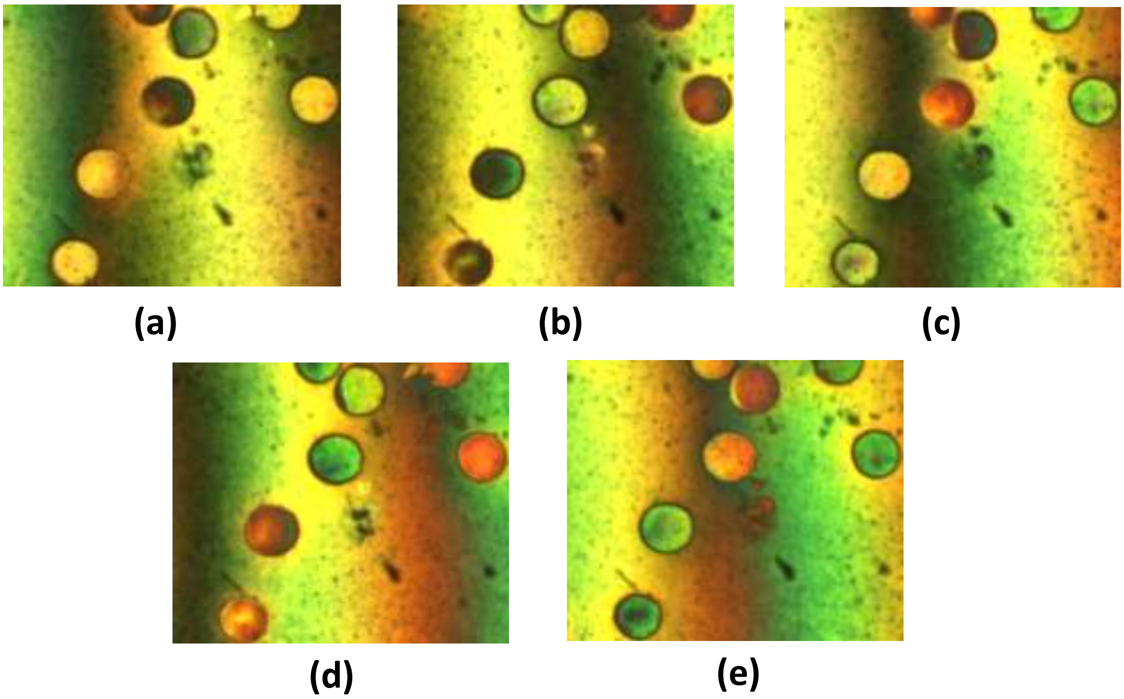
(a) (b) (c)

(d) (e)

Figure 6.6 (a)-(e) Five Phase shifts interferogram of the stored RBCs (after one week of storage)

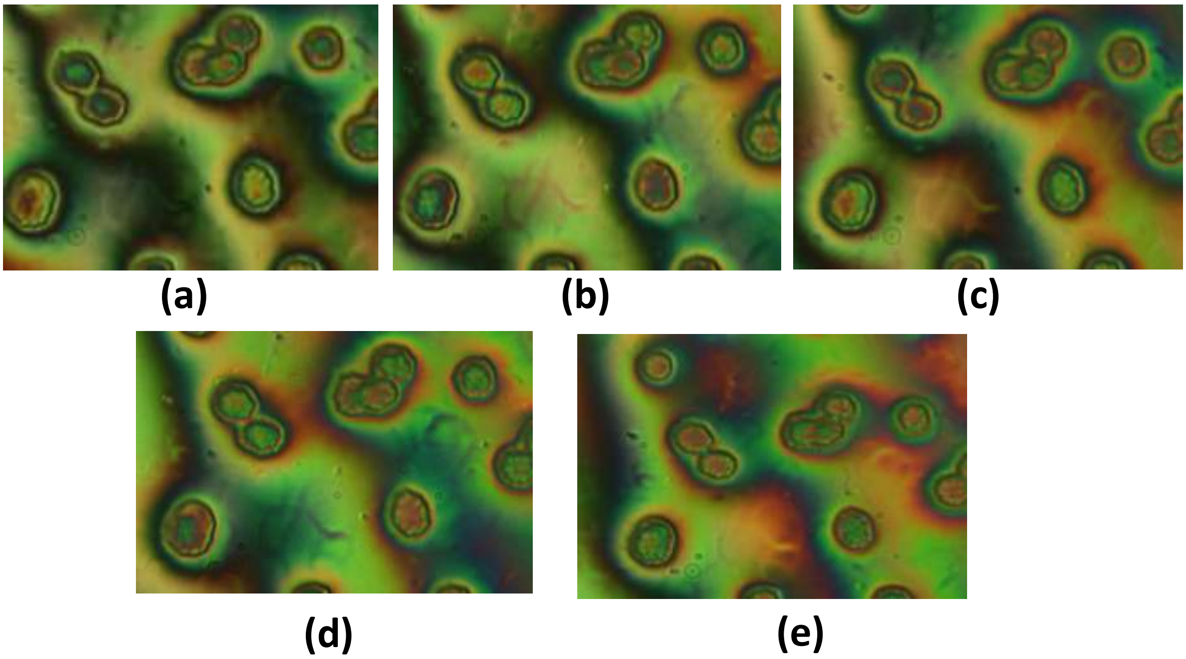

Figure 6.7 (a)-(e) Five Phase shifts interferogram of the stored RBCs (after three week of storage)

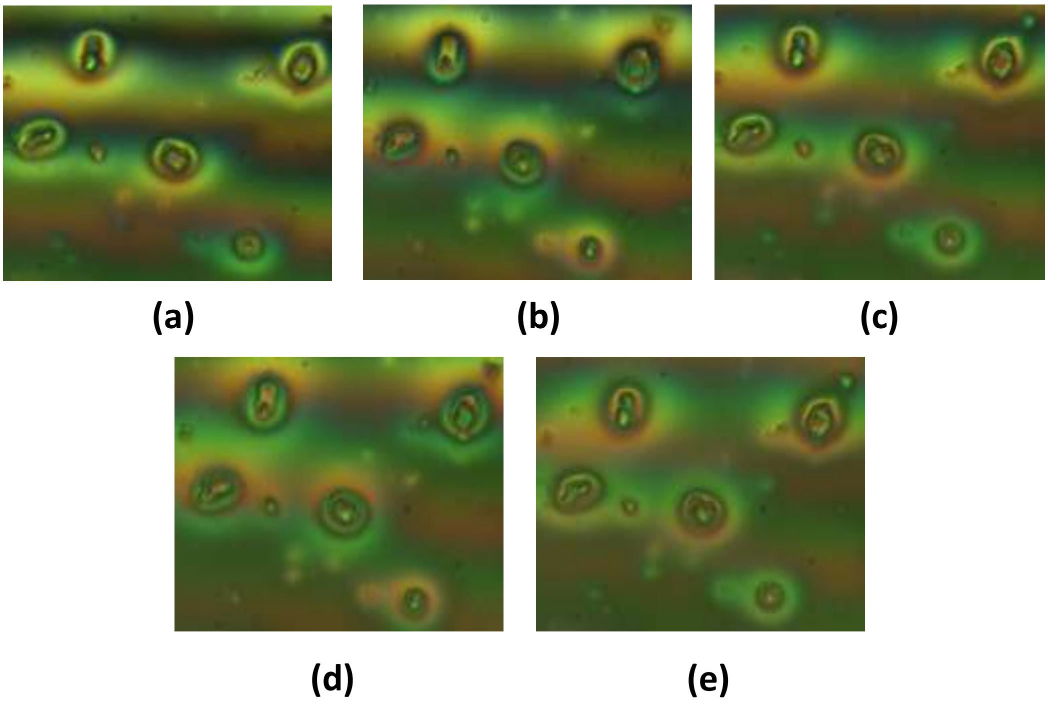

Figure 6.8 (a)-(e) Five Phase shifts interferogram of the stored RBCs (after five week of storage)

The spatial five phase shifted interferograms recorded by the PS-FF-OCM system at different time interval is shown in the figure 6.6 (a-e), 6.7 (a-e), and 6.8 (a-e), respectively. The wrapped phase map of the RBC is extracted with the help of equation (6.9) and were unwrapped by Goldstein method [17]. With the time, RBCs suffered the morphological states from discocyte to echinocyte and spherocyte as shown in figure 6.9 (a-c), respectively.

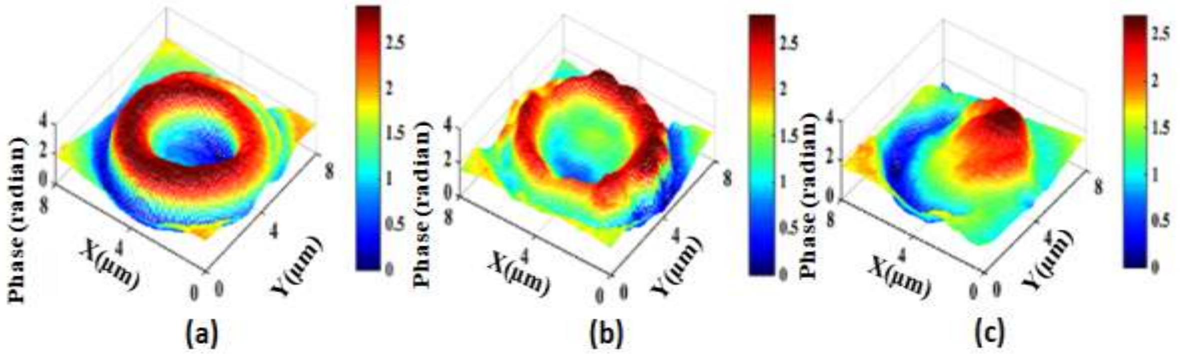

(a) (b) (c)

Figure 6.9 Phase images of stored RBCs with a function of time (a) Discocyte (after one week of storage) (b) Echinocyte (after three weeks of storage) and (c) Spherocyte (after five weeks of storage), respectively

S_φ: describes the mean phase value of the RBC cell. The formula is already written in equation (6.10).

Spatial Root Mean Square (S_{RMS}): gives the information about the distance the phase values from the mean phase values of the RBC cell.

$$S_{RMS} = \sqrt{\sum \left(\Delta\phi(x,y) - \overline{\Delta\phi}(x,y)\right)^2} \qquad (6.14)$$

Spatial standard Deviation (S_{std}): signifies the variations in the phase values of the cell. The formula discussed in equation (6.12).

Spatial Skewness (S_{sk}): measures the distribution of the phase values around the mean value and give its shape.

$$S_{sk} = \frac{\sqrt{\sum \left(\Delta\phi(x,y) - \overline{\Delta\phi}(x,y)\right)^3}}{S_{std}^{\ 3}} \qquad (6.15)$$

Spatial Kurtosis (S_{kur}): calculates from the histogram and extent upto the shape of the distribution equals to the normal distribution.

$$S_{kur} = \frac{\sqrt{\sum \left(\Delta\phi(x,y) - \overline{\Delta\phi}(x,y)\right)^4}}{S_{std}^{\ 4}} \qquad (6.16)$$

Table 6.2 RBC Morphology features

Features	Different shapes of RBCs with time		
	Discocyte	**Echinocyte**	**Spherocyte**
Spatial Mean phase	1.21(radian)	1.25 (radian)	1.187 (radian)
Spatial Root Mean Square	1.35 (radian)	1.31 (radian)	1.24 (radian)
Spatial Standard Deviation	0.57 (radian)	0.49 (radian)	0.34 (radian)
Spatial Skewness	0.003	0.004	0.002
Spatial Kurtosis	0.024	0.024	0.025

We extracted five morphological features including Spatial Mean phase, Spatial Root Mean Square, Spatial Standard Deviation, Spatial Skewness and Spatial Kurtosis of the different shapes of RBCs as mentioned in table 6.2. Spatial Mean phase values of all the samples are almost associated in a small region so standard deviation and spatial root mean square of phase values are reduced during the storage period of RBCs. From the other parameters, it is seen in table 6.2 that the spatial skewness values close to zero give the symmetrical distribution of phase values, which describes well-adhered cells and spatial kurtosis also gives the changes in values during the storage RBCs.

6.7 CONCLUSIONS

In summary, we presented PS-FF-OCM based on white light as an imaging tool for the study of breast cancer and stored RBCs. Quantitative features were extracted from the phase maps of the breast cancer and stored RBCs. In this study, PS-FF-OCM system imaged large area of tissue in a non-destructive manner with high resolution which will help the pathologist for the diagnosis. The sample doesn’t require any type of special preparation therefore PS-FF-OCM can be a potential intraoperative tool for the margin assessment of the cancerous tissues and the characterization of the different stages of RBCs. The system is compact, efficient, user-friendly and also gives high lateral and axial resolution which makes system useful to clinical pathology labs.

CHAPTER 7

CONCLUSIONS AND FUTURE SCOPE

7.1 CONCLUSIONS

The work presented in this thesis describes the development of the automated high-resolution full-field optical spatial coherence microscope (FF-OSCM) system for extracting the quantitative phase images of the biological applications like human cells and tissues etc. The performance of the developed system has been characterized by measuring the optical parameters such as axial resolution, lateral resolution, spatial and temporal phase sensitivity. The developed system was slightly off-axis in nature which is very helpful to study the dynamic behaviour of cells with good accuracy and precision. In addition to this, as the spatial coherence of the system was reduced, the developed system achieved the high axial resolution and lateral resolution. The obtained resolution of the developed system is comparable to conventional OCT system based on temporal coherence. However, the main advantage of this system is free from chromatic abbreviation as it is based on highly monochromatic laser source.

In addition to that, the developed FF-OSCM system was used for differentiating the malaria infected RBCs from the healthy RBCs. Quantitative phase images-based features were calculated and used to train the multi-ensemble classifier for an automated classification between malaria infected RBCs and healthy RBCs in terms of high accuracy, sensitivity and specificity. The proposed classifier obtained 96.1% and 97.9% average accuracy in detecting early trophozoite and late trophozoite malaria infected stages of RBCs. Later on, this system was designed with multi-wavelength laser sources for *ex-vivo* imaging RBCs and TL algorithms applied for the classification of different stages of malaria infected RBCs with limited labelled datasize. In this study, customized CNN based TL model with SCM system was used for task-specific classification like classifying the healthy vs infected cells and early vs late trophozoite cells. Results also compared with other known CNN models and our customized model obtained 97.7% accuracy, 98.3% sensitivity and 96.9% specificity, respectively, for healthy and malaria infected RBCs whereas in the case of malaria-infected stages between early and trophozoite 91.2% accuracy, 90.3% sensitivity and 90.7% specificity, respectively with less computational time.

In the next part of this thesis, the study describes human burn skin tissue samples were imaged *in vivo* using SS-OCT system. Quantitative features were extracted from the normal and burned tissue images and were analysed using machine learning algorithm. Least sum of squares method-based learning model was used for the classification between the normal and burned tissue with obtained 91% accuracy. The performance shows that the quantitative features from both A-scan and B-scan OCT images can be powerful *in vivo* diagnostic tool for quantitative analysis of burned tissues without a specialized facility and clinician.

An automatic classification algorithm is developed to differentiate between the malignant breast and normal breast tissue using OCT images. A reverse active learning with fine-tuned pre-trained inception-v3 CNN is used to differentiate between the malignant breast and normal breast tissue. To overcome the challenges of over fitting and to increase the cardinality of the dataset (both the classes), data augmentation techniques have been applied and obtained high sensitivity 90.2% and specificity 91.7%. The cancer margin assessment results show the effectiveness of the developed model.

By ending of this thesis, we have demonstrated PS-FF-OCM system for the biological applications like human stored RBCs and breast cancer tissue. PS-FF-OCM system based on white light source with high NA achieves high axial and lateral resolution. The PS-FF-OCM imaging system is compact, common path and ease to align as compared to other methods.

7.2 FUTURE SCOPE

In the future studies, the quantitative idea of this technique disposes of intra-and inter observer contrasts. The utility of this technique with cells and tissue makes it fit in well with current pathology rehearses, without the requirement for changes in tissue handling pipelines. Also, the morphological data in H&E images is recovered subjectively in phase images, thus enabling pathologists to perform image segmentation, when important, without the requirement of additional training for recognizable proof of tissue compartments, as saw in the subjective analysis of tissue images by our pathology colleagues. Since QPI maps are self-aligning as for brightening, machine learning execution for computerized grouping will be less demanding to actualize. The quick filtering capacity of OCT frameworks will likewise help in circumstances where high throughput is required, as in screening settings.

Moreover, we hope to explore our knowledge and experience which gained in my thesis work to classify other biological applications like sickle cells, diabetes, cancer cells etc.

Based on the performance results, we expect that our proposed method in chapter 3 will be helpful to monitor the individual patient health progress and success of therapy by automatically extracting the hidden image information. A more accurate segmentation algorithm will be used to incorporate overlapping RBCs and the present developed FF-OSCM system will be modified to get the spectral response of the cells which will strengthen the performance for the classifying other diseases. Our proposed model can be very useful for other limited labelled biological studies. In future, the developed algorithm in chapter 4 can be used in differentiating between various grades of burn injuries and also studying fresh burn injuries. Our results lay the foundation for the future that the proposed method in chapter 5 and chapter 5 can be used to perform automatic intra-operative identification of breast cancer margins in real-time and to guide core needle biopsies. With more image data and the addition of different classes of breast cancer tissue will make the proposed algorithm more robust and great support in clinician decisions. The system designed in chapter 6 can be used in clinical pathology labs for the quantification of different biological samples.

REFERENCES

[1] Huang, D et al. (1991). Optical coherence tomography. S*cience*, *254*(5035), 1178-1181.

[2] Popescu, D. P et al. (2011). Optical coherence tomography: fundamental principles, instrumental designs and biomedical applications. *Biophysical reviews*, *3*(3), 155.

[3] Grieve, K et al. (2005, April). Full-field OCT: ex vivo and in vivo biological imaging applications. In *Coherence Domain Optical Methods and Optical Coherence Tomography in Biomedicine IX* (Vol. 5690, pp. 31-39). International Society for Optics and Photonics.

[4] Sarunic, M. V., Applegate, B. E., & Izatt, J. A. (2005). Spectral domain second-harmonic optical coherence tomography. *Optics letters*, *30*(18), 2391-2393.

[5] McLaughlin, R. A., Lorenser, D., & Sampson, D. D. (2013). Needle probes in optical coherence tomography. *Handbook of Coherent-Domain Optical Methods: Biomedical Diagnostics, Environmental Monitoring, and Materials Science*, 1065-1102.

[6] Chowdhury, S., & Izatt, J. A. (2016, April). Simultaneous fluorescence and phase imaging with extensions toward sub-diffraction resolution via structured-illumination (Conference Presentation). In *Three-Dimensional and Multidimensional Microscopy: Image Acquisition and Processing XXIII* (Vol. 9713, p. 97131J). International Society for Optics and Photonics.

[7] Kemper, B., Langehanenberg, P., & Bauwens, A. (2013). Holographic Microscopy Techniques for Multifocus Phase Imaging of Living Cells. In *Biomedical Optical Phase Microscopy and Nanoscopy* (pp. 97-128). Academic Press.

[8] Zernike, F. (1942). Phase contrast, a new method for the microscopic observation of transparent objects part II. *Physica*, *9*(10), 974-986.

[9] Kraut, S., & Cowley, J. M. (1993). A simplified mode of differential phase contrast Lorentz microscopy. *Microscopy research and technique*, *25*(4), 341-345.

[10] Hoffman, R., & Gross, L. (1975). Modulation contrast microscope. *Applied Optics*, *14*(5), 1169-1176.

[11] Zernike, F. (1955). How I discovered phase contrast. *Science*, *121*(3141), 345-349.

[12] Pham, H. V. et al. (2013). Real time blood testing using quantitative phase imaging. *PloS one*, *8*(2), e55676.

[13] Rosen, J., & Takeda, M. (2000). Longitudinal spatial coherence applied for surface profilometry. *Applied optics*, *39*(23), 4107-4111.

[14] Popescu, G. (2011). *Quantitative phase imaging of cells and tissues*. McGraw Hill

Professional.

[15] Singla, N., Srivastava, V., & Mehta, D. S. (2018). Development of full-field optical spatial coherence tomography system for automated identification of malaria using the multilevel ensemble classifier. *Journal of biophotonics*, *11*(5), e201700279.

[16] Yamaguchi, I., & Zhang, T. (1997). Phase-shifting digital holography. *Optics letters*, *22*(16), 1268-1270.

[17] Yoon, S. K et al. (2007). Phase Unwrapping using Modified Goldstein Algorithm in Digital Holography. *Korean Journal of Optics and Photonics*, *18*(2), 122-129.

[18] Popescu, G et al. (2004). Fourier phase microscopy for investigation of biological structures and dynamics. *Optics letters*, *29*(21), 2503-2505.

[19] Tearney, G. J et al. (1996). Rapid acquisition of in vivo biological images by use of optical coherence tomography. *Optics letters*, *21*(17), 1408-1410.

[20] Aknoun, S et al. (2015). Living cell dry mass measurement using quantitative phase imaging with quadriwave lateral shearing interferometry: an accuracy and sensitivity discussion. *Journal of biomedical optics, 20*(12), 126009.

[21] Popescu, G et al. (2008). Imaging red blood cell dynamics by quantitative phase microscopy. *Blood Cells, Molecules, and Diseases*, *41*(1), 10-16.

[22] Jung, J et al. (2016). Optical characterization of red blood cells from individuals with sickle cell trait and disease in Tanzania using quantitative phase imaging. *Scientific reports*, *6*, 31698.

[23] Park, Y et al. (2011, February). Metabolic remodeling of the human red blood cell membrane measured by quantitative phase microscopy. In *Imaging, Manipulation, and Analysis of Biomolecules, Cells, and Tissues IX* (Vol. 7902, p. 79021M). International Society for Optics and Photonics.

[24] Lee, K et al. (2013). Quantitative phase imaging techniques for the study of cell pathophysiology: from principles to applications. *Sensors*, *13*(4), 4170-4191.

[25] Bhaduri, B et al. (2013) Real - time quantitative phase imaging in biomedicine. *SPIE Newsroom*, 1–5.

[26] Cho, S et al. (2012). Optical imaging techniques for the study of malaria. *Trends in biotechnology*, *30*(2), 71-79.

[27] Majeed, H et al. (2015). Breast cancer diagnosis using spatial light interference microscopy. *Journal of biomedical optics, 20*(11), 111210.

[28] Sridharan, S et al. (2015). Prediction of prostate cancer recurrence using quantitative phase imaging. *Scientific reports*, *5*, 9976.

[29] Nguyen, T et al. (2015, March). Prostate cancer diagnosis using quantitative phase

imaging and machine learning algorithms. In *Quantitative Phase Imaging* (Vol. 9336, p. 933619). International Society for Optics and Photonics.

[30] Beaurepaire, E. et al. (1998). Full-field optical coherence microscopy. *Optics letters*, *23*(4), 244-246.

[31] Vabre, L., Dubois, A., & Boccara, A. C. (2002). Thermal-light full-field optical coherence tomography. *Optics letters*, *27*(7), 530-532.

[32] Kuś, A et al. (2014). Tomographic phase microscopy of living three-dimensional cell cultures. *Journal of biomedical optics*, *19*(4), 046009.

[33] Singh Mehta, D., & Srivastava, V. (2012). Quantitative phase imaging of human red blood cells using phase-shifting white light interference microscopy with colour fringe analysis. *Applied Physics Letters*, *101*(20), 203701.

[34] Kim, T et al. (2014). White-light diffraction tomography of unlabelled live cells. *Nature Photonics*, *8*(3), 256.

[35] Park, Y et al. (2009). Spectroscopic phase microscopy for quantifying hemoglobin concentrations in intact red blood cells. *Optics letters*, *34*(23), 3668-3670.

[36] Popescu, G et al. (2005). Erythrocyte structure and dynamics quantified by Hilbert phase microscopy. *Journal of biomedical optics*, *10*(6), 060503.

[37] Ogien, J., & Dubois, A. (2016). High-resolution full-field optical coherence microscopy using a broadband light-emitting diode. *Optics express*, *24*(9), 9922-9931.

[38] Fujimoto, J. G., & Drexler, W. (2015). Optical coherence tomography: technology and applications.

[39] Watanabe, Y., Yamada, K., & Sato, M. (2006). In vivo non-mechanical scanning grating-generated optical coherence tomography using an InGaAs digital camera. *Optics communications*, *261*(2), 376-380.

[40] Guo, R. et al. (2014). LED-based digital holographic microscopy with slightly off-axis interferometry. *Journal of Optics*, *16*(12), 125408.

[41] Thomas, L et al. (2015). Phase-sharing using a Mach–Zehnder interferometer. *Applied optics*, *54*(4), 699-706.

[42] Krauter, J et al. (2015, June). Full-field swept-source optical coherence tomography with phase-shifting techniques for skin cancer detection. In *Optical Methods for Inspection, Characterization, and Imaging of Biomaterials II*(Vol. 9529, p. 952913). International Society for Optics and Photonics.

[43] Medoff, B. P et al. (1983). Iterative convolution backprojection algorithms for image reconstruction from limited data. *JOSA*, *73*(11), 1493-1500.

[44] Kadono, H., Ogusu, M., & Toyooka, S. (1994). Phase shifting common path

interferometer using a liquid-crystal phase modulator. *Optics communications, 110*(3-4), 391-400.

[45] Na, J et al. (2008). Image restoration method based on Hilbert transform for full-field optical coherence tomography. *Applied optics*, *47*(3), 459-466.

[46] Xue, L., Lai, J. C., & Li, Z. H. (2010, November). Quantitative phase microscopy of red blood cells with slightly-off-axis interference. In *Optics in Health Care and Biomedical Optics IV* (Vol. 7845, p. 784505). International Society for Optics and Photonics.

[47] Cuche, E., Marquet, P., & Depeursinge, C. (2000). Spatial filtering for zero-order and twin-image elimination in digital off-axis holography. *Applied optics*, *39*(23), 4070-4075.

[48] Wang, Z et al. (2011). Spatial light interference microscopy (SLIM). *Optics express*, *19*(2), 1016-1026.

[49] Popescu, G et al. (2006). Diffraction phase microscopy for quantifying cell structure and dynamics. *Optics letters*, *31*(6), 775-777.

[50] Fujimoto, G. J et al. (1995). Optical biopsy and imaging using optical coherence tomography. *Nature Medicine, 1,* 970-972.

[51] Tomlins, P. H., & Wang, R. K. (2005). Theory, developments and applications of optical coherence tomography. *Journal of Physics D: Applied Physics*, *38*(15), 2519.

[52] Subhash, H. M. (2012). Full-field and single-shot full-field optical coherence tomography: A novel technique for biomedical imaging applications. *Advances in Optical Technologies*, *2012*.

[53] Choma, M. A et al. (2003). Sensitivity advantage of swept source and Fourier domain optical coherence tomography. *Optics express*, *11*(18), 2183-2189.

[54] Chang, S et al. (2008). Large area full-field optical coherence tomography and its applications. *Open Opt. J.*, *2*(1), 10-20.

[55] Burcheri-Curatolo, A. (2012). *Advances of full-field optical coherence tomography (FFOCT) for clinical applications and developmental biology* (Doctoral dissertation, Université Pierre et Marie Curie-Paris VI).

[56] Zysk, A. M et al. (2007). Optical coherence tomography: a review of clinical development from bench to bedside. *Journal of biomedical optics*, *12*(5), 051403.

[57] Choi, W. (2012). Tomographic phase microscopy and its biological applications. *3D Research*, *3*(4), 5.

[58] Jung, W et al. (2005). Advances in oral cancer detection using optical coherence tomography. *IEEE Journal of Selected Topics in Quantum Electronics*, *11*(4), 811-817.

[59] Watanabe, Y., Yamada, K., & Sato, M. (2006). Three-dimensional imaging by ultrahigh-speed axial-lateral parallel time domain optical coherence tomography. *Optics*

express, *14*(12), 5201-5209.

[60] Fercher, A. F et al. (1995). Measurement of intraocular distances by backscattering spectral interferometry. *Optics communications*, *117*(1-2), 43-48.

[61] Leitgeb, R., Hitzenberger, C. K., & Fercher, A. F. (2003). Performance of fourier domain vs. time domain optical coherence tomography. *Optics express*, *11*(8), 889-894.

[62] Liu, X et al. (2008). Fiber-optic Fourier-domain common-path OCT. *Chinese Optics Letters*, *6*(12), 899-901.

[63] Ryabukho, V. P., et al. (2013). Wiener–Khintchin theorem for spatial coherence of optical wave field. *Journal of Optics*, *15*(2), 025405.

[64] Fergusson, J et al. (2010, February). In vitro retinal imaging with full field swept source optical coherence tomography. In *Optical Coherence Tomography and Coherence Domain Optical Methods in Biomedicine XIV* (Vol. 7554, p. 75540I). International Society for Optics and Photonics.

[65] Akiba, M., Chan, K. P., & Tanno, N. (2003). Full-field optical coherence tomography by two-dimensional heterodyne detection with a pair of CCD cameras. *Optics letters*, *28*(10), 816-818.

[66] Dubois, A., & Boccara, A. C. (2008). Full-field optical coherence tomography. In *Optical Coherence Tomography* (pp. 565-591). Springer, Berlin, Heidelberg.

[67] Popescu, G et al. (2006, October). Red Blood Cell Fluctuations During Osmolarity Changes. In *Frontiers in Optics* (p. FTuE1). Optical Society of America.

[68] Anna, T et al. (2011). High-resolution full-field optical coherence microscopy using a Mirau interferometer for the quantitative imaging of biological cells. *Applied optics*, *50*(34), 6343-6351.

[69] Federici, A., & Dubois, A. (2015). Full-field optical coherence microscopy with optimized ultrahigh spatial resolution. *Optics letters*, *40*(22), 5347-5350.

[70] Ducros, M et al. (2002). Parallel optical coherence tomography in scattering samples using a two-dimensional smart-pixel detector array. *Optics Communications*, *202*(1-3), 29-35.

[71] Yu, L., & Kim, M. K. (2004). Full-color three-dimensional microscopy by wide-field optical coherence tomography. *Optics express, 12*(26), 6632-6641.

[72] Boccara, A et al. (2007, October). Full-field optical coherence tomography (OCT) and early alterations in chloroplast morphology. In *Advanced Environmental, Chemical, and Biological Sensing Technologies V* (Vol. 6755, p. 67550E). International Society for Optics and Photonics.

[73] Chinn, S. R., Swanson, E. A., & Fujimoto, J. G. (1997). Optical coherence tomography using a frequency-tunable optical source. *Optics letters*, *22*(5), 340-342.

[74] Nguyen, T. M et al. (2014). Visualizing ultrasonically induced shear wave propagation using phase-sensitive optical coherence tomography for dynamic elastography. *Optics letters*, *39*(4), 838-841.

[75] Chin, L et al. (2017). Simplifying the assessment of human breast cancer by mapping a micro-scale heterogeneity index in optical coherence elastography. *Journal of biophotonics*, *10*(5), 690-700.

[76] Wang, G et al. (2018). Interactive medical image segmentation using deep learning with image-specific fine tuning. *IEEE transactions on medical imaging*, *37*(7), 1562-1573.

[77] Kowal, M et al. (2013). Computer-aided diagnosis of breast cancer based on fine needle biopsy microscopic images. *Computers in biology and medicine*, *43*(10), 1563-1572.

[78] Singh, J., & Arora, A. S. (2019). Automated approaches for ROIs extraction in medical thermography: a review and future directions. *Multimedia Tools and Applications*, 1-24.

[79] Vidotti, V. G et al. (2013). Sensitivity and specificity of machine learning classifiers and spectral domain OCT for the diagnosis of glaucoma. *European journal of ophthalmology*, *23*(1), 61-69.

[80] Li, W et al. (2015). Outlier detection and removal improves accuracy of machine learning approach to multispectral burn diagnostic imaging. *Journal of biomedical optics*, *20*(12), 121305.

[81] Ahirwar, N., Pattnaik, S., & Acharya, B. (2012). Advanced image analysis based system for automatic detection and classification of malarial parasite in blood images. *International Journal of Information Technology and Knowledge Management*, *5*(1), 59-64.

[82] Huang, X et al. (2016). Machine learning based single-frame super-resolution processing for lensless blood cell counting. *Sensors*, *16*(11), 1836.

[83] Venhuizen, F. G et al. (2015, March). Automated age-related macular degeneration classification in OCT using unsupervised feature learning. In *Medical Imaging 2015: Computer-Aided Diagnosis* (Vol. 9414, p. 94141I). International Society for Optics and Photonics.

[84] Das, D. K et al. (2013). Machine learning approach for automated screening of malaria parasite using light microscopic images. *Micron*, *45*, 97-106.

[85] Assayag, O et al. (2014). Large field, high resolution full-field optical coherence tomography: a pre-clinical study of human breast tissue and cancer assessment. *Technology in cancer research & treatment*, *13*(5), 455-468.

[86] Li, H et al. (2017). Deep learning in breast cancer risk assessment: evaluation of

convolutional neural networks on a clinical dataset of full-field digital mammograms. *Journal of medical imaging*, *4*(4), 041304.

[87] Jo, Y et al. (2017). Holographic deep learning for rapid optical screening of anthrax spores. *Science advances*, *3*(8), e1700606.

[88] Chen, C. L et al. (2016). Deep learning in label-free cell classification. *Scientific reports*, *6*, 21471.

[89] Rao, K. D et al. (2009). Real-time in vivo imaging of adult Zebrafish brain using optical coherence tomography. *Journal of biophotonics*, *2*(5), 288-291.

[90] Esteva, A et al. (2017). Dermatologist-level classification of skin cancer with deep neural networks. *Nature*, *542*(7639), 115.

[91] Shin, H. C et al. (2016). Deep convolutional neural networks for computer-aided detection: CNN architectures, dataset characteristics and transfer learning. *IEEE transactions on medical imaging*, *35*(5), 1285-1298.

[92] Xu, M et al. (2017). A deep convolutional neural network for classification of red blood cells in sickle cell anemia. *PLoS computational biology*, *13*(10), e1005746.

[93] Yi, F., Moon, I., & Javidi, B. (2017). Automated red blood cells extraction from holographic images using fully convolutional neural networks. *Biomedical optics express*, *8*(10), 4466-4479.

[94] Roy, A. G et al. (2017). ReLayNet: retinal layer and fluid segmentation of macular optical coherence tomography using fully convolutional networks. *Biomedical optics express*, *8*(8), 3627-3642.

[95] Samala, R. K et al. (2016). Mass detection in digital breast tomosynthesis: Deep convolutional neural network with transfer learning from mammography. *Medical physics*, *43*(12), 6654-6666.

[96] Mikołajczyk, A., & Grochowski, M. (2018, May). Data augmentation for improving deep learning in image classification problem. In *2018 International Interdisciplinary PhD Workshop (IIPhDW)* (pp. 117-122). IEEE.

[97] Das, A et al. (2018, August). Document Image Classification with Intra-Domain Transfer Learning and Stacked Generalization of Deep Convolutional Neural Networks. In *2018 24th International Conference on Pattern Recognition (ICPR)* (pp. 3180-3185). IEEE.

[98] Samala, R. K et al. (2018, February). Cross-domain and multi-task transfer learning of deep convolutional neural network for breast cancer diagnosis in digital breast tomosynthesis. In *Medical Imaging 2018: Computer-Aided Diagnosis* (Vol. 10575, p. 105750Q). International Society for Optics and Photonics.

[99] Karri, S. P. K., Chakraborty, D., & Chatterjee, J. (2017). Transfer learning based classification of optical coherence tomography images with diabetic macular edema and dry age-related macular degeneration. *Biomedical optics express*, *8*(2), 579-592.

[100] Yap, M. H et al. (2018). Automated breast ultrasound lesions detection using convolutional neural networks. *IEEE journal of biomedical and health informatics*, *22*(4), 1218-1226.

[101] Das, K et al. (2018, April). Multiple instance learning of deep convolutional neural networks for breast histopathology whole slide classification. In *2018 IEEE 15th International Symposium on Biomedical Imaging (ISBI 2018)* (pp. 578-581). IEEE.

[102] Yong, Y. L et al. (2017). Linear-regression convolutional neural network for fully automated coronary lumen segmentation in intravascular optical coherence tomography. *Journal of biomedical optics*, *22*(12), 126005.

[103] Ma, J et al. (2017). Cascade convolutional neural networks for automatic detection of thyroid nodules in ultrasound images. *Medical physics*, *44*(5), 1678-1691.

[104] He, K et al. (2016). Deep residual learning for image recognition. In *Proceedings of the IEEE conference on computer vision and pattern recognition* (pp. 770-778).

[105] Nahid, A. A., & Kong, Y. (2018). Histopathological breast-image classification using local and frequency domains by convolutional neural network. *Information*, *9*(1), 19.

[106] Hussain, Z et al. (2017). Differential data augmentation techniques for medical imaging classification tasks. In *AMIA Annual Symposium Proceedings*(Vol. 2017, p. 979). American Medical Informatics Association.

[107] Lu, G., & Fei, B. (2014). Medical hyperspectral imaging: a review. *Journal of biomedical optics*, *19*(1), 010901.

[108] Kuo, W. C et al. (2008). Assessment of arterial characteristics in human atherosclerosis by extracting optical properties from polarization-sensitive optical coherence tomography. *Optics Express*, *16*(11), 8117-8125.

[109] Kuo, W. C et al. (2017). In vivo images of the epidural space with two-and three-dimensional optical coherence tomography in a porcine model. *PloS one*, *12*(2), e0172149.

[110] Singh, J., Kumar, S., & Arora, A. S. (2018). Thermographic evaluation of mindfulness meditation using dynamic IR imaging. *Infrared Physics & Technology*, *95*, 81-87.

[111] Alonso-Caneiro, D et al. (2016). Tissue thickness calculation in ocular optical coherence tomography. *Biomedical optics express*, *7*(2), 629-645.

[112] Singla, N., Srivastava, V., & Mehta, D. S. (2018). In vivo classification of human skin burns using machine learning and quantitative features captured by optical coherence

tomography. *Laser Physics Letters*, *15*(2), 025601.

[113] Sullivan, A. C., Hunt, J. P., & Oldenburg, A. L. (2011). Fractal analysis for classification of breast carcinoma in optical coherence tomography. *Journal of biomedical optics*, *16*(6), 066010.

[114] Marschall, S et al. (2011). Optical coherence tomography—current technology and applications in clinical and biomedical research. *Analytical and bioanalytical chemistry*, *400*(9), 2699-2720.

[115] Farhat, G et al. (2011, February). Optical coherence tomography speckle decorrelation for detecting cell death. In *Biomedical Applications of Light Scattering V* (Vol. 7907, p. 790710). International Society for Optics and Photonics.

[116] Atif, M et al. (2011). Catheters for optical coherence tomography. *Laser Physics Letters*, *8*(9), 629-646.

[117] Peters, I. T et al. (2016). Noninvasive detection of metastases and follicle density in ovarian tissue using full-field optical coherence tomography. *Clinical Cancer Research*, *22*(22), 5506-5513.

[118] Levine, A., Wang, K., & Markowitz, O. (2016). Optical Coherence Tomography for Skin Cancer Screening. *Gavin J Dermatol Res Ther*, *2016*, 24-25.

[119] He, L et al. (2012). Histology image analysis for carcinoma detection and grading. *Computer methods and programs in biomedicine*, *107*(3), 538-556.

[120] Gurfinkel, R et al. (2010). Histological assessment of tangentially excised burn eschars. *Canadian Journal of Plastic Surgery*, *18*(3), 33-36.

[121] Gurcan, M. N et al. (2009). Histopathological image analysis: A review. *IEEE reviews in biomedical engineering*, *2*, 147.

[122] Yoon, J et al. (2017). Identification of non-activated lymphocytes using three-dimensional refractive index tomography and machine learning. *Scientific reports*, *7*(1), 6654.

[123] Kim, K et al. (2016). Optical diffraction tomography techniques for the study of cell pathophysiology. *Journal of Biomedical Photonics & Engineering*, *2*(2).

[124] Park, J. Y et al. (2016, March). 3D measurements of live cells via digital holographic microscopy and terahertz spectroscopy. In *Quantitative Phase Imaging II*(Vol. 9718, p. 97182D). International Society for Optics and Photonics.

[125] Park, H. S et al. (2016). Automated detection of P. falciparum using machine learning algorithms with quantitative phase images of unstained cells. *PloS one*, *11*(9), e0163045.

[126] Kim, M. K. (2010). Principles and techniques of digital holographic

microscopy. *SPIE reviews*, *1*(1), 018005.

[127] Colomb, T et al. (2006). Numerical parametric lens for shifting, magnification, and complete aberration compensation in digital holographic microscopy. *JOSA A*, *23*(12), 3177-3190.

[128] Girshovitz, P., & Shaked, N. T. (2014). Doubling the field of view in off-axis low-coherence interferometric imaging. *Light: Science & Applications*, *3*(3), e151.

[129] Abdulhalim, I. (2012). Spatial and temporal coherence effects in interference microscopy and full-field optical coherence tomography. *Annalen der Physik*, *524*(12), 787-804.

[130] Patel, N. R et al. (2015, June). Identification of malaria infected red blood samples by digital holographic quantitative phase microscope. In *European Conference on Biomedical Optics* (p. 95360E). Optical Society of America.

[131] Abdulhalim, I. (2006). Competence between spatial and temporal coherence in full field optical coherence tomography and interference microscopy. *Journal of Optics A: Pure and Applied Optics*, *8*(11), 952.

[132] Safrani, A., & Abdulhalim, I. (2011). Spatial coherence effect on layer thickness determination in narrowband full-field optical coherence tomography. *Applied optics*, *50*(18), 3021-3027.

[133] Ahmad, A et al. (2015). Ultra-short longitudinal spatial coherence length of laser light with the combined effect of spatial, angular, and temporal diversity. *Applied Physics Letters*, *106*(9), 093701.

[134] Mehta, D. S et al. (2016, March). Quantitative phase imaging of biological cells and tissues using singleshot white light interference microscopy and phase subtraction method for extended range of measurement. In *Quantitative Phase Imaging II* (Vol. 9718, p. 971828). International Society for Optics and Photonics.

[135] Lee, B. S., & Strand, T. C. (1990). Profilometry with a coherence scanning microscope. *Applied optics*, *29*(26), 3784-3788.

[136] Gao, W. (2015). Effects of temporal and spatial coherence on resolution in full-field optical coherence tomography. *Journal of Modern Optics*, *62*(21), 1764-1774.

[137] Srivastava, V., Nandy, S., & Singh Mehta, D. (2013). High-resolution full-field spatial coherence gated optical tomography using monochromatic light source. *Applied Physics Letters*, *103*(10), 103702.

[138] Dubois, A et al. (2002). High-resolution full-field optical coherence tomography with a Linnik microscope. *Applied optics*, *41*(4), 805-812.

[139] Bhaduri, B et al. (2012). Diffraction phase microscopy with white light. *Optics*

letter, *37*(6), 1094-1096.

[140] Shaked, N. T et al. (2010). Whole-cell-analysis of live cardiomyocytes using wide-field interferometric phase microscopy. *Biomedical optics express*, *1*(2), 706-719.

[141] Debnath, S. K., & Park, Y. (2011). Real-time quantitative phase imaging with a spatial phase-shifting algorithm. *Optics letters*, *36*(23), 4677-4679.

[142] Watanabe, Y., & Sato, M. (2008). Quasi-single shot axial-lateral parallel time domain optical coherence tomography with Hilbert transformation. *Optics express*, *16*(2), 524-534.

[143] "World Malaria Day _ National Health Portal Of India". https://www.nhp.gov.in/World-Malaria-Day_pg (22 May 2017).

[144] Das, D. K., Mukherjee, R., & Chakraborty, C. (2015). Computational microscopic imaging for malaria parasite detection: a systematic review. *Journal of microscopy*, *260*(1), 1-19.

[145] Kapishnikov, S et al. (2017). Biochemistry of malaria parasite infected red blood cells by X-ray microscopy. *Scientific reports*, *7*(1), 802.

[146] Tek, F. B., Dempster, A. G., & Kale, I. (2010). Parasite detection and identification for automated thin blood film malaria diagnosis. *Computer vision and image understanding*, *114*(1), 21-32.

[147] Linder, N et al. (2014). A malaria diagnostic tool based on computer vision screening and visualization of Plasmodium falciparum candidate areas in digitized blood smears. *PLoS One*, *9*(8), e104855.

[148] Bibin, D., Nair, M. S., & Punitha, P. (2017). Malaria parasite detection from peripheral blood smear images using deep belief networks. *IEEE Access*, *5*, 9099-9108.

[149] Liu, R et al. (2011). Recognition and classification of red blood cells using digital holographic microscopy and data clustering with discriminant analysis. *JOSA A*, *28*(6), 1204-1210.

[150] Hejna, M et al. (2017). High accuracy label-free classification of single-cell kinetic states from holographic cytometry of human melanoma cells. *Scientific reports*, *7*(1), 11943.

[151] Rinehart, M., Zhu, Y., & Wax, A. (2012). Quantitative phase spectroscopy. *Biomedical optics express*, *3*(5), 958-965.

[152] Berger, P. D., Gerstenfeld, A., & Zeng, A. Z. (2004). How many suppliers are best? A decision-analysis approach. *Omega*, *32*(1), 9-15.

[153] Buehlmann, P et al., *Package ' mboost .'* 2017.

[154] Liaw, A., & Wiener, M. (2002). Classification and regression by randomForest. *R news*, *2*(3), 18-22.

[155] Keerthi, S. S., & Gilbert, E. G. (2002). Convergence of a generalized SMO algorithm for SVM classifier design. *Machine Learning*, *46*(1-3), 351-360.

[156] Regularized T et al. Package RRF. 2017.

[157] Max , A. et al., Package caret. 2017.

[158] Ripley, B., & Venables, W. (2011). R Package ‘nnet’: Feed-forward neural networks and multinomial log-linear models. *R package version*, *7*(5).

[159] Kim, J. D et al. (2016). Automatic detection of malaria parasite in blood images using two parameters. *Technology and Health Care*, *24*(s1), S33-S39.

[160] Go, T et al. (2018). Machine learning-based in-line holographic sensing of unstained malaria-infected red blood cells. *Journal of biophotonics*, *11*(9), e201800101.

[161] Araújo, T et al. (2017). Classification of breast cancer histology images using convolutional neural networks. *PloS one*, *12*(6), e0177544.

[162] Lee, S et al. (2017). Refractive index tomograms and dynamic membrane fluctuations of red blood cells from patients with diabetes mellitus. *Scientific reports*, *7*(1), 1039.

[163] Grady, L. (2006). Random walks for image segmentation. *IEEE Transactions on Pattern Analysis & Machine Intelligence*, (11), 1768-1783.

[164] Zhang, C., Sun, C., & Pham, T. D. (2013). Segmentation of clustered nuclei based on concave curve expansion. *Journal of microscopy*, *251*(1), 57-67.

[165] Srivastava, N et al. (2014). Dropout: a simple way to prevent neural networks from overfitting. *The Journal of Machine Learning Research*, *15*(1), 1929-1958.

[166] “WHO_Burns” www.who.int/mediacentre/factsheets/fs365/en/ (accessed on 4 Jan 2017).

[167] Kaiser, M et al. (2011). Noninvasive assessment of burn wound severity using optical technology: a review of current and future modalities. *burns*, *37*(3), 377-386.

[168] Monstrey, S et al. (2008). Assessment of burn depth and burn wound healing potential. *burns*, *34*(6), 761-769.

[169] Iftimia, N et al. (2013). Combined reflectance confocal microscopy/optical coherence tomography imaging for skin burn assessment. *Biomedical optics express*, *4*(5), 680-695.

[170] Chua, A. W. C et al. (2016). Skin tissue engineering advances in severe burns: review and therapeutic applications. *Burns & trauma*, *4*(1), 3.

[171] Church, D et al. (2006). Burn wound infections. *Clinical microbiology reviews*, *19*(2), 403-434.

[172] Rosenberg, L et al. (2014). A novel rapid and selective enzymatic debridement agent

for burn wound management: a multi-center RCT. *Burns*, *40*(3), 466-474.

[173] Thatcher, J. E et al. (2016). Imaging techniques for clinical burn assessment with a focus on multispectral imaging. *Advances in wound care*, *5*(8), 360-378.

[174] Sowa, M. G et al. (2001). Near infrared spectroscopic assessment of hemodynamic changes in the early post-burn period. *Burns*, *27*(3), 241-249.

[175] Lotter, O et al. (2015). Utilization of laser Doppler flowmetry and tissue spectrophotometry for burn depth assessment using a miniature swine model. *Wound Repair and Regeneration*, *23*(1), 132-136.

[176] Stewart, C. J et al. (2005). A comparison of two laser-based methods for determination of burn scar perfusion: laser Doppler versus laser speckle imaging. *Burns*, *31*(6), 744-752.

[177] Squiers, J. J et al. (2016, March). Multispectral imaging burn wound tissue classification system: a comparison of test accuracies between several common machine learning algorithms. In *Medical Imaging 2016: Computer-Aided Diagnosis* (Vol. 9785, p. 97853L). International Society for Optics and Photonics.

[178] Jayachandran, M et al. (2016). Critical review of noninvasive optical technologies for wound imaging. *Advances in wound care*, *5*(8), 349-359.

[179] Proskurin, S. G., & Meglinski, I. V. (2007). Optical coherence tomography imaging depth enhancement by superficial skin optical clearing. *Laser Physics Letters*, *4*(11), 824.

[180] Zhao, Y et al. (2015). Evaluation of burn severity in vivo in a mouse model using spectroscopic optical coherence tomography. *Biomedical optics express*, *6*(9), 3339-3345.

[181] Park, B. H et al. (2001). In vivo burn depth determination by high-speed fiber-based polarization sensitive optical coherence tomography. *Journal of biomedical optics*, *6*(4), 474-480.

[182] Gong, P et al. (2016). Optical coherence tomography for longitudinal monitoring of vasculature in scars treated with laser fractionation. *Journal of biophotonics*, *9*(6), 626-636.

[183] Yang, Y et al. (2011). Optical scattering coefficient estimated by optical coherence tomography correlates with collagen content in ovarian tissue. *Journal of biomedical optics*, *16*(9), 090504.

[184] Moiseev, A et al. (2018). Pixel classification method in optical coherence tomography for tumor segmentation and its complementary usage with OCT microangiography. *Journal of biophotonics*, *11*(4), e201700072.

[185] Maher, J. R et al. (2014). In vivo analysis of burns in a mouse model using spectroscopic optical coherence tomography. *Optics letters*, *39*(19), 5594-5597.

[186] Choi, W. J., & Wang, R. K. (2015). Swept-source optical coherence tomography

powered by a 1.3-μm vertical cavity surface emitting laser enables 2.3-mm-deep brain imaging in mice in vivo. *Journal of biomedical optics*, *20*(10), 106004.

[187] Squiers, J. J et al. (2016, March). Multispectral imaging burn wound tissue classification system: a comparison of test accuracies between several common machine learning algorithms. In *Medical Imaging 2016: Computer-Aided Diagnosis* (Vol. 9785, p. 97853L). International Society for Optics and Photonics.

[188] Nandy, S., Sanders, M., & Zhu, Q. (2016). Classification and analysis of human ovarian tissue using full field optical coherence tomography. *Biomedical optics express*, *7*(12), 5182-5187.

[189] Wang, Y et al. (2016). Machine learning based detection of age-related macular degeneration (AMD) and diabetic macular edema (DME) from optical coherence tomography (OCT) images. *Biomedical optics express*, *7*(12), 4928-4940.

[190] Marvdashti, T et al. (2016). Classification of basal cell carcinoma in human skin using machine learning and quantitative features captured by polarization sensitive optical coherence tomography. *Biomedical optics express*, *7*(9), 3721-3735.

[191] Hassan, T et al. (2016). Automated segmentation of subretinal layers for the detection of macular edema. *Applied optics*, *55*(3), 454-461.

[192] Thatcher, J. E et al. (2016). Multispectral and photoplethysmography optical imaging techniques identify important tissue characteristics in an animal model of tangential burn excision. *Journal of Burn Care & Research*, *37*(1), 38-52.

[193] Mandurah, M et al. (2013). Monitoring remineralization of enamel subsurface lesions by optical coherence tomography. *Journal of biomedical optics*, *18*(4), 046006.

[194] Kholodnykh, A. I et al. (2003). Precision of measurement of tissue optical properties with optical coherence tomography. *Applied optics*, *42*(16), 3027-3037.

[195] Haralick, R. M., & Shanmugam, K. (1973). Textural features for image classification. *IEEE Transactions on systems, man, and cybernetics*, (6), 610-621.

[196] Torre, L. and Siegel Rebecca, J. A. (2015). Global Cancer Facts & Figures 3rd Edition. *American Cancer Society*, *800*, 1-64.

[197] Zanjani, F. G., & Zinger, S. (2018, March). Cancer detection in histopathology whole-slide images using conditional random fields on deep embedded spaces. In *Medical Imaging 2018: Digital Pathology* (Vol. 10581, p. 105810I). International Society for Optics and Photonics.

[198] Gál, B et al. (2017). Distinctive behaviour of live biopsy-derived carcinoma cells unveiled using coherence-controlled holographic microscopy. *PloS one*, *12*(8), e0183399.

[199] World Health Organization,2018, http://www.who.int/en/. (Accessed date22 March

2018).

[200] Buist, D. S et al. (2004). Factors contributing to mammography failure in women aged 40–49 years. *Journal of the National Cancer Institute*, *96*(19), 1432-1440.

[201] Taneja, P et al. (2010). Classical and novel prognostic markers for breast cancer and their clinical significance. *Clinical Medicine Insights: Oncology*, *4*, 15-34.

[202] Vakoc, B. J et al. (2012). Cancer imaging by optical coherence tomography: preclinical progress and clinical potential. *Nature Reviews Cancer*, *12*(5), 363-368.

[203] Savastru, D. M et al. (2014). Detection of breast surgical margins with optical coherence tomography imaging: a concept evaluation study. *Journal of Biomedical optics*, *19*(5), 056001.

[204] Zhou, C et al. (2010). Integrated optical coherence tomography and microscopy for ex vivo multiscale evaluation of human breast tissues. *Cancer research*, *70*(24), 10071-10079.

[205] Yao, X et al. (2017). Visualization and tissue classification of human breast cancer images using ultrahigh-resolution OCT. *Lasers in surgery and medicine*, *49*(3), 258-269.

[206] Wan, S et al. (2017). Integrated local binary pattern texture features for classification of breast tissue imaged by optical coherence microscopy. *Medical image analysis*, *38*, 104-116.

[207] Boppart, S. A et al. (2004). Optical coherence tomography: feasibility for basic research and image-guided surgery of breast cancer. *Breast cancer research and treatment*, *84*(2), 85-97.

[208] Ambekar, R et al. (2012). Quantifying collagen structure in breast biopsies using second-harmonic generation imaging. *Biomedical optics express*, *3*(9), 2021-2035.

[209] Srivastava, A et al. (2011). Determination of elastic properties of resected human breast tissue samples using optical coherence tomographic elastography. *Strain*, *47*(1), 75-87.

[210] Abdel-Ilah, L., & Šahinbegović, H. (2017). Using machine learning tool in classification of breast cancer. In *CMBEBIH 2017* (pp. 3-8). Springer, Singapore.

[211] Majeed, H et al. (2018). Label-free quantitative evaluation of breast tissue using Spatial Light Interference Microscopy (SLIM). *Scientific reports*, *8*(1), 6875.

[212] Cvetković, J. (2017). Breast cancer patients' depression prediction by machine learning approach. *Cancer investigation*, *35*(8), 569-572.

[213] Li, H et al. (2018, February). Deep learning in breast cancer risk assessment: evaluation of fine-tuned convolutional neural networks on a clinical dataset of FFDMs. In *Medical Imaging 2018: Computer-Aided Diagnosis* (Vol. 10575, p. 105750S). International Society for Optics and Photonics.

[214] Golatkar, A., Anand, D., & Sethi, A. (2018, June). Classification of Breast Cancer Histology using Deep Learning. In *International Conference Image Analysis and Recognition* (pp. 837-844). Springer, Cham.

[215] Karimian, N et al. (2018, February). Deep learning classifier with optical coherence tomography images for early dental caries detection. In *Lasers in Dentistry XXIV* (Vol. 10473, p. 1047304). International Society for Optics and Photonics.

[216] Albarqouni, S et al. (2016). Aggnet: deep learning from crowds for mitosis detection in breast cancer histology images. *IEEE transactions on medical imaging*, *35*(5), 1313-1321.

[217] Abdolmanafi, A et al. (2017). Deep feature learning for automatic tissue classification of coronary artery using optical coherence tomography. *Biomedical optics express*, *8*(2), 1203-1220.

[218] Tran, P. V. (2016). A fully convolutional neural network for cardiac segmentation in short-axis MRI. *arXiv preprint arXiv:1604.00494*.

[219] Ben-Cohen, A et al. (2017). Retinal layers segmentation using fully convolutional network in OCT images. *RSIP Vision*.

[220] Zheng, Y., Yang, C., & Merkulov, A. (2018, May). Breast cancer screening using convolutional neural network and follow-up digital mammography. In *Computational Imaging III*(Vol. 10669, p. 1066905). International Society for Optics and Photonics.

[221] Duchi, J., Hazan, E., & Singer, Y. (2011). Adaptive subgradient methods for online learning and stochastic optimization. *Journal of Machine Learning Research*, *12*(Jul), 2121-2159.

[222] Stifter, D. (2007). Beyond biomedicine: a review of alternative applications and developments for optical coherence tomography. *Applied Physics B*, *88*(3), 337-357.

[223] Gyger, C et al. (2014). Three-dimensional speckle reduction in optical coherence tomography through structural guided filtering. *Optical Engineering*, *53*(7), 073105.

[224] Kirillin, M. Y et al. (2005). Effect of red blood cell aggregation and sedimentation on optical coherence tomography signals from blood samples. *Journal of Physics D: Applied Physics, 38*(15), 2582.

[225] Heredia-Juesas, J et al. (2016, August). Non-invasive optical imaging techniques for burn-injured tissue detection for debridement surgery. In *2016 38th Annual International Conference of the IEEE Engineering in Medicine and Biology Society (EMBC)* (pp. 2893-2896). IEEE.

[226] Fu, D et al. (2010). Quantitative dispersion microscopy. *Biomedical optics express*, *1*(2), 347-353.

[227] Sarunic, M. V., Weinberg, S., & Izatt, J. A. (2006). Full-field swept-source phase

microscopy. *Optics letters*, *31*(10), 1462-1464.

[228] Swanson, E. A et al. (1993). In vivo retinal imaging by optical coherence tomography. *Optics letters*, *18*(21), 1864-1866.

[229] Safrani, A., & Abdulhalim, I. (2012). Ultrahigh-resolution full-field optical coherence tomography using spatial coherence gating and quasi-monochromatic illumination. *Optics letters*, *37*(4), 458-460.

[230] Tuchin, V. V. (2013). Handbook of coherent-domain optical methods. *Handbook of Coherent-Domain Optical Methods: Biomedical Diagnostics, Environmental Monitoring, and Materials Science, ISBN 978-1-4614-5175-4. Springer Science+ Business Media New York, 2013*.

[231] Vikram, C. S. (2001). Phase error effect on contrast measurement in Schwider-Hariharan phase-shifting algorithm. *Optik*, *112*(3), 140-141.

[232] Shaked, N et al. (2009). Two-step-only phase-shifting interferometry with optimized detector bandwidth for microscopy of live cells. *Optics express*, *17*(18), 15585-15591.

[233] Servin, M., Estrada, J. C., & Quiroga, J. A. (2009). The general theory of phase shifting algorithms. *Optics express*, *17*(24), 21867-21881.

[234] Jackin, B. J., Narayanamurthy, C. S., & Yatagai, T. (2016). Geometric phase shifting digital holography. *Optics letters*, *41*(11), 2648-2651.

[235] Kemao, Q., Fangjun, S., & Xiaoping, W. (2000). Determination of the best phase step of the Carré algorithm in phase shifting interferometry. *Measurement Science and Technology*, *11*(8), 1220.

[236] Hariharan, P., Oreb, B. F., & Eiju, T. (1987). Digital phase-shifting interferometry: a simple error-compensating phase calculation algorithm. *Applied optics*, *26*(13), 2504-2506.

[237] Shaked, N. T., Rinehart, M. T., & Wax, A. (2009). Dual-interference-channel quantitative-phase microscopy of live cell dynamics. *Optics letters*, *34*(6), 767-769.

[238] Majeed, H et al. (2015). Breast cancer diagnosis using spatial light interference microscopy. *Journal of biomedical optics*, *20*(11), 111210.

[239] Lam, V. K et al. (2018). Quantitative assessment of cancer cell morphology and motility using telecentric digital holographic microscopy and machine learning. *Cytometry Part A*, *93*(3), 334-345.

[240] Bhaduri, B et al. (2014). Optical assay of erythrocyte function in banked blood. *Scientific reports*, *4*, 6211.

[241] Park, J. H., Go, T., & Lee, S. J. (2017). Label-Free Sensing and Classification of Old Stored Blood. *Annals of biomedical engineering*, *45*(11), 2563-2573.

LIST OF PUBLICATIONS

In Peer-Reviewed SCI Journals

1. **Neeru Singla**, Vishal Srivastava and Dalip Singh Mehta, "*In vivo* classification of human skin burns using machine learning and quantitative features captured by optical coherence tomography." ***Laser Physics Letter***, vol. 15, no.2, pp.025601, 2018. **Impact Factor - 2.240.**

2. **Neeru Singla**, Vishal Srivastava and Dalip Singh Mehta, "Development of full-field optical spatial coherence tomography system for automated identification of malaria using the multilevel ensemble classifier." ***Journal of Biophotonics,*** vol.11, no. 5, pp. e201700279, 2018. **Impact Factor- 3.768.**

3. **Neeru Singla**, Kavita Dubey and Vishal Srivastava, "Automated assessment of breast cancer margin in optical coherence tomography images via pre-trained convolutional neural network", ***Journal of Biophotonics***, vol.12, no. 3, pp. e201800255, 2018. **Impact Factor- 3.768**

4. **Neeru Singla** and Vishal Srivastava, "Deep learning enabled multi-wavelength spatial coherence microscope for the classification of malaria-infected stages with limited labelled data size", Under Review.

In International Conferences

1. **Neeru Singla**, Kavita Dubey, Vishesh Dubey, Vishal Srivastava, and Dalip Singh Mehta, "Cancerous skin quantitative assessment based on morphological features using PS-FF-OCT system." *International Conference on Advances in Optics and Photonics (ICAOP)*, Nov 2017.

2. **Neeru Singla**, Kavita Dubey, Vishal Srivastava, and Dalip Singh Mehta," Quantitative detection of morphological alterations in red blood cell during storage using PS-FF-OCT system." *In 2017 IEEE Workshop on recent advances on Photonics (WRAP)*, Dec 2017.

3. **Neeru Singla**, Kavita Dubey, Vishal Srivastava, Azeem Ahmad and D. S. Mehta,

"Automated high resolution full-field spatial coherence tomography for quantitative phase imaging of human red blood cells", Proc. SPIE 10503, Quantitative Phase Imaging IV, 105032I (23 February 2018), doi: 10.1117/12.2286612.